GROWTH OF SILICA-BASED NANOPARTICLES: CONTROLLING STRUCTURE AND FUNCTION

A Dissertation

Presented to the Faculty of the Graduate School

of Cornell University

In Partial Fulfillment of the Requirements for the Degree of

Doctor of Philosophy

by

Teresa Yi Kao

December 2017

GROWTH OF SILICA-BASED NANOPARTICLES CONTROLLING STRUCTURE AND FUNCTION

Teresa Yi Kao, Ph. D.

Cornell University 2017

Silica chemistry provides a uniquely tunable platform for nanoparticle synthesis, where particle size, nanoscale morphology, and surface properties can be precisely controlled. Recent advances demonstrate that conveniently accessible parameters, including silica precursor chemistry, solvent, and reaction pH, can be used to tune particle size down to below 10 nm. By cooperative assembly of inorganic silica species and organic molecular structure directing agents, a diverse range of mesoporous silica nanoparticles with hexagonal, cubic, and multicompartment structures can be produced. This versatile chemistry provides pathways for answering fundamental questions about structure formation and developing novel functional nanomaterials for applications including separation, catalysis, and drug delivery. In this dissertation, two examples of such silica nanoparticle systems are discussed.

As a first example, the development of an intensity-based fluorescent silica nanoparticle barcode is discussed. This work is motivated by a need for fluorescent tags that increase the number of molecular species that can be simultaneously labeled and reliably distinguished using commercially available fluorescence microscopes. In this study, the synthetic parameters that govern the incorporation of precisely controlled numbers of fluorescent dyes into silica nanoparticles in batch reactions are identified. Heterogeneities within particle batches are mapped using single particle fluorescence microscopy. Proof-of-concept experiments demonstrate that fluorescent

silica nanoparticles with well-separated high and low fluorescence intensity distribution levels can be synthesized in batch reactions and used as an intensity barcode in fluorescence microscopy.

In the second example, a mesoporous silica nanoparticle system, structure directed by surfactant-micelle self-assembly, is investigated. As a function of an added pore expander molecule or reaction stirring rate, a series of four distinct mesoporous silica nanoparticle structures is observed: hexagonal, cubic/hexagonal multicompartment, cubic, and dodecagonal quasicrystalline. The mechanism driving the structural transition between cubic crystalline and dodecagonal quasicrystalline mesoporous silica nanoparticles is investigated. Control of nanoparticle size down to a single tiling unit (< 30 nm), allows direct comparison between experimental results and a simple theoretical growth model, providing insights into the early growth trajectories of quasicrystalline mesoporous silica. This work identifies simple synthetic control parameters for quasicrystal growth that may be translated to other self-assembled systems.

BIOGRAPHICAL SKETCH

Teresa Yi Kao was born in Stony Brook, New York on February 11, 1990. She attended Columbia University for her undergraduate studies in Applied Physics. From 2009 to 2011, she participated in the Research Experience for Undergraduates (REU) summer program at Harvard University. In 2009, she worked in the laboratory of Professor David Weitz, studying cell migration behavior on stiffness patterned substrates using fluorescence microscopy. From 2010 to 2011, she worked in the laboratory of Professor Wesley Wong, where she implemented a gravity-based technique for characterization of force dependent binding kinetics between biomolecules. In 2012, she moved to Ithaca, New York to pursue a doctorate in Materials Science and Engineering at Cornell University. She worked in the laboratory of Professor Ulrich Wiesner, studying the growth of silica-based nanomaterials. She will move to Hillsboro, Oregon upon completing her degree to work as a Process Engineer in the Portland Technology Development (PTD) group at Intel.

To My Family

ACKNOWLEDGMENTS

This work would not have been possible without the support of a great number of people. First, I would like to thank my advisor Professor Ulrich Wiesner, whose support and guidance helped me grow immensely as a scientist and as an individual. I would also like to thank my committee members Professor Veit Elser and Professor Lara Estroff for all their support.

Thank you to all the members of the Wiesner group. You have all taught me so much and your insightful feedback has been much appreciated. A special thank you to Dr. Kai Ma for all your help throughout the years. I would also like to thank Dolores Dewbury for all her help navigating the administrative side of graduate school. Thank you to my friends (Angela, Abby, Jennie, Mun and Qi) for thoughtfully listening to my research problems and providing innovative solutions. Thank you to all my collaborators, especially Professor Veit Elser, whose guidance on quasicrystals has been invaluable to my work. I would like to thank the wonderful staff at the CCMR, NBTC, and BRC (John Grazul, Don Werder, Penny Burke, Teresa Porri, Brian Bowman) for all of their help solving my research problems.

Thank you to my family and David for your unwavering support. I could not have done any of it without you.

TABLE OF CONTENTS

Biographical Sketch……...……...……. v

Dedication……...……..…… vi

Acknowledgements……...……... vii

Table of Contents……..…….……. viii

List of Figures……... x

List of Tables……..…….. xiii

Chapter 1- Introduction……... 1

References……...……. 6

Chapter 2- Introduction……...……. 10

Experimental Methods……...…… 14

Results and Discussion……. 16

Conclusion……...…… 24

References……...……. 26

Chapter 3- Introduction……...……. 29

Experimental Methods…… 31

Characterization……...…… 34

Results and Discussion…… 37

Conclusion……...…… 51

References……...……. 54

Chapter 4- Introduction……...……. 60

Experimental Methods…..……... 63

Characterization……...…… 64

Results and Discussion……. 79

Conclusion……...…… 51

References……..……. 83

Chapter 5- Introduction……...……. 89

Experimental Methods…..…… 92

Characterization……...…… 64

Results and Discussion……... 100

Conclusion……...…….. 110

References……...……... 112

Chapter 6- Conclusion…..……...……... 113

References……...……... 115

Appendix A……...……. 128

References……...……... 133

Appendix B……...……. 134

Appendix C……...……. 137

References……...……... 154

Appendix D……...……. 155

LIST OF FIGURES

Figure 2.1 Schematic illustration of a bath dye approach for synthesizing fluorescent polymer beads ……..…… 12

Figure 2.2 Schematic representations of the preparation of fluorescent SNPs and substrates for TIRF microscopy.……..…… 15

Figure 2.3 Characterization of fluorescent SNPs synthesized by homogenous and seeded growth……..... 17

Figure 2.4 Comparison of fluorescence intensity levels for low and high dye-loaded SNPs as revealed by single particle imaging using TIRF microscopy …… 20

Figure 3.1 Fluorescent SNPs prepared by homogenous growth ……. 38

Figure 3.2 Characterization of APTES-induced size dispersity……. 40

Figure 3.3 Comparison of high and low dye-loaded SNPs …….. 43

Figure 3.4 Optimization of seeded growth conditions……..……...…… 46

Figure 3.5 Seeded growth of SNPs using different organosilane linkers …….. 51

Figure 4.1 Four mesoporous silica nanoparticle structures observed in two silane systems as a function of mesitylene concentration ……. 67

Figure 4.2 Quasicrystallinity of tetramethyl orthosilicate/(3-aminopropyl) tri-methoxysilane derived mesoporous silica nanoparticles.....… 71

Figure 4.3 Cryo-transmission electron microscopy of native micelle solutions prepared using varying mesitylene concentrations and stirring rates …… 73

Figure 4.4 Analysis of tetramethyl orthosilicate/(3-aminopropyl)trimethoxysilane derived mesoporous silica nanoparticles and simulated structures …… 76

Figure 4.5 Analysis of simulated single particle growth trajectories …… 79

Figure 4.6 Comparison of simulated growth trajectories with tetramethyl orthosilicate /(3-aminopropyl)trimethoxysilane derived mesoporous silica nanoparticles ……..… 80

Figure 5.1 Micelle size distributions from cryo-TEM images …… 95

Figure 5.2 Schematic illustration of the proposed assembly model ……... 97

Figure 5.3 Plots of $R_g^{\perp}$ against $R_g^{\parallel}$ calculated for tilings …….……... 103

Figure 5.4 Plots of $R_g^{\perp}$ against $R_g^{\parallel}$ calculated for tilings produced using S = 0.1 … 105

Figure 5.5 Representative particle growth trajectories from simulations ……. 107

Figure 5.6 Representative tiling with S = 2.3 and radius = 25*d* ……..…….. 110

Figure A.1 Characterization of SNPs synthesized by homogenous growth.…...….. 125

Figure A.2 Spot detection and intensity analysis……...… 126

Figure A.3 Substrate background and intensity threshold .……...… 127

Figure A.4 Characterization of nanoparticle intermediates during seeded growth, using 24.0 μM Cy3/AEAPTMS.……...…...… 128

Figure A.5 Intensity distributions for SNPs synthesized using seeded growth.....… 129

Figure B.1 Optimization of laser power in TIRF microscopy.…...……... 130

Figure B.2 Comparison of homogenous and seeded growth conditions in TIRF microscopy……..... 135

Figure B.3 Characterization of size dispersity in SNPs prepared using different dye conjugates…….…...……... 136

Figure C.1 Fast Fourier transform analysis of a tetraethyl orthosilicate/N-(2-aminoethyl)-3-aminopropyltrimethoxysilane derived multicompartment particle.... 146

Figure C.2 Structure evolution of tetraethyl orthosilicate/N-(2-aminoethyl)-3-aminopropyltrimethoxysilane derived mesoporous silica nanoparticles as a function of mesitylene concentration as revealed by small angle x-ray scattering and nitrogen sorption.…...……... 147

Figure C.3 Single-tilt transmission electron microscopy study of a tetraethyl orthosilicate/N-(2-aminoethyl)-3-aminopropyltrimethoxysilane derived mesoporous silica nanoparticle with dodecagonal tiling.……... 148

Figure C.4 Synthesis maps of mesoporous silica nanoparticles synthesized using two different silane systems……..…..... 149

Figure C.5 Pore size analysis of tetraethyl orthosilicate/N-(2-aminoethyl)-3-aminopropyltrimethoxysilane derived mesoporous silica nanoparticles synthesized under varying conditions.…….…….…..... 150

Figure C.6 Structure evolution of tetraethyl orthosilicate/N-(2-aminoethyl)-3-aminopropyltrimethoxysilane derived mesoporous silica nanoparticles as a function of stirring rate..…….…….…..... 151

Figure C.7 Tiling analysis for mesoporous silica nanoparticles synthesized using the tetraethyl orthosilicate/N-(2-aminoethyl)-3-aminopropyltrimethoxysilane silane system at 116mM mesitylene...…….…….……..…….…..... 152

Figure D.1 Tilings from simulations performed using a modified version of Tiling Rule 3 that allows replacement site selection only……..…….…..... 155

Figure D.2 Representative tilings using S = 0.1, 0.01 and radius = 25 *d*. 156

LIST OF TABLES

Table C.1 Pore size analysis derived from nitrogen sorption measurements on mesoporous silica nanoparticles synthesized using tetraethyl orthosilicate and N-(2-aminoethyl)-3-aminopropyltrimethoxysilane....……..……..…….. 153

CHAPTER 1

INTRODUCTION

Abstract

The focus of the work described in this thesis is the synthesis and characterization of silica-based nanoparticles. Silica chemistry is employed as a synthesis platform for the investigation of structure formation mechanisms in mesoporous silica and for the development of functional silica nanoparticles. This chapter introduces fundamental concepts in the preparation of silica nanoparticles. Each of the following chapters contains a brief introduction that provides a summary of the relevant literature and background.

Synthesis of Silica Nanoparticles

A widely used method[1] for preparing silica spheres, in which tetraethyl orthosilicate (TEOS) is hydrolyzed in a basic mixture of water and alcohol, was introduced by Stöber and co-workers in 1968. Monodisperse particles obtained using this approach range from less than 0.05 μm to 0.7 μm in diameter[1]. Size control is achieved by varying solvent ratio and reaction pH[2]. Variations of the Stöber synthesis[2] using silica precursors with larger alkoxy groups (i.e. tetrapentyl orthosilicate) have been introduced to extend particle sizes to ~2 μm. In general, smaller particle sizes are accessed by using smaller alcohols as solvents[2]. Particle sizes can also be tuned by incremental growth of silica shells[3].

Recent advances demonstrate that in water, sub-10 nm particle sizes can be achieved by reacting tetramethyl orthosilicate under basic conditions[4]. Controlled particle growth from ~ 4 to 10 nm can be achieved by using increasing reaction temperatures or by shell addition[4]. In Chapters 2 and 3 of this dissertation, an amino acid catalyzed reaction of TEOS in aqueous media at 60°C is used, because it facilitates particle size control between 12 and 200 nm[5, 6]. The formation of silica particles in aqueous media at elevated temperatures proceeds by rapid aggregation of small (< 2 nm) silica clusters[4, 7]. Since the reaction is conducted at high pH, the colloidal suspension is stabilized by electrostatic repulsion between the negatively-charged particles[3]. Continued growth of silica particles under these conditions proceeds by silica cluster addition[7].

Uniformly sized silica nanoparticles (SNPs) have attracted widespread interest for applications in bioimaging, because silica is optically transparent and biocompatible[8]. A variety of functionalities can also be introduced to SNPs by using organosilane linkers[9, 10]. For example, covalent encapsulation of fluorescent dyes with activated ester groups can be achieved by conjugation with an aminosilane (e.g.

aminopropyl triethoxysilane) [8, 9]. Additionally, encapsulation inside the rigid silica matrix improves the photophysical properties of the dyes (i.e. brightness and photostability)[11]. Facile surface modification protocols provide routes to stable, multi-functional particles[12]. In this work, the development of a fluorescence intensity-based silica nanoparticle barcode is described.

Synthesis of Mesoporous Silica Materials

Mesoporous silica materials have large specific surface areas and pore sizes between 2 and 50 nm[14]. Mesoporous silica materials are prepared by self-assembly of silica precursors (e.g. TEOS) and surfactant or polymer micelle templates. The organic template can be removed by calcination of the resulting material at high temperatures[14]. Early examples of mesoporous silica materials used quaternary ammonium surfactants (e.g. CTAB) as structure-directing agents (SDA) under basic synthesis conditions[15, 16]. Surfactants with varying alkyl chain lengths could be used to tune pore diameters from 2 to 5 nm[16]. Mesoporous silica materials with increased pore sizes (~30 nm) were generated by using block copolymer templates (e.g. SBA-15) under acidic conditions[17].

Two general pathways for structure formation in mesoporous silica materials have been identified[14]. In the first case, use of high surfactant concentrations enables the formation of an organic, liquid crystalline template[16]. Mesoporous silica is formed by infiltration of silica precursors into the template. In the second model, mesostructured silica is formed by cooperative assembly at relatively low surfactant concentrations, driven by electrostatic interactions between surfactants (e.g. positively charged CTAB surfactant head groups) and negatively-charged silica precursors[18]. Variations of the synthesis using anionic surfactants typically use a positively charged co-structure directing agent (CDSA)[19, 20].

Mesopore structure depends critically on the micelle template. The size and shape of a surfactant micelle can be described by a surfactant packing parameter, which accounts for the head-group area, tail length, and tail volume of the surfactant molecule[21]. In surfactant-silicate systems, the effective head-group area of the surfactant is strongly affected by electrostatic and steric interactions with negatively charged silica species[18]. Additives, such as micelle expanders, can also be added to the surfactant-silicate system to tune the micelle size and shape[18]. Synthetic control of micelle templates in surfactant-silicate systems has produced a variety of mesoporous silica structures, including hexagonal, cage-like cubic, cubic continuous, and dodecagonal quasicrystal structures[14, 22].

Due to their high surface areas and large pore volumes, mesoporous silica materials have attracted widespread interest for applications including catalysis, separation, and nanomedicine[14]. The versatile silica chemistry provides tremendous opportunity for the design of functional materials. As an example, single-pore mesoporous silica nanoparticles with sizes below 10 nm have been developed as therapeutic nanocarriers[23]. Additionally, readily accessible control parameters (e.g. micelle expanders and co-structure directing agents) provide pathways for fundamental investigations of structure formation mechanisms[14]. In this work, the surfactant-directed assembly of mesoporous silica nanoparticles is used as a platform for investigating the early growth mechanisms of quasicrystalline mesoporous silica.

Thesis Outline

The development of nano-sized fluorescence barcodes can greatly increase the number of molecular species that can be tagged and simultaneously observed using commercially available fluorescence microscopes. Silica chemistry provides a promising pathway for barcode design. In Chapter 2, the synthesis of a series of highly

fluorescent silica nanoparticle probes with sizes < 40 nm and controlled fluorescence intensity levels is described. A previously reported method for amino acid catalyzed growth of silica nanoparticles in aqueous media is used as a synthesis platform[5, 6].

Heterogeneities within batches of particles are investigated using single particle fluorescence microscopy. Proof-of concept experiments demonstrate that silica nanoparticles synthesized with high and low intensity levels can be used as an intensity barcode in single-particle fluorescence images. A key parameter in the optimized protocol is the use of a seeded growth approach to minimize formation of low dye-loaded secondary particles. Additional variations of the synthesis are described in Chapter 3, including the use of different organosilane linkers for covalent encapsulation of dyes inside the silica matrix.

A second nanoparticle system is described in Chapters 4 and 5. The surfactant-directed assembly of mesoporous silica nanoparticles is used to investigate the early growth pathways of quasicrystalline mesoporous silica. In Chapter 4, increasing concentrations of a micelle expander or equivalently, increasing reaction stirring rate, induces structural transitions from hexagonal, to hexagonal/cubic multicompartment[24], to cubic, and to dodecagonal quasicrystalline MSNs. The transition between cubic crystalline and dodecagonal quasicrystalline structure is investigated in detail.

In this system, control of MSN size down to a single tiling unit (< 30 nm) facilitates direct comparison between experimental results and a simple theoretical growth model. A full account of the growth model used in this study is provided in Chapter 5. In this work, simulations are finally employed to extended the growth of MSNs beyond particle sizes observed in experiment.

This thesis concludes with a discussion of future directions for research on controlling the structure and function of silica nanoparticles.

REFERENCES

1. Stöber, W.; Fink, A.; Bohn, E. Controlled Growth of Monodisperse Silica Spheres in the Micron Size Range. *J. Coll. Int. Sci.* **1968**, *26*, 62-69.

2. Brinker, C. J.; Scherer, G. W. *Sol-Gel Science;* Academic Press: New York, **1990**.

3. Nyffenegger, R.; Quellet, C.; Ricka, J. Synthesis of Fluorescent, Monodisperse, Colloidal Silica Particles. *J. Coll. Int. Sci.* **1993**, *159*, 150-157.

4. Ma, K.; Mendoza, C.; Werner-Zwanziger, U.; Zwanziger, J.; Wiesner, U. Control of Ultrasmall Sub-10 nm Ligand-Functionalized Fluorescent Core−Shell Silica Nanoparticle Growth in Water. *Chem. Mater.* **2015**, *27*, 4119 – 4133.

5. Yokoi, T.; Sakamoto, Y.; Terasaki, O.; Kubota, Y.; Okubo, T.; Tatsumi, T. Periodic Arrangement of Silica Nanospheres Assisted by Amino Acids. *J. Am. Chem. Soc.* **2006**, *128*, 13664 – 13665.

6. Hartlen, K. D.; Athanasopoulos, A. P. T.; Kitaev, V. Facile Preparation of Highly Monodisperse Small Silica Spheres (15 to >200 nm) Suitable for Colloidal Templating and Formation of Ordered Arrays. *Langmuir*. **2008**, *24*, 1714-1720.

7. Carcouët, C. C. M. C.; van de Put, M. W. P.; Mezari, B.; Magusin, P. C. M. M.; Laven, J.; Bomans, P. H. H.; Friedrich, H.; Catarina, A.; Esteves, C.; Sommerdijk, N. A. J. M.; van Benthem, R. A. T. M.; de With, G. Nucleation and Growth of Monodisperse Silica Nanoparticles. *Nano Lett.* **2014**, *14*, 1433 – 1438.

8. Burns, A.; Ow, H.; Wiesner, U. Fluorescent core-shell silica nanoparticles: towards “Lab on a particle” architectures for nanobiotechnology. *Chem. Soc. Rev.* **2006**, *35*, 1028 – 1042

9. van Blaaderen, A.; Vrij, A. Synthesis and Characterization of Colloidal Dispersions of Fluorescent, Monodisperse Silica Spheres. *Langmuir*. **1992**, *8*, 2921-2931.

10. Ow, H.; Larson, D.; Srivastava, M.; Baird, B., Webb, W.; Wiesner U. Bright and Stable Core−Shell Fluorescent Silica Nanoparticles. *Nano Lett.* **2005**, *5*, 113 - 117.

11. Larson, D. R.; Ow, H.; Vishwasrao, H. D.; Heikal, A. A.; Wiesner, U.; Webb, W. W. Silica Nanoparticle Architecture Determines Radiative Properties of Encapsulated Fluorophores. *Chem. Mater.* **2008**, *20*, 2677 – 2684.

12. Ma, K.; Zhang, D.; Cong, Y.; Wiesner, U. Elucidating the Mechanism of Silica Nanoparticle PEGylation Processes Using Fluorescence Correlation Spectroscopies. *Chem. Mater.* **2016**, *28*, 1537 – 1545.

13. Ma, K.; Wiesner, U. Modular and Orthogonal Post-PEGylation Surface Modifications by Insertion Enabling Penta-Functional Ultrasmall Organic-Silica Hybrid Nanoparticles. *Chem. Mater.* **2017**, *29*, 6840 – 6855.

14. Hoffman, F.; Cornelius, M.; Morell, J.; Fröba, M. Silica-Based Mesoporous Organic–Inorganic Hybrid Materials. *Angew. Chem. Int. Ed.* **2006**, *45*, 3216–3251.

15. Yanagisawa, T.; Shimizu, T.; Kuroda, K.; Kato, C. The Preparation of Alkyltrimethylammonium-Kanemite Complexes and Their Conversion to Microporous Materials. *Bull. Chem. Soc. Jpn.* **1990**, *63*, 988 – 922.

16. Kresge, C. T.; Leonowicz, M. E.; Roth, W. J.; Vartuli, J. C.; Beck, J. S. Ordered mesoporous molecular sieves synthesized by a liquid-crystal template mechanism. *Nature* **1992**, *359*, 710 – 712.

17. Zhao, D.; Feng, J.; Huo, Q.; Melosh, N.; Fredrickson, G. H.; Chmelka, B. F.; Stucky, G. D. Triblock Copolymer Syntheses of Mesoporous Silica with Periodic 50 to 300 Angstrom Pores. *Science* **1998**, *279*, 548 – 552.

18. Monnier, A.; Schuth, F.; Huo, Q.; Kumar, D.; Margolese, D.; Maxwell, R. S.; Stucky, G. D.; Krishnamurty, M.; Petroff, P.; Firouzi, A.; Janicke, M.; Chmelka, B. F. Cooperative Formation of Inorganic-Organic Interfaces in the Synthesis of Silicate Mesostructures. *Science* **1993**, *261*, 1299 – 1303.

19. Che, S.; Garcia-Bennett, A. F.; Yokoi, T.; Sakamoto, K.; Kunieda, H.; Terasaki, O.; Tatsumi, T. A novel anionic surfactant templating route for synthesizing mesoporous silica with unique structure. *Nat. Mater.* **2003**, *2*, 801 – 805.

20. Gao, C.; Sakamoto, Y.; Terasaki, O.; Che, S. Formation of Diverse Mesophases Templated by a Diprotic Anionic Surfactant. *Chem. Eur. J.* **2008**, *14*, 11423 – 11428.

21. Israelachvilli, J. *Intermolecular and Surface Forces;* Academic Press: New York, **1991**.

22. Xiao, C.; Fujita, N.; Miyasaka, K.; Sakamoto, Y.; Terasaki, O. Dodecagonal tiling in mesoporous silica. *Nature* **2012,** *487*, 349-353.

23. Ma, K.; Sai, H.; Wiesner, U. Ultrasmall Sub-10 nm Near-Infrared Fluorescent Mesoporous Silica Nanoparticles. *J. Am. Chem. Soc.* **2012**, *134*, 13180 – 13183.

24. Suteewong, T.; Sai, H.; Hovden, R.; Muller, D.; Bradbury, M. S.; Gruner, S. M.; Wiesner, U. Multicompartment Mesoporous Silica Nanoparticles with Branched Shapes: An Epitaxial Growth Mechanism. *Science* **2013**, *340*, 337 – 341.

CHAPTER 2

FLUORESCENT SILICA NANOPARTICLES WITH WELL SEPARATED INTENSITY DISTRIBUTIONS FROM BATCH REACTIONS[*]

Abstract

Silica chemistry provides pathways to uniquely tunable nanoparticle platforms for biological imaging. It has been a long-standing problem to synthesize fluorescent silica nanoparticles (SNPs) in batch reactions with high and low fluorescence intensity levels for reliable use as an intensity barcode, which would greatly increase the number of molecular species that could be tagged intracellularly and simultaneously observed in conventional fluorescence microscopy. Here, employing an amino-acid catalyzed growth, highly fluorescent SNP probes were synthesized with sizes < 40 nm and well separated intensity distributions, as mapped by single-particle imaging techniques. A seeded growth approach was used to minimize the rate of secondary particle formation. Organic fluorescent dye affinity for the SNP during shell growth was tuned using specifics of the organosilane linker chemistry. This work highlights design considerations in the development of fluorescent probes with well separated intensity distributions synthesized in batch reactions for single-particle imaging and sensing applications, where heterogeneities across the nanoparticle ensemble are critical factors in probe performance.

---

[*] Prepared for Submission as: Teresa Kao, Ferdinand Kohle, Kai Ma, Tangi Aubert Alexander Andrievsky, Ulrich Wiesner. *Fluorescent Silica Nanoparticles with Well Separated Intensity Distribution from Batch Reactions.*

Introduction

Fluorescence microscopy has emerged as a powerful technique for non-invasive biological imaging[1]. Target molecules are typically visualized using fluorescent tags, such as fluorescent proteins[2, 3], organic dyes, or nanoparticles[4, 5]. Using spectrally distinct fluorescent tags, multiple molecular species can be labeled and simultaneously detected, facilitating studies of complex biological systems[6]. However, spectral multiplexing remains limited in many systems by the number of fluorescent tags that can be reliably distinguished using commercially available microscopes. This problem motivates a need for novel fluorescent tags that increase the number of molecular species that can be imaged in parallel, while maintaining the small sizes and target labeling capabilities of traditional fluorophores[7].

Optical barcodes for highly multiplexed imaging have been realized in micron-sized beads exhibiting multiple spectral colors at distinguishable intensity levels[8-10]. These bead-based technologies typically rely on "bath dye" approaches for controlling fluorescence intensity, where solvent-swollen polymer particles are incubated in a solution of organic dye molecules, allowing dyes to absorb into the particles. Subsequent solvent removal traps dyes inside the particles[9, 10]. Using micron-sized particles, intensity barcodes with up to ten distinguishable intensity levels can be generated simply by changing the concentration of dyes in the bath[8-10]. Despite wide success in micron-sized particles, the development of nano-sized intensity barcodes remains a challenge[7]. Highly-loaded microbeads may contain thousands of dyes per particle, allowing use of widely separated adjacent intensity levels[8]. For example, a factor of two difference in dye concentration may be used to generate microbeads that differ in dye-loading by an average of one thousand dyes. However, similar strategies cannot be applied in nano-sized systems, where small particle volumes necessitate use of substantially lower numbers of dyes per particle to

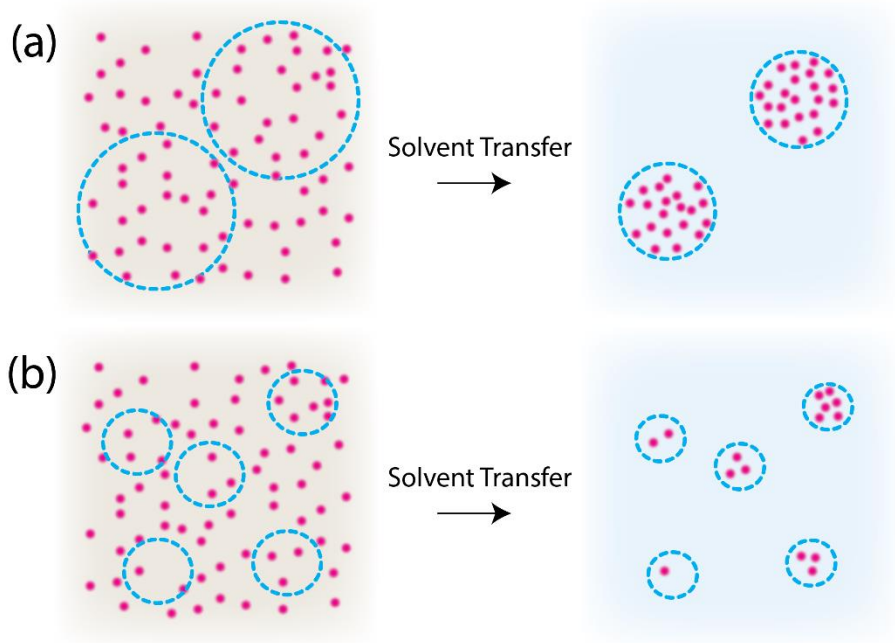

Figure 2.1. Schematic illustration of a bath dye approach for synthesizing fluorescent polymer beads. (a, b) Solvent-swollen polymer particles (blue circles) are incubated in a solution of organic dye molecules, allowing dyes to absorb into particles. Solvent transfer traps dyes inside the particles. Comparison of large (a) and small (b) particles shows that decreasing the average number of encapsulated dyes in small particles magnifies the effects of local concentration fluctuations on the number of dyes per particle leading to large heterogeneities.

prevent fluorescence quenching[11]. Under this constraint, a factor of two difference in dye concentration results in average differences of only a few dyes per particle and as illustrated in Figure 2.1, local fluctuations in dye concentration alone may cause overlap between intensity distributions[10].

While previous reports have shown that this problem can be solved using programmable materials, including DNA and RNA[7, 12], only limited success in nanoparticle-based systems has been achieved[13, 14]. Distinguishable intensity levels are difficult to achieve in nanoparticles using infiltration-based batch synthesis approaches even at increasing dye concentrations, due to low encapsulation efficiency[15]. Previous reports have shown that highly dye-doped nanoparticles with minimal fluorescence quenching may be synthesized by controlled covalent attachment of dyes during particle growth[16]. However, using these methods, the batch synthesis of nanoparticles with non-overlapping intensity distributions is complicated by heterogeneities across the ensemble, often exacerbated by secondary particle formation during growth[17]. Here, we have addressed these problems using a highly tunable synthesis method for covalently encapsulating organic fluorescent dyes inside silica nanoparticles (SNPs), by controlling secondary particle formation and varying the organosilane linker chemistry to the dye, demonstrating that high and low dye-loaded SNP intensity distributions are well separated as mapped by single particle fluorescence imaging.

Silica chemistry provides a uniquely tunable platform for nanoparticle synthesis, where particle size[18-20], nanoscale morphology[21], and surface properties[22, 23] can be precisely controlled. Recent advances in fabrication have extended the range of accessible particle sizes to below 10 nm, using water as a solvent[18], and established efficient methods for surface functionalization with a variety of targeting moieties[22, 23], making such materials ideal candidates as probes for biological imaging. We use a previously reported method for amino acid catalyzed growth of SNPs in aqueous

media[19, 20] to investigate the synthetic parameters that govern single-particle intensity distributions in fluorescent dye-loaded SNPs. Using this basic framework, we demonstrate two different approaches for synthesizing bright SNPs with tunable average fluorescence intensity levels and sizes below 40 nm. Controlled distributions of dyes within individual SNPs are achieved by incremental shell growth, allowing dyes to remain unquenched even at high loadings. The resulting SNPs are up to 100 times brighter than the constituent dyes. Optimized intensity distributions, as mapped by single-particle imaging techniques, are achieved by using a seeded growth approach to minimize the rate of secondary particle formation and by tuning the affinity of the organosilane linker for the SNP during shell growth to improve the incorporation efficiency of the often-expensive fluorescent dye molecules, by means of functional groups able to hydrogen bond to silica surface silanol groups.

Experimental

Cy3-labeled SNPs were prepared either by homogenous or seeded growth in the presence of a Cy3-silane conjugate (Figure 2.1a) (see Supporting Information for detailed methods). We utilized l-arginine as a base catalyst for SNP formation in aqueous media at elevated temperatures[19, 20, 24] of 60 °C. As previously studied in detail[18, 25], under such conditions (i.e. aqueous medium at elevated temperatures) silica nanoparticle formation proceeds via the rapid formation of small (< 2 nm) silica clusters which subsequently aggregate into larger particles. In this system, however, a thin layer of tetraethoxysilane (TEOS) added to the top surface of the aqueous reaction volume serves as the silica source, with the interfacial area determining the rate of hydrolyzed TEOS diffusing into the water phase. For SNPs synthesized using what we call in the following the "homogenous" growth approach (Figures 2.2a and c), Cy3 dye was covalently coupled to an aminopropyltriethoxysilane (APTES) and added to

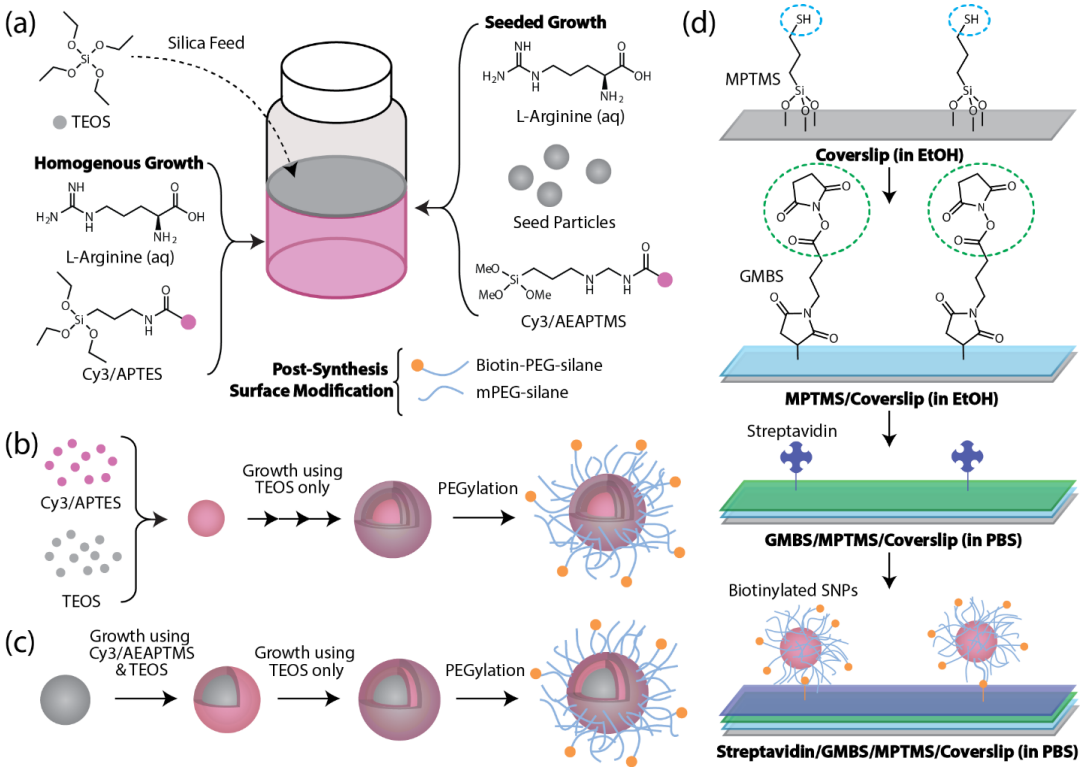

Figure 2.2 Schematic representations of the preparation of fluorescent SNPs and substrates for TIRF microscopy. (a) Experimental setup and chemicals used during synthesis. (b, c) Growth pathways of fluorescent SNPs synthesized using (b) homogenous and (c) seeded growth. (d) For single particle imaging, a thiol-coated substrate (blue) was prepared by incubating a glass slide (gray) in a solution of MPTMS in ethanol (EtOH). Heterobifunctional GMBS was attached to the thiol-coated substrate using its reactive maleimide group and the NHS ester group (green) at the opposite end was coupled to a primary amine on the streptavidin molecule (purple). Substrates were rinsed thoroughly after each step to remove unreacted chemicals. Biotinylated SNPs were attached to streptavidin-coated substrates just before imaging.

the water phase before TEOS was layered on top. APTES was chosen for its relatively slow hydrolysis kinetics, as compared to aminopropyltrimethoxysilane (APTMS)[26], to minimize self-aggregation and quenching of Cy3 dyes during particle nucleation. Due to the slow reaction rate of the sterically hindered Cy3/APTES conjugate, it is not fully consumed during the core synthesis. Three subsequent TEOS additions in 8 hr increments were therefore used to allow for continued attachment of unreacted Cy3/APTES to SNPs, resulting in highly dye-doped particles. After growth was completed, SNPs were stabilized by covalent attachment of polyethylene glycol (PEG) chains[22]. SNPs were subsequently purified using gel permeation chromatography (GPC) to remove any unreacted chemicals[18, 23] (Figures A1c and d).

Results and Discussion

As a result of covalent dye encapsulation in the rigid silica matrix[4, 27, 28], normalized absorption and emission spectra (Figures 2.3a) show that per dye brightness levels increase ~7 to 8 times over free dye in solution. Only slightly decreased per dye fluorescence enhancements are observed as the concentration of Cy3-silane is increased, suggesting that even at high loadings, dyes remain essentially unquenched. Cy3-labeled SNPs were further characterized using fluorescence correlation spectroscopy (FCS)[27], where fluctuations in fluorescence intensity generated by particle diffusion into and out of a detection volume of a confocal setup are autocorrelated and fit using a model describing single-component diffusion[4, 29, 30]. Importantly, a single FCS measurement provides information over hydrodynamic particle size, particle concentration, as well as particle brightness[27], making it a powerful tool in fluorescent nanoparticle characterization. A 543 nm HeNe laser was used as the excitation source. Figure 2.3b shows that the average hydrodynamic sizes obtained from FCS fits of Cy3-labeled SNPs synthesized by homogenous growth

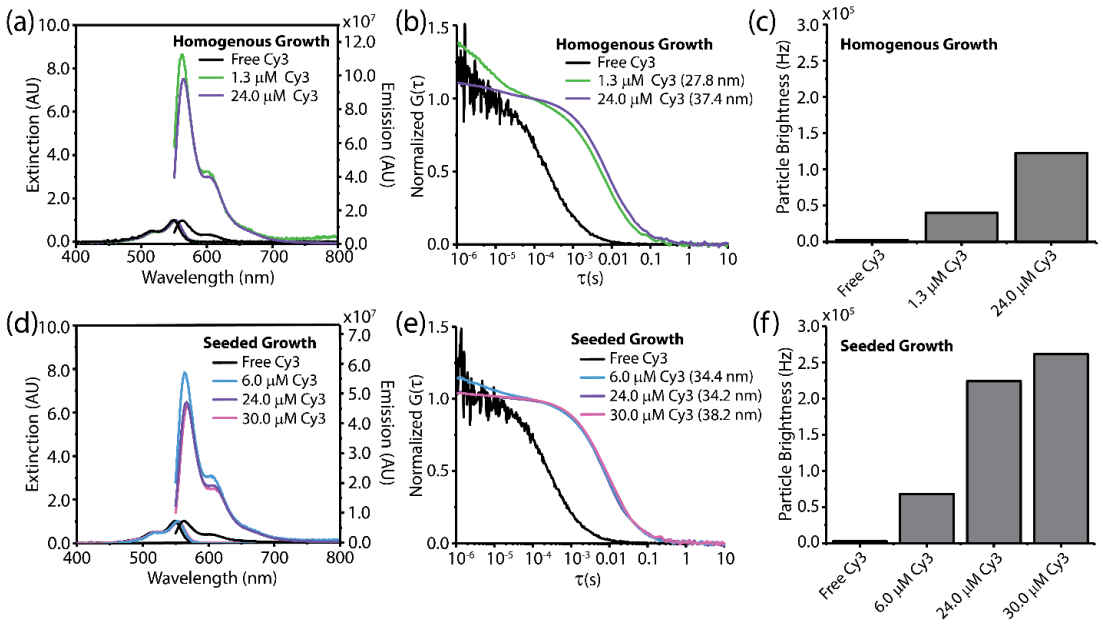

Figure 2.3. Characterization of fluorescent SNPs synthesized by (a-c) homogenous and (d-f) seeded growth. (a, d) Absorbance and emission spectra, (b, e) FCS curves, and (c, f) FCS-derived per particle brightness values for SNPs synthesized using homogenous or seeded growth and varying Cy3/APTES or Cy3/AEAPTMS concentrations, respectively. Noise levels of FCS curves for free dye in (b) and (e) are higher than for particles due to substantially increased particle brightness, see (a) and (d).

increase as Cy3/APTES concentration is increased. Using 1.3 μM and 24.0 μM Cy3/APTES resulted in SNPs with diameters of 27.8 nm and 37.4 nm, respectively.

The difference in particle size measured by FCS as a function of Cy3/APTES concentration is corroborated in the corresponding GPC elugrams (Figures A1c and d) of the particles. In this system, a typical GPC elugram exhibits three peaks as a function of elution volume, corresponding to particle aggregates, PEGylated particle product, and free reactants, respectively[18]. Shorter elution times were observed for SNPs prepared using 24.0 μM Cy3/APTES (Figure A1d), indicating increased particle size relative to SNPs synthesized using 1.3 μM Cy3/APTES (Figure A1c). Transmission electron microscopy (TEM) images and corresponding size analysis (Figure A1a, b) corroborate the APTES-dependent size difference observed in FCS and GPC. Since the Cy3/APTES conjugate is prepared using a 10-fold excess of aminosilane and the reaction is performed at basic pH, these observations are consistent with early aggregation of negatively charged silica clusters (*vide supra*) facilitated by increasing concentrations of positively charged APTES, resulting in increased average particle sizes[25, 31]. Interestingly, the GPC elugram in Figure A1d for particles from the higher dye concentration (24.0 μM Cy3/APTES) exhibits a more skewed particle size peak. This suggests that higher concentrations of positively-charged APTES leads to continuous secondary particle formation, as more and more TEOS from the top layer hydrolyzes and diffuses into the water phase, thereby increasing particle size dispersity[32]. Despite increased polydispersity, Figure 2.3c clearly demonstrates that SNPs with increasing average fluorescence intensity levels could be obtained by adjusting the concentration of Cy3-silane used during particle synthesis, resulting in SNPs that are 15 and 47 times brighter than free Cy3 dye. Unfortunately, due to extreme particle size dispersity at even higher APTES levels, the

concentration of Cy3-silane could not be increased beyond 24.0 μM without complete loss of particle uniformity.

Accurate identification of "high" and "low" intensity tags requires minimal overlap between single particle intensity distributions. We therefore evaluated batches of fluorescent dye-loaded SNPs for use as an intensity barcode, assessing single particle analysis based intensity distributions using total internal reflection fluorescence (TIRF) microscopy[14]. For imaging, biotinylated SNPs were immobilized on a streptavidin-coated glass substrate. Small numbers of biotin molecules were introduced to SNP surfaces during PEGylation using α,ω-heterobifunctional PEG molecules (Figures 2.2a and c). Streptavidin-coated substrates were prepared using a previously established method[33] with slight modifications (see Supporting Information). Briefly, a thiol-coated substrate (blue in Figure 2.2b) was prepared by silanization of a glass slide (gray) using mercaptopropyltrimethoxysilane (MPTMS). N-γ-maleimidobutyryl-oxysuccinimide ester (GMBS) was attached to the thiol-coated substrate using its reactive maleimide group and the NHS ester group (green) at the opposite end of the GMBS was coupled to a primary amine on the streptavidin molecule (purple). Substrates were rinsed thoroughly after each step to remove unreacted chemicals. Imaging was performed over a 51.1 x 51.1 μm^2 area containing ~100 SNPs. Single images were acquired for 100 msec. After image acquisition, a spot detection algorithm was used to identify individual SNPs. The background level and full width at half maximum (FWHM) of spots in the x- and y-directions were derived from Gaussian fits. Spot intensity was defined as the background-corrected sum over all pixels within the FWHM[34] (see Supporting Information and Figures A2 and A3 for details).

We compared spot intensities from Cy3-labeled SNPs synthesized using the homogenous growth approach and 1.3 μM or 24.0 μM Cy3/APTES. The resulting

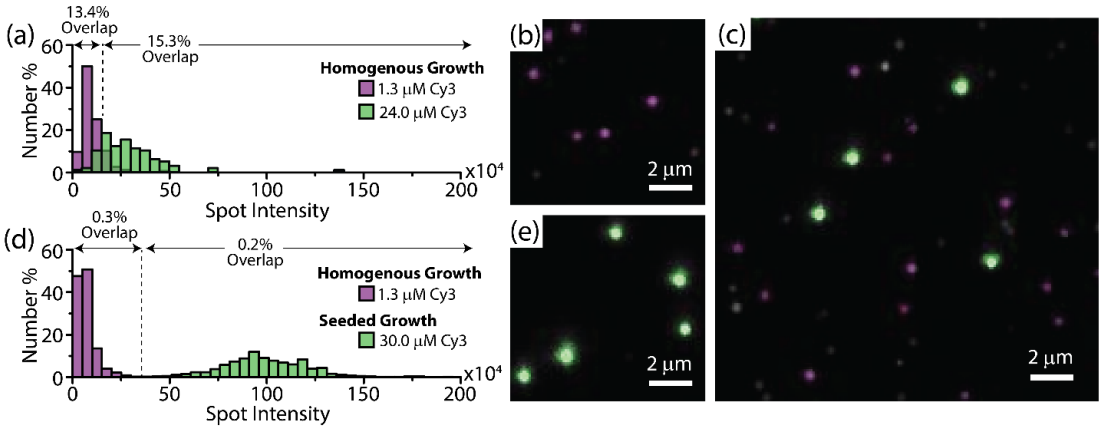

Figure 2.4. Comparison of fluorescence intensity levels for low and high dye-loaded SNPs as revealed by single particle imaging using TIRF microscopy. (a, d) Single-particle intensity distributions for SNPs. The SNPs shown in (a) are prepared by homogenous growth, using 1.3 μM (purple) and 24.0 μM (green) Cy3/APTES. Overlap for high Cy3-loaded SNPs is defined as the fraction of particles with spot intensity below a threshold value (dashed black lines). Overlap for low Cy3-loaded SNPs is calculated as the fraction of particles with spot intensity above the same threshold value. In (d), low Cy3-loaded SNPs are again prepared by homogenous growth, using 1.3 μM (purple) Cy3/APTES. High Cy3-loaded SNPs are synthesized using seeded growth and 30.0 μM Cy3/AEAPTMS (green). (b, c, e) Single particle fluorescence images of (b) only the low, (e) only the high, and (c) mixtures of the low and high Cy3-loaded SNPs shown in (d). Spots above and below the threshold shown in (d) are colored green and purple, respectively.

histograms (Figure 2.4a), while showing an overall intensity increase for high Cy3-loaded particles, consistent with the increased average brightness/particle values measured using FCS (Figure 2.3c), substantially overlap. To benchmark the performance of these SNPs, we quantified the overlap between the two intensity distributions shown in Figure 2.4a. First, a threshold value was identified that minimizes overlap between high and low intensity distributions (dashed black line in Figure 2.4a). Overlap for high Cy3-loaded SNPs was then defined as the fraction of particles with spot intensity below that threshold value, while overlap for low Cy3-loaded SNPs was calculated as the fraction of particles with spot intensity above the threshold. Using these criteria, 15.3% and 13.4% overlap were calculated for high and low intensity distributions, respectively. This result indicates that on a single particle level, nearly 30% of particles cannot be unambiguously identified based on intensity alone. Clearly, such low identification accuracy would preclude use of these SNPs as an intensity barcode.

To overcome these limitations of the homogenous growth approach (*i.e.* high concentrations of Cy3/APTES causing extreme polydispersity in SNPs and limited separation from low particle brightness distributions), we introduced a second synthesis approach which we will refer to as the "seeded" growth method. Here, undyed SNPs with sizes < 20 nm were used as seeds for further particle growth (Figures 2.2a and d). Furthermore, Cy3 dye was covalently coupled to N-(2-aminoethyl)-3-aminopropyltrimethoxysilane (AEAPTMS) instead of APTES. The comparatively fast hydrolysis kinetics of AEAPTMS[26] obviates the prolonged continued growth used to achieve high dye-loadings in the homogenous growth approach. Thus, to maintain relatively small particle sizes (< 40 nm), only one additional TEOS growth step was used. SNPs were again PEGylated prior to purification using GPC. Seeded growth of SNPs was monitored using dynamic light

scattering (DLS), demonstrating that incremental shell growth results in steadily increasing particle sizes (see Figure A.4a in Supporting Information). Figure 2.3e shows that as compared to SNPs synthesized by homogenous growth (Figure 2.3b), the hydrodynamic sizes of SNPs synthesized by seeded growth do not vary significantly with increasing Cy3/AEAPTMS concentration. Using 6.0 μM, 24.0 μM, and 30.0 μM Cy3/AEAPTMS resulted in SNPs with diameters of 34.4 nm, 34.2 nm, and 38.2 nm, respectively. Using the same concentration of Cy3-silane, SNPs prepared by seeded growth also exhibit more symmetric particle peaks in GPC (Figure A.4e) than SNPs synthesized by homogenous growth (Figure A1d), suggesting that fewer secondary particles are formed. TEM images corroborated that these SNPs are narrowly dispersed (see Figure A.4c and d in Supporting Information).

Figure 2.3d shows that Cy3-labeled SNPs synthesized by seeded growth and using increasing amounts of Cy3/AEAPTMS exhibit per dye fluorescence enhancements of 6 to 7 times. As in SNPs synthesized via homogenous growth, increasing average brightness/particle was achieved by increasing the concentration of Cy3/AEAPTMS conjugate. Figure 2.3f shows that Cy3-labeled SNPs using 6.0 μM, 24.0 μM, and 30.0 μM Cy3/AEAPTMS are 28, 91, and 106 times brighter, respectively, than free Cy3 dye. Comparison between Figures 2.3c and f shows that from 24.0 μM Cy3-silane concentration upwards, the seeded growth approach is a more efficient method of generating bright fluorescent tags. Cy3-labeled SNPs prepared by seeded growth using 24.0 μM Cy3/AEAPTMS are nearly 2 times brighter than those synthesized by homogenous growth using Cy3/APTES at the same concentration, even though the per dye brightness is slightly decreased in these particles. This increased dye incorporation efficiency is attributed to reduced rates of secondary particle nucleation/formation achieved using the seeded growth approach and to the relatively fast reaction rates of Cy3/AEAPTMS as compared to

Cy3/APTES. As this result could not be achieved with Cy3/APTMS (data not shown), we hypothesize that the secondary amines present in AEAPTMS may also contribute to the enhanced association with the growing SNPs by hydrogen bonding to silica surface silanol groups[35], further increasing the incorporation efficiency of Cy3/AEAPTMS relative to Cy3/APTES.

The advantages of the seeded growth of fluorescent SNPs using Cy3/AEAPTMS (*i.e.* increased brightness/particle in FCS) particularly manifested in TIRF microscopy. Single particle intensity distributions for SNP batches synthesized using 6.0 μM, 24.0 μM, and 30.0 μM Cy3/AEAPTMS show that an overall intensity increase is reproducibly observed as the concentration of Cy3/AEAPTMS is increased (see Figure S5 in the Supporting Information). Importantly, single particle intensity distributions for batches generated using the seeded growth approach and 24.0 μM Cy3/AEAPTMS (Figure S5b) are also shifted to higher spot intensities as compared to particle batches derived from the homogeneous growth approach at the same concentration of Cy3/APTES (Figure 2.4a). Designating SNP batches synthesized by homogenous (1.3 μM Cy3/APTES) and seeded growth, (30.0 μM Cy3/AEAPTMS) as low and high intensity level tags, we approach near perfect identification accuracy. Figure 2.4d shows that single particle intensity distributions exhibit 0.2 to 0.3% overlap for low (purple) and high (green) Cy3-loaded SNPs, indicating that >99% of SNPs are unambiguously identifiable based on intensity alone. We applied our intensity barcoding scheme to fluorescence images of mixed high and low intensity probes (Figure 2.4c). Spots above and below the intensity threshold defined in Figure 2.4d are colored green and purple, respectively. Comparison to images of only high (Figure 2.4e) or only low intensity (Figure 2.4b) probes illustrates that highly accurate intensity-based identification can be achieved. While for these proof-of-principle demonstrations, batches from homogeneous and seeded growth were compared, we

expect that after careful parameter optimization other combinations, for example of two batches synthesized using seeded growth, will show similar results.

Conclusions

We have described two batch approaches for the synthesis of fluorescent silica nanoparticles using either homogenous or seeded growth. Controlled fluorescence intensity levels can be achieved in these systems simply by varying the concentration of a Cy3-silane conjugate in the batch. We have shown that the precise spatial distributions of dyes within particles can be controlled by silica shell growth, minimizing self-quenching of dyes even in highly dye-doped particles. Comparison of the two approaches highlights that the nucleation of secondary particles during shell growth presents a major challenge in the synthesis of highly dye-doped SNPs with narrowly distributed single particle fluorescence intensity distributions. Using the seeded growth approach, we have decreased the rate of secondary nucleation. Simultaneously, we have increased the rate of Cy3 incorporation by choice of silane linker (e.g. AEAPTMS versus APTES), minimizing the effects of secondary nucleation in this system.

We find that single particle analysis based fluorescence intensity distributions of SNPs synthesized in these ways are well separated and can therefore be used as an intensity-based barcode. These SNPs are small (< 40 nm), highly biocompatible, and readily functionalizable, making them ideal fluorescent tags for imaging in living biological systems. We have used a single fluorescent dye (Cy3) as proof-of-concept, but expect that our results can be extended to combinations of dyes with multiple spectral colors, greatly increasing the number of SNP tags that can be imaged in parallel using conventional fluorescence microscopy. Additionally, since this strategy relies on the improved incorporation efficiency of a silane linker, we expect that

similar results can be achieved using a range of organic fluorescent dyes and linker chemistries, providing an efficient route to encapsulation of these often-expensive molecules.

REFERENCES

1. Lichtman, J. W.; Conchello, J. *Nat. Meth.* **2005**, *2*, 910 – 919.
2. Joo, C.; Balci, H.; Ishitsuka, Y.; Buranachai, C.; Ha, T. *Annu. Rev. Biochem.* **2008,** *77*, 51 – 77.
3. Tsien, R. Y. *Annu. Rev. Biochem.* **1998**, *67*, 509 – 544.
4. Ow, H.; Larson, D.; Srivastava, M.; Baird, B., Webb, W.; Wiesner U. *Nano Lett.* **2005**, *5*, 113 - 117.
5. Medintz, I. L.; Uyeda, H. T.; Goldman, E. R.; Mattoussi, H. *Nat. Mater.* **2005**, *4*, 435 – 446.
6. Lubeck, E.; Cai, L. *Nat. Methods.* **2012**, *9*, 743 – 748.
7. Woehrstein, J. B.; Strauss, M. T.; Ong, L. L.; Wei, B.; Zhang, D. Y.; Jungmann R.; Yin P. *Sci. Adv.* **2017**, *3*, 1602128.
8. Han, M.; Gao, X.; Su, J. Z.; Nie, S. *Nat. Biotechnol.* **2001**, *19*, 631 – 635.
9. Zhang, Y. Z.; Kemper, C. R.; Haugland, R.P. Microspheres with fluorescent spherical zones. US 5,786,219 (1998).
10. Banerjee, S.; Georgescu, C.; Daniels, E. S.; Dimonie, V. L., Seul, M. Production of dyed polymer microparticles. US 6,964,747 (2005).
11. Forster, T.; *Ann. Phys.* **1948**, *437*, 55 – 75.
12. Um, S. H.; Lee, J. B.; Kwon, S. Y.; Li, Y.; Luo D. *Nat. Protoc.* **2006**, *1*, 995 – 1000.
13. Wang, L.; Tan, W. *Nano Lett.* **2006**, *6*, 84 – 88.
14. Wu, C.; Hansen, S. J.; Hou, Q.; Yu, J.; Zeigler, M.; Jin, Y.; Burnham, D. R.; McNeill, J. D.; Olson, J. M.; Chiu, D. T. *Angew. Chem. Int. Ed.* **2011**, *50*, 3430 – 3434.
15. Jungmann, N.; Schmidt, M.; Ebenhoch, J.; Weis, J.; Maskos, M. *Angew. Chem., Int. Ed.* **2003**, 42, 1714
16. Ow, H.; Larson, D.; Srivastava, M.; Baird, B., Webb, W.; Wiesner U. *Nano Lett.* **2005**, *5*, 113 - 117.

17. Graf, C.; Vossen, D. L. J.; Imhof, A.; van Blaaderen, A. *Langmuir*. **2003**, *19*, 6693 – 6700.
18. Ma, K.; Mendoza, C.; Werner-Zwanziger, U.; Zwanziger, J.; Wiesner, U. *Chem. Mater.* **2015**, *27*, 4119 – 4133.
19. Yokoi, T.; Sakamoto, Y.; Terasaki, O.; Kubota, Y.; Okubo, T.; Tatsumi, T. *J. Am. Chem. Soc.* **2006**, *128*, 13644 – 13665.
20. Hartlen, K. D.; Athanasopoulos, A. P. T.; Kitaev, V. *Langmuir*. **2008**, *24*, 1714-1720.
21. Ma, K.; Sai, H.; Wiesner, U. *J. Am. Chem. Soc.* **2012**, *134*, 13180 – 13183.
22. Ma, K.; Zhang, D.; Cong, Y.; Wiesner, U. *Chem. Mater.* **2016**, *28*, 1537 – 1545.
23. Ma, K.; Wiesner, U. *Chem. Mater.* **2017**, *29*, 6840 – 6855.
24. Schubbe, S.; Cavelius, C.; Schumann, C.; Koch, M.; Kraegeloh, A. *Adv. Eng. Mater.* **2010**, *12*, 417 – 422.
25. Carcouët, C. C. M. C.; van de Put, M. W. P.; Mezari, B.; Magusin, P. C. M. M.; Laven, J.; Bomans, P. H. H.; Friedrich, H.; Catarina, A.; Esteves, C.; Sommerdijk, N. A. J. M.; van Benthem, R. A. T. M.; de With, G. *Nano Lett.* **2014**, *14*, 1433 – 1438.
26. Wang, J.; Sugawara-Narutaki, A.; Fukao, M.; Yokoi, T.; Shimojima, A.; Okubo, T. *ACS Appl. Mater. Interfaces*, **2011**, *3*, 1538 – 1544.
27. Larson, D. R.; Ow, H.; Vishwasrao, H. D.; Heikal, A. A.; Wiesner, U.; Webb, W. W. *Chem. Mater.* **2008**, *20*, 2677 – 2684.
28. Muddana, H. S.; Morgan, T. T.; Adair, J. H.; Butler, P. J. *Nano Lett.* **2009**, *9*, 1559 – 1566.
29. Magde, D.; Elson, E.; Webb, W. W. *Phys. Rev. Lett.* **1972**, *29*, 705.
30. Yin, Y.; Yuan, R.; Zhao, X. S. *J. Phys. Chem. Lett.* **2013**, *4*, 304 – 309.
31. Mizutani, T.; Nagase, H.; Fujiwara, N.; Ogoshi, H. *Bull. Chem. Soc. Jpn.* **1998**, *71*, 2017 – 2022.
32. Chen, C; Hayakawa, C; Shirosaki, Y.; Fujii, E.; Kawabata, K; Tsuru, K; Osaka, A. *J. Am. Ceram. Soc.* **2009**, *92*, 2074 – 2082.

33. Ngundi, M. M.; Shriver-Lake, L. C.; Moore, M. H.; Lassman, M. E.; Ligler, F. S.; Taitt, C. R. *Anal. Chem.* **2005**, *77*, 148 – 154.

34. Willing, K. I.; Rizzoli, S. O.; Westphal, V.; Jahn, R.; Hell, S.W. *Nature*. **2006**, *440*, 935 – 939.

35. Kroger, N.; Deutzmann, R.; Bergsdorf, C.; Sumper, M. *Proc. Natl. Acad. Sci.* **2000**, *97*, 14133 – 14138.

CHAPTER 3

CONTROLLING FLUORESCENT DYE INCORPORATION IN BATCH REACTIONS OF SILICA NANOPARTICLES

Abstract

The development of nano-sized, fluorescence intensity-based barcodes can greatly enhance the multiplexing capabilities of fluorescence microscopy. Here, we provide a full account of the synthesis of a sub-40 nm, intensity-based fluorescent silica nanoparticle barcode. In this study, the synthetic parameters that govern heterogeneities in batch reactions of silica nanoparticles are investigated. A key synthesis feature is the use of a seeded growth approach to minimize formation of low dye-loaded secondary particles. Additional variations of the synthesis conditions include the seed concentration and the organosilane linker used for covalent encapsulation of dyes inside the silica matrix. Heterogeneities within batches of nanoparticles are mapped using single particle fluorescence microscopy, gel permeation chromatography, and transmission electron microscopy. Results establish critical parameters enabling batch synthesis of fluorescent silica nanoparticles with well-separated single-particle intensity distributions. Insights gained from this study may be transferred to the design of other nanoparticle-based intensity barcodes.

---

[*] Prepared for Submission as: Teresa Kao, Ferdinand Kohle, Kai Ma, Tangi Aubert Alexander Andrievsky, Ulrich Wiesner. *Controlling Fluorescent Dye Incorporation in Batch Reactions of Silica Nanoparticles.*

Introduction

As a result of rapidly advancing technologies, fluorescence microscopy now provides a powerful approach for single molecule detection[1]. One major advantage of fluorescence microscopy is that multiple target molecules can be imaged simultaneously by attaching spectrally distinct fluorescent tags[2], such as organic dyes, fluorescent proteins[3, 4], or nanoparticles[5, 6]. However, studies of more complex systems remain limited by the number of probes that can be simultaneously imaged and reliably distinguished on the single particle level, using commercially available microscopes[7]. Combinatorial labeling strategies have been used successfully to generate color- and intensity-based barcodes in fluorescent dye-doped microbeads[8-10], but implementation in nano-sized systems remains challenging due to sample heterogeneity. State of the art efforts have used programmable materials to circumvent these issues, generating nano-sized DNA- and RNA-based optical barcodes with precisely controlled numbers of organic dyes[7, 11]. However, only limited success has been achieved in nanoparticle-based systems[12, 13].

Fluorescent dye-doped silica nanoparticles (SNPs) have been used extensively in bioimaging applications, because silica is optically transparent and highly biocompatible[5]. Recent advances in fabrication have extended the range of accessible sizes to below 10 nm[14]. Additionally, facile surface modification protocols provide routes to stable, multi-functional particles[15, 16]. Precise control of particle size and surface functionality make SNPs ideal candidates for biological imaging applications. For example, a class of sub-10 nm PEGylated fluorescent SNPs (Cornell Dots or C Dots) were approved by the FDA in 2011 as an investigational new drug for cancer diagnostics in first in-human clinical trials[17]. Fluorescent dye-doped SNPs have also been shown to have improved photophysical properties as compared to the constituent fluorophores, including increased brightness and photostability[5, 18].

We have recently reported the batch synthesis of SNPs with controlled fluorescence intensity levels and sizes below 40 nm[19]. SNPs synthesized with high and low intensity levels could be used as an intensity barcode in single-particle fluorescence images, with near perfect identification accuracy. In this article, we provide a full account of these results. We use fluorescence correlation spectroscopy (FCS) to demonstrate that SNPs with increasing average fluorescence brightness may be generated by co-condensation of silica precursors with increasing concentrations of fluorescent dye-silanes. We investigate the effects of the organosilane molecules used in preparation of fluorescent dye-conjugates on particle formation, using a combination of gel permeation chromatography (GPC) and transmission electron microscopy (TEM). An optimized synthesis protocol is described, in which a seeded growth approach is used to minimize secondary particle formation. Due to the high cost of the fluorescent dyes, the initial seed concentration is also optimized to reduce the amount of dye required for generating highly fluorescent SNPs. Organosilane linker chemistry is introduced as an additional control parameter for increasing the efficiency of organic fluorescent dye incorporation into SNPs. Heterogeneities within particle batches are mapped using single particle fluorescence microscopy. Finally, we demonstrate that under optimized synthesis conditions, SNPs with well-separated single particle intensity distributions can be achieved.

Experimental

Materials

All chemicals were used as received without further purification. Deionized water (Milli-Q, 18.2 MΩ) was used throughout. Cy3 NHS ester was purchased from GE Healthcare. 3-aminopropyltriethoxysilane (APTES, ≥97%), 3-aminopropyltrimethoxysilane (APTMS, ≥96%), N-(2-aminoethyl)-3-

aminopropyltrimethoxysilane (AEAPTMS, 95%), 3-mercaptopropyltrimethoxysilane (MPTMS, ≥96%), and methoxy-terminated poly(ethylene glycol) (PEG-silane, molar mass ~500 g/mol) were purchased from Gelest Inc. Tetraethyl orthosilicate (TEOS, ≥99%), l-arginine (≥99%), ammonium hydroxide (NH_4OH, 29%), isopropanol (anhydrous, 99.5%), ethanol (absolute, anhydrous), and dimethyl sulfoxide (DMSO) were purchased from Sigma Aldrich. α,ω-heterobifunctional poly(ethylene glycol) with maleimide and biotin groups (mal-PEG-biotin, molar mass ~922 g/mol) was purchased from Quanta BioDesign Inc. Phosphate buffered saline (PBS, sterile) was purchased from Amresco Inc. Streptavidin and N-γ-maleimidobutyryl-oxysuccinimide ester (GMBS) were purchased from Life Technologies.

Synthesis of Fluorescent SNPs by Homogenous Growth.

Cy3/APTES conjugate was prepared by reacting Cy3 NHS ester with a 10-fold excess of APTES in DMSO. Conjugation reactions were conducted overnight, under an inert nitrogen environment. In a typical synthesis, l-arginine (0.012 g) was dissolved in deionized water (9.32 mL), stirring slowly (150 rpm) in a 20 mL borosilicate scintillation vial at 60°C. 4 mm x 12.7 mm PTFE coated stir bars were used in all particle syntheses. Homogenous growth of dye-doped cores was achieved by adding Cy3/APTES dropwise into the stirring solution, followed by 135 μL TEOS, added slowly in a thin layer at the top surface of the reaction. Cores were formed after 8 hours. SNPs with increasing fluorescence intensity levels were prepared by increasing the concentration of Cy3/APTES (1.3 μM to 24.0 μM) added during nucleation. An additional 3 blank silica shells (135 μL TEOS per shell) were added in 8 hour intervals. The reaction was left stirring at 150 rpm for 24 hours after the final TEOS addition.

Synthesis of Fluorescent SNPs by Seeded Growth.

Cy3-silane conjugates were prepared by reacting Cy3 NHS ester with a 10-fold excess of APTES (Cy3/APTES), APTMS (Cy3/APTMS), or AEAPTMS (Cy3/AEAPTMS) in DMSO. All conjugation reactions were conducted overnight, in an inert nitrogen environment. To prepare seed particles, l-arginine (0.012 g) was dissolved in deionized water (9.32 mL), stirring slowly (150 rpm) in a 20mL borosilicate scintillation vial at 60°C. 4 mm x 12.7 mm PTFE coated stir bars were used in all particle syntheses. TEOS was added slowly in a thin layer to the top surface of the reaction. An additional 4 TEOS additions (3 x 135 μL and 1 x 143.4 μL) were made at 8 hr intervals. The reaction was left stirring for 24 hours after the final TEOS addition. In a typical seeded growth, 2 mL of seed particles was added to 8 mL of deionized water stirring slowly (150 rpm) in a 20 mL scintillation vial at 60°C. The Cy3-silane conjugate was added dropwise into the stirring solution, followed by 143.5 μL TEOS, added slowly in a thin layer to the top surface of the reaction. One additional TEOS (143.5 μL) addition was made after 24 hrs. SNPs with increasing fluorescence intensity were prepared by varying the concentration of Cy3-silane from 1.3 μM to 30.0 μM. The reaction was left stirring at 150 rpm for 24 hours after the final TEOS addition.

PEGylation of Fluorescent SNPs.

Biotin-PEG-silane conjugate was prepared by reacting mal-PEG-biotin (100 mg/mL in DMSO) with 1.1 equivalents of MPTMS in DMSO. Conjugation reactions were conducted overnight, in an inert nitrogen environment. Before PEGylation, native solutions of SNPs were diluted 5-fold in deionized water and adjusted to pH 10 using NH_4OH. For a 10mL reaction volume, a mixture of 100 μL methoxy-terminated PEG-silane and 12.5 μL biotin-PEG-silane was added. Solutions were rapidly stirred

(600 rpm) at room temperature during PEG addition and left stirring overnight. Finally, the temperature was increased to 80°C with no stirring for 12 hours.

TIRF Substrate Preparation.

35 mm glass bottom dishes (No. 15 coverslip, 22 mm glass diameter) were functionalized with streptavidin using a previously established protocol with slight modifications[20]. Dishes were rinsed successively using isopropanol and deionized water and dried using nitrogen. Substrates were then plasma cleaned for 10 minutes using a Harrick Plasma Generator (PDC32G) operated at high power. 500 μL of a 0.2M solution of MPTMS in ethanol was added to each dish and incubated for 30 minutes to generate a thiol-coated surface. After rinsing several times with ethanol to remove free MPTMS, 250 μL of 4 mM GMBS in ethanol was added to each dish and incubated for 30 minutes. GMBS was attached to the thiol-coated substrate using its reactive maleimide group, leaving the NHS ester at the opposite end free to react with primary amines on the streptavidin molecule. The substrate was rinsed several times with ethanol to remove free GMBS and then again using PBS buffer to remove ethanol. 100 μL of streptavidin (50 μg/mL) was immobilized on the surface of the GMBS-activated glass by incubation for 2 hours. Finally, free streptavidin was removed by rinsing several times with PBS. Substrates were used immediately or stored in PBS at 4ºC.

3.2.6 Characterization.

Gel Permeation Chromatography (GPC) purification was performed using a BioLogic LP system equipped with a 275 nm UV detector and using Sephacryl 400 resin from GE Healthcare, as previously described for PEGylated SNPs[14]. Prior to GPC purification, PEGylated samples were cleaned 3 times using a 30 MWCO spin-

filter (Vivaspin 20) to remove unreacted chemicals (e.g. free dye). Transmission electron microscopy (TEM) images were taken using a FEI Tecnai T12 Spirit microscope operated at an acceleration voltage of 120 kV. TEM grids were prepared by drop casting from native synthesis solutions prior to PEGylation. Absorbance and emission spectra were measured using a Varian Cary Model 5000 spectrophotometer and Photon Technologies International Quantamaster spectrofluorometer, respectively. Intrinsic scattering from SNPs was estimated by fitting the absorbance from 350 – 450 nm, a region of the spectra which is not affected by Cy3 absorbance, and subtracted from the excitation spectra of fluorescent SNPs[21]. Fluorescence correlation spectroscopy (FCS) measurements were conducted using a home-built FCS setup. A 543 nm HeNe laser was used as a laser source for the Cy3 fluorophore. As previously described, the hydrodynamic size, brightness per particle, and particle concentration were obtained from single component diffusion fits of the FCS autocorrelation curves[5, 18, 22].

3.2.7 Fluorescence Imaging and Intensity Analysis.

Before each imaging experiment, biotinylated SNPs were attached to streptavidin-coated substrates by incubation for several minutes. Unbound SNPs were removed by rinsing with PBS. All imaging experiments were performed in PBS. Fluorescence imaging was performed using an inverted Zeiss Elyra microscope operated in total internal reflection fluorescence (TIRF) mode. A 1.46 NA 100X objective was used for illumination and light collection. A 543 nm laser was used as an excitation source for the Cy3 fluorophore and the resulting fluorescent signal was filtered using a 570 - 620 nm band pass filter. Experiments were conducted using 4.2 mW laser power, measured at the objective. In a typical experiment, a series of 50 images (100 ms/frame) was acquired, beginning just before the excitation laser was

turned on. “Definite focus” focal-drift compensation was used during image acquisition. Images acquired before the laser power stabilized (~700 ms) were discarded and image analysis was performed only on the first image of the remaining stack. Image analysis was performed using a self-written MATLAB program[19]. Spot detection and subsequent spot intensity analysis was performed inside a 256 x 256 pixel^2 area to minimize variations in excitation power and image focus. Spots with peak intensity (I_{Peak}) above a threshold value ($I_{Threshold}$) were centered in a 17 x 17 pixel^2 region of interest (ROI). $I_{Threshold}$ was optimized to reduce false positive identification of low intensity substrate contaminants and held constant for all experiments performed using a given batch of substrates. For this reason, only imaging experiments performed using substrates from the same batch were compared directly. ROIs containing multiple spots were excluded from analysis according to previously defined criteria[19]. The background level and FWHM for individual spots were determined from Gaussian fits centered on I_{Peak} in the x- and y- directions. A single background value was calculated by averaging background values obtained from the x- and y- spot intensity profiles. Spot intensity was calculated as the background-corrected sum over all pixels inside an approximately circular area, defined using full width at half maximum, $FWHM_x$ and $FWHM_y$, as the x- and y-axis lengths of an ellipse[23]. In this study, laser power was optimized to maximize the signal to noise ratio, while maintaining narrow spot intensity distributions (Figure S1).

3.3 Results and Discussion

In this article, we describe two methods for preparing highly fluorescent dye-doped silica nanoparticles (SNPs) with sizes below 40 nm. In both cases, l-arginine is used as a base catalyst for SNP formation in aqueous media at a reaction temperature of 60°C. A thin layer of tetraethoxysilane (TEOS) added to the top surface of the

aqueous phase serves as the silica source[24, 25, 26]. In the first method, fluorescent dye-doped SNP cores are formed by co-condensation of a Cy3-silane conjugate and TEOS. Additional shells are added using TEOS only. In the second method, the dye-silane conjugate and TEOS are introduced during continued growth of monodisperse, undyed seed particles with sizes < 20 nm. To distinguish between the two methods described here, we refer to the first method as "homogenous growth" and the second method as "seeded growth." In the following sections, we compare the size dispersity and single particle intensity distributions of SNPs prepared using these two approaches. Variations of the synthesis parameters in the seeded growth approach, including seed particle concentration and details of the organosilane linker used to prepare the Cy3-silane conjugate, are employed in the development of optimized synthesis conditions for achieving high and low dye-loaded SNPs with well-separated intensity distributions.

Fluorescent SNPs prepared by homogenous growth.

A series of SNPs with increasing fluorescence brightness was prepared as previously described[19]. Covalent attachment of Cy3 NHS ester dye to SNPs was achieved using aminopropyltriethoxysilane (APTES) as a linker[5]. SNPs prepared by co-condensation of increasing concentrations of the Cy3/APTES conjugate and 65 mM TEOS served as cores for continued growth. Three additional silica shells (65 mM TEOS per shell) were added prior to PEGylation.

Figure 3.1A shows intensity-matched absorption and corresponding emission spectra for this series of SNPs. PEGylated SNPs were cleaned by centrifugation and subsequently purified using GPC to remove aggregates and unreacted dyes prior to measurement. As previously reported and analyzed[5, 18, 27, 28], the per dye fluorescence of the Cy3 dye is dramatically increased upon encapsulation inside the rigid silica

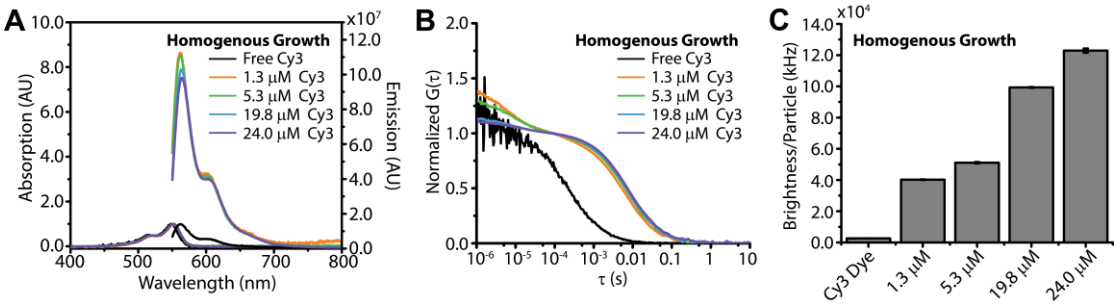

Figure 3.1. Fluorescent SNPs prepared by homogenous growth. (A) Absorbance and emission spectra, (B) FCS autocorrelation curves, and (C) FCS brightness/particle for SNPs prepared by homogenous growth using 1.3 µM, 5.3 µM, 19.8 µM, and 23.9 µM Cy3. The noise level in the FCS curve for free Cy3 in (B) is higher than for particles due to dramatically increased particle brightness, see (C). Data corresponding to 1.3 µM and 24.0 µM reproduced from ref. 19.

matrix. Comparison of the free Cy3 dye to Cy3-loaded SNPs in Figure 3.1A, shows that per dye quantum enhancements of 7 to 8 are observed upon encapsulation. Only slightly lowered quantum enhancements are observed for SNPs as a function of increasing Cy3-silane concentration, suggesting that dyes remain essentially unquenched[18]. SNPs were further characterized using fluorescence correlation spectroscopy (FCS). Using FCS, fluctuations in fluorescence intensity resulting from diffusion into and out of the detection volume of a confocal setup could be autocorrelated and fit using a single-component model for diffusion to measure average hydrodynamic particle size, concentration, and brightness[5, 18, 22]. FCS measurements showed that increasing concentrations of Cy3/APTES resulted in continuously increasing particle sizes (Figure 3.1B) and the desired increase in average brightness per particle (Figure 3.1C). FCS based hydrodynamic diameters of SNPs prepared by homogenous growth, using 1.3 μM, 5.3 μM, 19.8 μM, and 24.0 μM Cy3/APTES were 27.8 nm, 33.4 nm, 35.6 nm, and 37.4 nm, respectively, with FCS derived brightness levels 15, 29, 38 and 47 times higher, respectively, than the constituent Cy3 dye in FCS.

To explain the Cy3/APTES concentration-dependent trend in particle size, we considered the formation mechanism of SNPs prepared by homogenous growth[30, 31]. As previously described, the formation of SNPs at basic pH and elevated temperature proceeds by rapid aggregation of small (< 2 nm), negatively-charged silica clusters[14, 30]. In this system, slow hydrolysis and diffusion of TEOS from the top layer into the aqueous reaction phase provides a continuous stream of silica precursors that form these small clusters. Figure 3.2A shows schematic illustrations of the formation mechanism for undyed SNPs at time points before (t = 1) and after (t = 2) the critical concentration for cluster aggregation is reached. Further growth of SNPs occurs by continuous silica cluster addition[30].

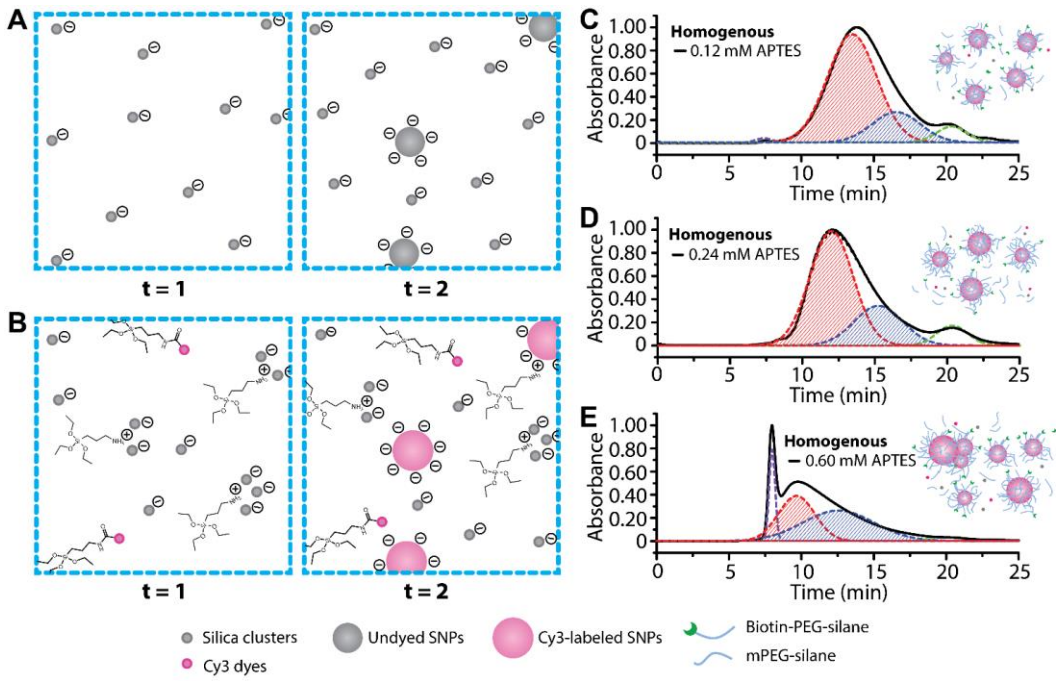

Figure 3.2. Characterization of APTES-induced size dispersity. (A, B) Schematic illustrations of the growth processes of SNPs prepared by homogenous growth, synthesized in (A) the absence or (B) the presence of the Cy3/APTES conjugate (compounds not to scale). (A) Undyed SNPs prepared using TEOS alone under basic reaction conditions are formed from small (< 2nm), negatively-charged silica clusters (t = 1)[30]. A continuous feed of hydrolyzed TEOS into solution facilitates further growth of SNPs by aggregation of these silica clusters (t = 2)[30]. (B) The excess aminosilane used in the preparation of the Cy3/APTES conjugate is positively-charged and induces early aggregation of the negatively-charged silica clusters (t = 1), resulting in the formation of larger Cy3-labeled SNPs (t = 2). By the same mechanism, APTES that is not consumed during SNP formation also induces secondary nucleation during growth (t = 2). (C-E) GPC elugrams for SNPs prepared by homogenous growth using 24.0 μM Cy3-silane. APTES concentrations used during preparation of Cy3-silane conjugate were (C) 0.12 mM, (D) 0.24 mM, and (E) 0.60 mM. The dominant peak in (C) and (D) corresponds to the PEGylated SNP product. In (E), the dominant peak corresponds to large particle aggregates while PEGylated SNP product is observed at ~ 9 min. In all cases, the asymmetric peak shape observed for the PEGylated SNP product is attributed to the presence of smaller, secondary particles. As a first approximation, this peak is fit using two Gaussian distributions, corresponding to the main (red) and secondary (blue) particle populations. The amount of secondary nucleation is estimated by comparing the peak areas calculated from the Gaussian fits. Ratios of secondary (blue) to main (red) particle peak areas are (C) 0.27, (D) 0.38, and (E) 1.32. Gaussian fits of the aggregate peak and any remaining free reactants are shown in purple and green, respectively. Insets in panels (C) to (E) show schematic illustrations of contributing particle sizes in native SNP solutions.

Due to the high cost of the Cy3 dye, the Cy3/APTES conjugate used in the synthesis of Cy3-labeled SNPs was typically prepared using a 10-fold excess of aminosilane to maximize the yield of silane-conjugated Cy3 dye. Importantly, this excess APTES is expected to be positively-charged under our basic pH reaction conditions. We hypothesize that the excess of aminosilane used in the preparation of the Cy3/APTES conjugate induces early aggregation of the negatively charged silica clusters (t = 1 in Figure 3.2B), resulting in the formation of larger Cy3-labled SNPs (t = 2 in Figure 3.2B), consistent with our observations. Comparison of the t = 1 and t = 2 time points in Figures 3.2A and B illustrates this concept. Furthermore, due to the relatively slow reaction rate of APTES, we expect that following core formation, unreacted APTES continues to induce aggregation of silica clusters to form dye-doped secondary particles during shell growth (t = 2 in Figure 3.2B).

Motivated by this hypothesis and by previous studies that describe the influence of amines on SNP morphology[31, 32, 33], we evaluated the size dispersity of a series of Cy3-loaded SNPs prepared by homogenous growth, using different ratios of Cy3 to APTES during dye conjugation. In these experiments, Cy3/APTES conjugates were prepared using constant Cy3 concentration (24.0 μM) and 5-fold (0.12 mM), 10-fold (0.24 mM), or 25-fold (0.6 mM) excess APTES.

Following PEGylation, the native SNP batches contain a mixture of particle aggregates, PEGylated SNP product, and unreacted chemicals (e.g. PEG or Cy3 dye)[14]. PEGylated SNPs were cleaned 3 times by centrifugation using a 30K MWCO membrane filter to remove unreacted chemicals. We then evaluated the size distributions of these Cy3-loaded SNPs using GPC[14]. Figures 3.2C to E show the corresponding GPC elugrams. The primary peak in Figures 3.2C (0.12 mM APTES) and D (0.24 APTES) corresponds to PEGylated SNP product. However, in SNPs prepared using 0.6 mM APTES (Figure 3.2E) the dominant GPC peak corresponds to

particle aggregates at short elution times around 8 min[14]. Aggregates are likely because the attachment of large numbers of positively-charged APTES molecules during particle growth decreases the stabilizing, electrostatic repulsion between negatively charged SNPs, resulting in increased particle aggregation at high APTES concentrations[31]. In this GPC elugram, the desired PEGylated SNP product is observed at ~ 10 min.

Comparison of Figures 3.2A to C shows that with increasing APTES concentration the PEGylated particle product peak shifts to shorter elution times, corresponding to increasing particle size. This trend is consistent with FCS results for SNPs synthesized using increasing concentrations of Cy3-silane (Figure 3.1B) and with our proposed formation mechanism (Figure 3.2B).

We also observed that increasing amounts of amine enhanced secondary nucleation during particle growth resulting in asymmetric GPC size distributions. In Figures 3.2C to E, peaks corresponding to PEGylated SNPs were consistently skewed toward long elution times due to the presence of smaller, secondary particles. Since a narrowly dispersed population of SNPs can be modeled using a single Gaussian distribution[14], we have approximated this asymmetric particle peak (Figures 3.2C to E) as a superposition of two Gaussian distributions (red and blue). The amount of secondary nucleation was estimated by comparing the peak areas from the Gaussian fits. As a metric, we have used the ratio, A, of the secondary particle peak area (blue) to the main particle product peak area (red). Increasing values of A are calculated as a function of increasing APTES, indicating an increase of secondary particle formation with APTES concentration. Calculated values of A for SNPs prepared using 0.12 mM, 0.24 mM and 0.60 mM APTES are 0.27, 0.38, and 1.32, respectively. Gaussian fits for aggregate peak and remaining free reactants peak shown in purple and green in Figures 3.2C to E, respectively, completed the analysis.

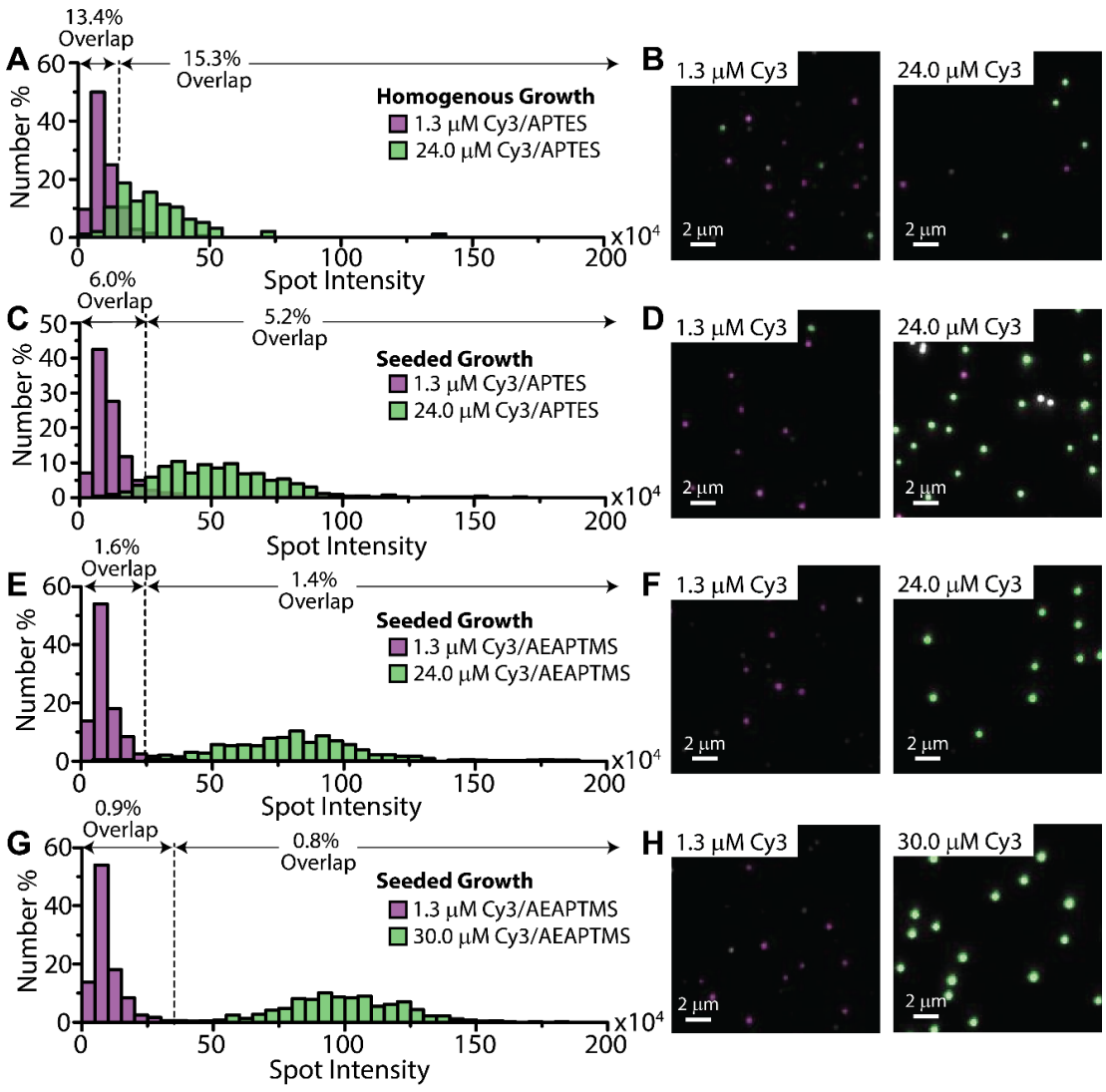

Figure 3.3. Comparison of high and low dye-loaded SNPs. (A) Single particle intensity distributions and (B) representative fluorescence images for SNPs prepared by (A, B) homogenous growth using 1.3 μM Cy3/APTES (purple in (A)) and 24.0 μM Cy3/APTES (green in (B)). (C, E, G) Single particle intensity distributions and (D, F, H) representative fluorescence images for SNPs prepared by seeded growth using 1.3 μM (purple in (C) through (G)) and either (C, D) 24.0 μM Cy3/APTES (green in (C)), (E, F) 24.0 μM Cy3/AEAPTMS (green in (E)), or (G, H) 30.0 μM Cy3/AEAPTMS (green in (G)). Overlap for high Cy3-loaded SNPs is defined as the fraction of particles with spot intensity below a threshold value (dashed black lines). Overlap for low Cy3-loaded SNPs is calculated as the fraction of particles with spot intensity above the same threshold value. In (B), (D), (F), and (H) spots above and below the corresponding thresholds in (A), (C), (E), and (G) are color-coded green and purple, respectively. (A and B are reproduced from ref. 19).

Due to the limits to quantitative analysis of sample heterogeneity using FCS[34, 35, 36], we have used total internal reflectance fluorescence (TIRF) microscopy to evaluate the effects of secondary nucleation on single-particle brightness of SNPs prepared by homogenous growth[13, 37]. Biotinylated SNPs were immobilized on streptavidin-coated glass substrates. We used a spot detection algorithm to identify individual particles in the resulting images. To calculate spot intensity, the background level and full width at half maximum, FWHM, in the x- and y-directions were derived from Gaussian fits. Spot intensity was defined as the background-corrected sum over all pixels within the FWHM[23].

We compared single particle intensity distributions from images of SNPs with low (1.3 μM Cy3) and high (24.0 μM Cy3) dye loadings, prepared by homogenous growth. Figures 3A and B show the resulting histograms and representative fluorescence images. As expected, we observe that spot intensity distributions shift to higher intensities as Cy3/APTES is increased from 1.3 μM to 24.0 μM. However, in this system, a nearly 20-fold increase in Cy3/APTES concentration translates to only a 2-fold increase in the peak position of the spot intensity distribution (Figure 3.3A). Additionally, significant overlap between the two distributions was observed. This result is attributed to the formation of secondary Cy3-labeled particles at high Cy3/APTES concentrations, which effectively decrease the overall concentration of Cy3 dyes relative to SNPs.

As a benchmark for intensity barcoding, we have quantified the overlap between the single particle intensity distributions shown in Figure 3.3A[7]. We defined a threshold between the two distributions (dashed line in Figure 3.3A) as the intensity value minimize overlap between high and low intensity particles. Overlap was then calculated as the percentage of high Cy3-loaded SNPs with intensities below the cutoff. Similarly, overlap for low Cy3-loaded SNPs was calculated as the percentage

of spots with intensities above the threshold value. As indicated in Figure 3.3A, calculated overlaps for low (1.3 μM Cy3) and high (24.0 μM Cy3) Cy3-loaded SNPs were 13.4% and 15.3%, respectively.

To illustrate the effects of overlapping intensity distributions in barcoding applications, we have false-colored the images in Figure 3.3B according to the threshold defined in Figure 3.3A, so that spots with intensities below and above the threshold are purple and green, respectively. Figure 3.3A shows that on a single particle level, nearly 30% of SNPs cannot be identified based on intensity alone. As expected, both green and purple spots are observed in images (Figure 3.3B) that contain only high or only low Cy3-loaded SNPs, demonstrating that these SNPs cannot be unambiguously identified if mixed.

3.3.2 Fluorescent SNPs prepared by seeded growth.

We circumvented the size dispersity associated with use of high Cy3-silane concentrations in the homogenous growth approach by introducing the second "seeded growth" approach. Using this method, the Cy3/APTES conjugate was introduced during the continued growth of narrowly dispersed, undyed seed particles (< 20 nm) using TEOS. The Cy3/APTES conjugate was again prepared by reacting Cy3 NHS ester with a 10-fold excess of APTES. To maintain relatively small particle sizes, only two doses of TEOS (64.3 mM TEOS each) were added in a thin layer to the top surface of the reaction.

Since the feed rate of TEOS into the reaction is determined by the interfacial area between the aqueous reaction volume and a thin layer of TEOS added to its surface[24], optimized protocols for shell growth were developed by varying the concentration of seed particles. In this system, increasing seed particle concentration (compare Figures 3.4A and 3.2B) is expected to increase the rate of TEOS

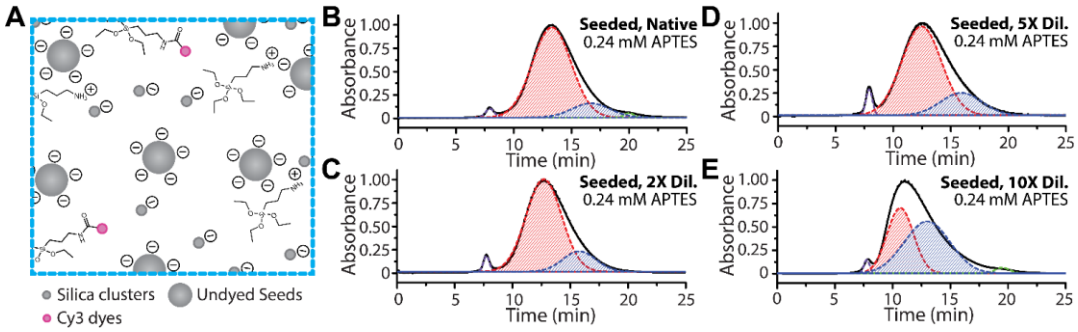

Figure 3.4. Optimization of seeded growth conditions. (A) Schematic illustration of the formation of SNPs synthesized by seeded growth in the presence of the Cy3/APTES conjugate (compounds not to scale). A continuous feed of TEOS into solution facilitates growth of undyed seed particles by addition of negatively-charged silica clusters (< 2 nm). Since the feed rate is determined by the interfacial area between the aqueous reaction volume and a thin layer of TEOS added to the top of the reaction, increasing seed particle concentrations (as compared to Figure 2B) progressively increase the rate of TEOS consumption by existing particles thereby lowering the probability of secondary particle formation. At the same time, the attractive electrostatic interactions between the excess of positively-charged aminosilane used in the preparation of the Cy3/APTES conjugate and negatively-charged seed particles decrease the effective aminosilane concentration in solution also reducing secondary nucleation. (B) to (E) GPC elugrams of SNPs following the growth of two silica shells (64.3 mM TEOS per shell). Core/shell SNPs are prepared using (B) native concentration, (C) 2-fold, (D) 5-fold, and (E) 10-fold diluted cores. The dominant peak in each GPC elugram (black) corresponds to PEGylated SNP product. The asymmetric peak shape is attributed to the presence of smaller, secondary particles. As a first approximation, peak fits used two Gaussian distributions, corresponding to main (red) and secondary (blue) particle populations. The amount of secondary nucleation was estimated by comparing peak areas calculated from Gaussian fits. Calculated ratios of secondary (blue) to main (red) particle peak areas are (A) 0.15, (B) 0.20, (C) 0.26, and (D) 1.37. Gaussian fits of aggregate (purple) and remaining free reactants (green) peaks completed the analysis.

consumption by existing particles thereby lowering the probability of secondary particle formation. At the same time, the attractive electrostatic interactions between the negatively-charged seed particles and the excess of positively-charged aminosilane used in the preparation of the Cy3/APTES conjugate may decrease the effective concentration of aminosilanes in solution also reducing secondary nucleation of particles (Figure 3.4A).

Figures 3.4B to E show GPC elugrams of SNPs prepared using varying seed concentrations, following the addition of 24.0 μM Cy3/APTES, prepared using a 10-fold excess of APTES, and two silica shells (64.3 mM TEOS per shell; i.e keeping the amount of added TEOS constant). SNPs were again PEGylated and cleaned by spin filtration prior to GPC. Seed concentrations are reported relative to the native reaction concentration (e.g. 5-fold dilution). We observed decreasing elution times corresponding to increasing particle product sizes for lower core concentrations (Figure 3.4B to E). Furthermore, SNPs synthesized using progressively dilute seed concentrations exhibited increasingly skewed particle peaks, indicating that rates of secondary nucleation were increased. The PEGylated particle peaks in Figures 3.4B to E were again approximated as a superposition of two Gaussian distributions (red and blue). Calculated values of *A* for SNPs prepared using the native core concentration, or 2-fold, 5-fold, and 10-fold diluted cores are 0.15, 0.20, 0.26, and 1.37, respectively. Comparison to SNPs prepared by homogenous growth using 24.0 μM Cy3 and a 10-fold excess of APTES ($A = 0.38$), shows that preparation of SNPs by seeded growth of native, 2-fold, or 5-diluted cores decreases the rate of secondary nucleation.

Due to the prohibitive cost of using high concentrations of Cy3 dye, we did not initially increase the concentration of Cy3/APTES beyond the maximum of 24.0 μM used in the homogenous growth series described in Figure 3.3A. At constant Cy3/APTES, the effective ratio of Cy3 to SNPs is determined by both the initial seed

concentration and rate of secondary nucleation. SNPs prepared by either seeded growth of 2-fold diluted cores or by homogenous growth using identical concentrations of Cy3/APTES (24.0 μM) show similar single particle intensity distributions (Figures S2A and B). This result demonstrates that although the rate of secondary particle formation is lowered by using the seeded growth approach (compare Figures 3.4C and 3.3D), the effective ratio of Cy3 to SNPs is not improved. However, SNPs prepared by lowering the initial concentration of seeds 5-fold exhibit substantially improved single particle intensity distributions. We have therefore worked with 5-fold diluted seeds in all further experiments using this approach.

TEM images of SNPs prepared using the optimized seeded growth approach (i.e. 5-fold diluted cores) taken prior to PEGylation and subsequent purification (Figure S3A) show that Cy3-loaded SNPs synthesized using this method and 24.0 μM Cy3-silane from APTES are < 40 nm and narrowly dispersed. Figure 3.5B shows the intensity-matched absorption and corresponding emission spectra of free Cy3 dye (black) and SNPs synthesized using 24.0 μM Cy3-silane (green). A quantum enhancement of only 4.9 is observed upon encapsulation. Comparison to SNPs prepared by homogenous nucleation (Figure 3.1A), where a 7-fold enhancement is measured, suggests that Cy3 dyes may be only partially encapsulated[14, 18]. However, spot intensity distributions for SNPs synthesized by seeded growth are still shifted to higher intensities (Figure 3.3C) as compared to SNPs prepared by homogenous growth (Figure 3.3A) using the same 24.0 μM concentration of Cy3/APTES. In Figure 3.3C, we have compared this brighter SNP to low intensity SNPs synthesized using the same approach (seeded growth, 1.3 μM Cy3/APTES). Using the intensity threshold defined in Figure 3.3C, we observe that the percentage of high dye-loaded SNPs with intensities below the threshold decreases from 13.4% to 6.0%, corresponding to improved identification accuracy. Similarly, the percentage of low dye-loaded SNPs

with intensities above the threshold decreases from 15.3% to 5.2%. Comparison of the color-coded images of high dye-loaded SNPs in Figures 3.3B and D illustrates that low-intensity spots (purple) are less frequently observed in images of high dye-loaded SNPs synthesized by seeded growth.

Due to the relatively slow reaction kinetics of APTES[29], we hypothesized that the efficiency of Cy3 incorporation into SNPs could be improved by introducing a faster reacting organosilane linker. We therefore prepared fluorescent SNPs by seeded growth and used 3-aminopropyl trimethoxysilane (APTMS, Figure 3.5A) as a silane linker[29]. Cy3-silane was prepared by reacting Cy3 NHS ester with a 10-fold excess of APTMS (Cy3/APTMS). Figure 3.5B shows the intensity-matched absorbance and corresponding emission spectra for SNPs prepared using 24.0 μM Cy3/APTMS (purple). Quantum enhancements are increased to about 6.4 as compared to 4.9 for SNPs prepared using Cy3/APTES at the same concentration (green in Figure 3.5B), suggesting that dyes are more completely encapsulated[18].

However, comparison of PEGylated particle peaks in GPC indicates that in seeded growth syntheses, use of Cy3/APTMS (Figure S3D) rather than Cy3/APTES (Figures 3.4D and S3B) increases the rate of secondary nucleation. Calculated values of *A* are 0.37 and 0.26 for Cy3/APTMS and Cy3/APTES, respectively. We also observe that the particle peak position shifts to smaller particle sizes. This effect is similar to that observed for the core concentration series shown in Figure 3.4, where secondary nucleation increases the particle concentration and due to the unchanged feed rate of TEOS into the reaction, decreases the average size of the final particles. Figures S3A and S3B show TEM images that corroborate the effects of organosilane linker chemistry on size dispersity.

Spot intensity distributions for SNPs prepared using Cy3/APTMS (Figure 3.5D) were shifted to higher intensities as compared to SNPs prepared using

Cy3/APTES (Figure 3.5C). However, low intensity spots were still frequently observed, which are attributed to the formation of secondary particles (Figure 3.5D). These secondary particles are expected to contain relatively low numbers of dyes because they are formed late in the synthesis.

To overcome this problem, we finally introduced N-(2-aminoethyl)-3-aminopropyl trimethoxysilane (AEAPTMS, Figure 3.5A) as a third fast-reacting organosilane linker[29]. We expect that the secondary amines may support association with SNPs by hydrogen bonding to surface silanol groups[33], increasing the incorporation efficiency of Cy3/AEAPTMS relative to Cy3/APTES or Cy3/APTMS. Such an association would also act to decrease the concentration of free aminosilane in solution, decreasing the relative rates of secondary particle formation. Cy3-silane was prepared by reacting Cy3 NHS ester with a 10-fold excess of AEAPTMS (Cy3/AEAPTMS). Figure 3.5B shows the intensity-matched absorbance and corresponding emission spectra for SNPs prepared by seeded growth using 24.0 μM Cy3/AEAPTMS (blue). Similar to SNPs prepared using Cy3/APTMS at the same concentration (purple), quantum enhancements of 6.5 are achieved.

Concomitantly, we observed decreased rates of secondary particle formation in syntheses using Cy3/AEAPTMS (A = 0.29) as compared to Cy3/APTMS (A = 0.37) (Figure S3E and S3F). Figure S3F demonstrates that SNPs prepared using Cy3/AEAPTMS exhibit relatively narrow and symmetric particle peaks in GPC. The TEM image shown in Figure S3E confirms that SNPs prepared using AEAPTMS are narrowly dispersed.

Spot intensity distributions for SNPs prepared using 24.0 μM Cy3/AEAPTMS (Figure 3.5E) were shifted to slightly higher intensities as compared to SNPs prepared using Cy3/APTMS (Figure 3.5D). Importantly, due to decreased rates of secondary particle formation, we observed relatively few low intensity spots (Figure 3.5E). In

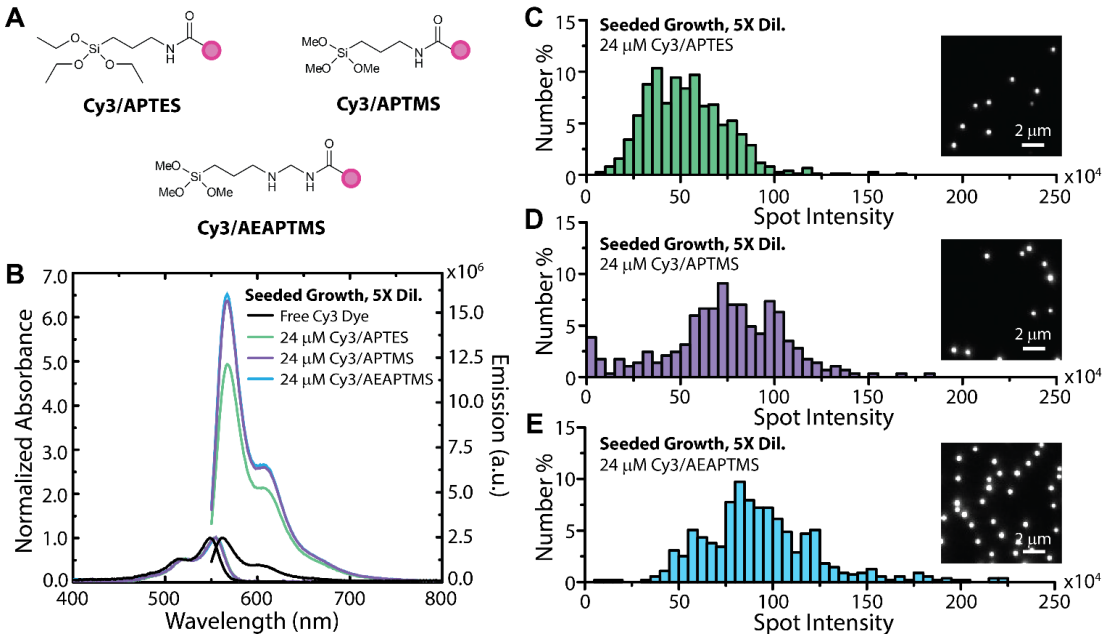

Figure 3.5. Seeded growth of SNPs using different organosilane linkers. (A) Chemical structures of Cy3-silane conjugates prepared using APTES, APTMS, and AEAPTMS. (B) Absorbance and emission spectra for free Cy3 dye and SNPs prepared by seeded growth using 24.0 μM Cy3/APTES, 24.0 μM Cy3/APTMS, and 24.0 μM Cy3/AEAPTMS. All dye conjugates in this series were prepared using a 10-fold excess of aminosilane. (C) to (E) Single particle intensity distributions corresponding to SNPs prepared by seeded growth using (C) 24.0 μM Cy3/APTES, (D) 24.0 μM Cy3/APTMS, and (E) 24.0 μM Cy3/AEAPTMS. Insets in panels (C) to (D) show representative fluorescence images.

Figure 3.3E, we have compared SNPs prepared by seeded growth using 1.3 μM and 24.0 μM Cy3/AEAPTMS. Comparison between Figures 3.3C and E shows that by using Cy3/AEAPTMS rather than Cy3/APTES, the percentage of high dye-loaded SNPs with intensities below the threshold decreases from 6.0% to 1.6%. Similarly, the percentage of low dye-loaded SNPs with intensities above the threshold decreases from 5.2% to 1.4%. Comparison of the color-coded images in Figures 3.3D and F demonstrates further improved identification accuracy.

Finally, we prepared an optimized set of SNPs with well-separated intensity distributions, using 1.3 μM and 30.0 μM Cy3/AEAPTMS in a seeded growth. Figure 3G shows the resulting spot intensity distributions. Using the intensity threshold defined in Figure 3.3G (dashed black lines), we observe minimal overlap (< 1%) between spot intensity distributions of high (green) and low (purple) dye-loaded SNPs. Figure 3.3H shows color-coded fluorescence images, in which spots with high and low intensities are again colored green and purple, respectively. These images illustrate that SNPs prepared using optimized synthesis conditions (i.e. by seeded growth and using Cy3/AEAPTMS) are unambiguously identifiable based on intensity alone.

Conclusions

In this article, we have introduced two methods for preparing highly dye-loaded SNPs with increasing average intensity levels. By comparing these approaches, we have identified critical parameters for the synthesis of high and low dye-loaded SNPs with well-separated single particle intensity distributions in batch reactions. Distributions of dyes within single particles are also well-controlled by silica shell growth, minimizing self-quenching and maximizing fluorescence enhancements gained from encapsulation within the rigid silica matrix. Optimized SNPs are highly

fluorescent and are unambiguously distinguishable on a single particle level based on fluorescence intensity alone.

We have observed in SNPs prepared by homogenous nucleation, that increased rates of secondary particle formation are caused by the excess of aminosilane commonly used to synthesize dye-silane conjugates (i.e. APTES), resulting in increased particle size dispersity. Importantly, secondary particles formed in the presence of dye-silane conjugates have comparatively low fluorescence intensity, because they are formed later in the growth process. Simply increasing the concentration of dye-silane conjugate used in homogenous nucleation-based approaches thus generates heterogenous samples with low overall brightness. In this study, we demonstrate that secondary nucleation is minimized by using a seeded growth approach, even in the presence of high concentrations of aminosilanes. Employing this approach, we demonstrate that reduced initial seed concentrations may be used to mitigate the cost of the fluorescent dyes. We have also shown that dye incorporation efficiency depends on the organosilane linker[29], demonstrating that maximum dye-loading efficiency is achieved using Cy3/AEAPTMS. Lowered incorporation efficiencies were observed for Cy3/APTES due to slow reaction kinetics. Conversely, use of fast-reacting Cy3/APTMS caused increased secondary particle formation and correspondingly wide single particle intensity distributions. We hypothesize that for AEAPTMS, fast reaction kinetics in addition to hydrogen bonding between secondary amines on the AEAPTMS and surface silanol groups on the SNPs play significant roles in improving incorporation efficiency[32].

Since optimized intensity distributions were achieved by tuning the silica chemistry only, we expect that our results can be generalized to a range of spectrally distinct dyes. Combinatorial labeling approaches could then be used to generate a silica nanoparticle platform for highly multiplexed single particle imaging

applications. The SNPs described in this study are small (< 40 nm) and readily surface functionalizable with a variety of targeting moieties, making them ideal fluorescent tags for imaging in living biological systems[7]. Additionally, the synthetic parameters identified here may also be relevant in the design of alternate approaches for batch synthesis of intensity-based nanoparticle barcodes for single particle imaging applications.

3.5 Acknowledgements

Research reported in this publication was supported by the National Cancer Institute of the National Institutes of Health under Award Number U54CA199081. T.A. acknowledges financial support by the Ghent University Special Research Fund (BOF14/PDO/007) and the European Union's Horizon 2020 research and innovation program (MSCA-IF-2015-702300). This work made use of CCMR Shared Facilities, which are supported through the NSF MRSEC program (DMR-1120296). This work made use of the Nanobiotechnology Center shared facilities at Cornell. Imaging data was acquired through the Cornell University Biotechnology Resource Center, with NSF funding (1428922) for the Zeiss Elyra Microscope.

REFERENCES

1. Lichtman, J. W.; Conchello, J. Fluorescence microscopy. *Nat. Meth.* **2005**, *2*, 910 – 919.

2. Lubeck, E.; Cai, L. Single-cell systems biology by super-resolution imaging and combinatorial labeling. *Nat. Methods.* **2012**, *9*, 743 – 748.

3. Joo, C.; Balci, H.; Ishitsuka, Y.; Buranachai, C.; Ha, T. Advances in Single-Molecule Fluorescence Methods for Molecular Biology. *Annu. Rev. Biochem.* **2008,** *77*, 51 – 77.

4. Tsien, R. Y. The Green Fluorescent Protein. *Annu. Rev. Biochem.* **1998**, *67*, 509 – 544.

5. Ow, H.; Larson, D.; Srivastava, M.; Baird, B., Webb, W.; Wiesner U. Bright and Stable Core−Shell Fluorescent Silica Nanoparticles. *Nano Lett.* **2005**, *5*, 113 - 117.

6. Medintz, I. L.; Uyeda, H. T.; Goldman, E. R.; Mattoussi, H. Quantum dot bioconjugates for imaging, labelling and sensing. *Nat. Mater.* **2005**, *4*, 435 – 446.

7. Woehrstein, J. B.; Strauss, M. T.; Ong, L. L.; Wei, B.; Zhang, D. Y.; Jungmann R.; Yin P. Sub-100 nm metafluorophores with digitally tunable optical properties self-assembled from DNA. *Sci. Adv.* **2017**, *3*, 1602128.

8. Han, M.; Gao, X.; Su, J. Z.; Nie, S. Quantum-dot-tagged microbeads for multiplexed optical coding of biomolecules. *Nat. Biotechnol.* **2001**, *19*, 631 – 635.

9. Zhang, Y. Z.; Kemper, C. R.; Haugland, R.P. Microspheres with fluorescent spherical zones. US 5,786,219 (1998).

10. Banerjee, S.; Georgescu, C.; Daniels, E. S.; Dimonie, V. L., Seul, M. Production of dyed polymer microparticles. US 6,964,747 (2005).

11. Um, S. H.; Lee, J. B.; Kwon, S. Y.; Li, Y.; Luo D. Dendrimer-like DNA-based fluorescence nanobarcodes. *Nat. Protoc.* **2006**, *1*, 995 – 1000.

12. Wang, L.; Tan, W. Multicolor FRET Silica Nanoparticles by Single Wavelength Excitation. *Nano Lett.* **2006**, *6*, 84 – 88.

13. Wu, C.; Hansen, S. J.; Hou, Q.; Yu, J.; Zeigler, M.; Jin, Y.; Burnham, D. R.; McNeill, J. D.; Olson, J. M.; Chiu, D. T. Bioconjugation of Ultrabright Semiconducting Polymer Dots for Specific Cellular Targeting. *Angew. Chem. Int. Ed.* **2011**, *50*, 3430 – 3434.

14. Ma, K.; Mendoza, C.; Werner-Zwanziger, U.; Zwanziger, J.; Wiesner, U. Control of Ultrasmall Sub-10 nm Ligand-Functionalized Fluorescent Core−Shell Silica Nanoparticle Growth in Water. *Chem. Mater.* **2015**, *27*, 4119 – 4133.

15. Ma, K.; Zhang, D.; Cong, Y.; Wiesner, U. Elucidating the Mechanism of Silica Nanoparticle PEGylation Processes Using Fluorescence Correlation Spectroscopies. *Chem. Mater.* **2016**, *28*, 1537 – 1545.

16. Ma, K.; Wiesner, U. Modular and Orthogonal Post-PEGylation Surface Modifications by Insertion Enabling Penta-Functional Ultrasmall Organic-Silica Hybrid Nanoparticles. *Chem. Mater.* **2017**, *29*, 6840 – 6855.

17. Phillips, E.; Penate-Medina, O.; Zanzonico, P. B.; Carvajal, R. D.; Mohan, P.; Ye, Y.; Humm, J.; Gonen, M.; Kalaigian, H., Schoder, H.; Strauss, H. W.; Larson, S. M.; Wiesner, U.; Bradbury, M. S. Clinical translation of an ultrasmall inorganic optical-PET imaging nanoparticle probe. *Sci. Trans. Med.* **2014**, *6*, 260.

18. Larson, D. R.; Ow, H.; Vishwasrao, H. D.; Heikal, A. A.; Wiesner, U.; Webb, W. W. Silica Nanoparticle Architecture Determines Radiative Properties of Encapsulated Fluorophores. *Chem. Mater.* **2008**, *20*, 2677 – 2684.

19. Kao, T.; Kohle, F.; Ma, K.; Aubert, T.; Andrievsky, A.; Wiesner U. Fluorescent Silica Nanoparticles with Well Separated Intensity Distributions from Batch Reactions. *Nano Lett.* **2017**, submitted.

20. Ngundi, M. M.; Shriver-Lake, L. C.; Moore, M. H.; Lassman, M. E.; Ligler, F. S.; Taitt, C. R. Array Biosensor for Detection of Ochratoxin A in Cereals and Beverages. *Anal. Chem.* **2005**, *77*, 148 – 154.

21. Ruiz, A. E.; Caregnato, P.; Arce, V. B.; Schiavoni, M. M.; Mora, V. C.; Gonzalez, M. C.; Allegretti, P. E.; Martire, D. O. Synthesis and Characterization of Butoxylated Silica Nanoparticles. Reaction with Benzophenone Triplet States. *J. Phys. Chem. C.* **2007**, *111*, 7623 – 7628.

22. Magde, D.; Elson, E.; Webb, W. W. Thermodynamic fluctuations in a reacting system-measurement by fluorescence correlation spectroscopy. *Phys. Rev. Lett.* **1972**, *29*, 705.

23. Willing, K. I.; Rizzoli, S. O.; Westphal, V.; Jahn, R.; Hell, S.W. STED microscopy reveals that synaptotagmin remains clustered after synaptic vesicle exocytosis. *Nature*. **2006**, *440*, 935 – 939.

24. Yokoi, T.; Sakamoto, Y.; Terasaki, O.; Kubota, Y.; Okubo, T.; Tatsumi, T. Periodic Arrangement of Silica Nanospheres Assisted by Amino Acids. *J. Am. Chem. Soc.* **2006**, *128*, 13644 – 13665.

25. Hartlen, K. D.; Athanasopoulos, A. P. T.; Kitaev, V. Facile Preparation of Highly Monodisperse Small Silica Spheres (15 to >200 nm) Suitable for Colloidal Templating and Formation of Ordered Arrays. *Langmuir*. **2008**, *24*, 1714-1720.

26. Schubbe, S.; Cavelius, C.; Schumann, C.; Koch, M.; Kraegeloh, A. STED Microscopy to Monitor Agglomeration of Silica Particles Inside A549 Cells. *Adv. Eng. Mater.* **2010**, *12*, 417 – 422.

27. Muddana, H. S.; Morgan, T. T.; Adair, J. H.; Butler, P. J. Photophysics of Cy3-Encapsulated Calcium Phosphate Nanoparticles. *Nano Lett.* **2009**, *9*, 1559 – 1566.

28. Cohen, B.; Martin, C.; Iyer, S. K.; Wiesner, U.; Douhal, A. Single Dye Molecule Behavior in Fluorescent Core-Shell Silica Nanoparticles. *Chem. Mater.* **2012**, *9*, 361 – 372.

29. Wang, J.; Sugawara-Narutaki, A.; Fukao, M.; Yokoi, T.; Shimojima, A.; Okubo, T. Two-Phase Synthesis of Monodisperse Silica Nanospheres with Amines or Ammonia Catalyst and Their Controlled Self-Assembly. *ACS Appl. Mater. Interfaces*, **2011**, *3*, 1538 – 1544.

30. Carcouët, C. C. M. C.; van de Put, M. W. P.; Mezari, B.; Magusin, P. C. M. M.; Laven, J.; Bomans, P. H. H.; Friedrich, H.; Catarina, A.; Esteves, C.; Sommerdijk, N. A. J. M.; van Benthem, R. A. T. M.; de With, G. Nucleation and Growth of Monodisperse Silica Nanoparticles. *Nano Lett.* **2014**, *14*, 1433 – 1438.

31. Mizutani, T.; Nagase, H.; Fujiwara, N.; Ogoshi, H. Silicic Acid Polymerization Catalyzed by Amines and Polyamines. *Bull. Chem. Soc. Jpn.* **1998**, *71*, 2017 – 2022.

32. Chen, C; Hayakawa, C; Shirosaki, Y.; Fujii, E.; Kawabata, K; Tsuru, K; Osaka, A. Sol–Gel Synthesis and Microstructure Analysis of Amino-Modified Hybrid Silica Nanoparticles from Aminopropyltriethoxysilane and Tetraethoxysilane. *J. Am. Ceram. Soc.* **2009**, *92*, 2074 – 2082.

33. Kroger, N.; Deutzmann, R.; Bergsdorf, C.; Sumper, M. Species-specific polyamines from diatoms control silica morphology. *Proc. Natl. Acad. Sci.* **2000**, *97*, 14133 – 14138.

34. Meseth, U.; Wohland, T.; Rigler, R.; Vogel, H. Resolution of Fluorescence Correlation Measurements. *Biophys. J.* **1999**, *76*, 1619–1631.

35. Doose, S.; Tsay, J.; M. Pinaud, F.; Weiss, S. Comparison of Photophysical and Colloidal Properties of Biocompatible Semiconductor Nanocrystals Using Fluorescence Correlation Spectroscopy. *Anal. Chem.* **2005**, *77*, 2235 – 2242.

36. Bacia, K.; Schwille, P. Practical guidelines for dual-color fluorescence cross-correlation spectroscopy. *Nat. Protoc.* **2007**, *11*, 2842-2856.

37. Small, A.; Stahlheber, S. Fluorophore localization algorithms for super-resolution microscopy. *Nat. Methods*. **2014**, *11*, 267 – 279.

CHAPTER 4

FORMATION PATHWAYS OF MESOPOROUS SILICA NANPARTICLES WITH DODECAGONAL TILING[*]

Abstract

Considerable progress in the fabrication of quasicrystals demonstrates that they can be realized in a broad range of materials. However, the development of chemistries enabling direct experimental observation of early quasicrystal growth pathways remains challenging. Here we report the synthesis of four surfactant directed mesoporous silica nanoparticle (MSN) structures, including dodecagonal quasicrystalline nanoparticles, as a function of micelle pore expander concentration or stirring rate. We demonstrate that the early formation stages of dodecagonal quasicrystalline MSNs can be preserved, where precise control of MSN size down to < 30 nm facilitates comparison between MSNs and simulated single particle growth trajectories beginning with a single tiling unit. Our results reveal details of the building block size distributions during early growth and how they promote quasicrystal formation. This work identifies simple synthetic parameters such as stirring rate, that may be exploited to design other quasicrystal-forming self-assembly chemistries and processes.

---

[*] Originally Published as: Yao Sun[§], Kai Ma[§], Teresa Kao[§], Katherine A. Spoth, Hiroaki Sai, Duhan Zhang, Lena F. Kourkoutis, Veit Elser, Ulrich Wiesner. Formation Pathways of Mesoporous Silica Nanoparticles with Dodecagonal Tiling. *Nature Communications*, 8, 252.

[§] Yao Sun, Kai Ma, and Teresa Kao contributed equally to this work.

Introduction

Quasicrystals exhibit highly ordered local structure but lack long range translational periodicity, and permit symmetry operations that are forbidden in classical crystallography. Since the discovery of quasicrystalline order in metal alloys[1], quasicrystals have been observed in a wide variety of materials, including thin films[2], liquid crystals[3], polymers[4], colloids[5] and mesoporous networks[6], demonstrating that quasicrystallinity can be considered a universal form of ordering.

Advances in the identification of quasicrystalline materials have attracted widespread attention to the underlying mechanisms that govern quasicrystal formation. In self-assembled micellar systems, access to quasicrystal and quasicrystal approximant phases depends on building block geometry, controlled in recent experimental studies through molecular design of giant surfactant molecules[7, 8] and asymmetric diblock copolymers [9, 10]. These experimental findings are consistent with simulations of self-assembled systems, where building blocks designed with substantial shape polydispersity or patchy surfaces promote quasicrystalline order[11, 12]. In metal alloys, studies of quasicrystal formation have verified theoretical predictions that quasicrystalline order is maintained during grain growth by a local error-and-repair type mechanism[13, 14]. Despite these successes, experimental investigations of early quasicrystal formation mechanisms remain challenging, largely due to a lack of chemistries that facilitate direct observation.

Mesoporous silica materials with pore sizes in the range between 2 – 50 nm have attracted widespread attention due to their precisely tunable macroscopic form, chemical functionality, and mesopore structure[15, 16]. There have been reports of mesoporous silica bulk materials[15, 16, 17, 18] and nanoparticles[19, 20, 21] with a variety of pore structures, including hexagonal[16], cubic[20], and quasicrystalline structures[6, 20, 22]. The formation of mesoporous silica is a result of silica condensation directed by

molecular templates, such as surfactants or polymers[16, 23]. This cooperative assembly process is driven by non-directional interactions between micelles and silica precursors, making mesoporous silica similar to systems of metal alloys, where non-directional bonding plays a key role in achieving the non-periodic bonding geometries required for quasicrystal formation.

Inspired by this analogy, we have synthesized surfactant directed mesoporous silica nanoparticles (MSNs) with dodecagonal tiling and used them as a test bed for studying early formation mechanisms. While previous reports of quasicrystalline mesoporous silicas have used anionic surfactants[6, 22], we demonstrate that such materials can also be synthesized by self-assembly of positively charged surfactant micelles. The dodecagonal quasicrystal structure is the last in a sequence of four different structures discovered in this study as a function of either micelle pore expander concentration or reaction stirring rate. Via direct visualization employing cryo-transmission electron microscopy (cryo-TEM) and quantitative image analysis, we find that quasicrystallinity is predominantly governed by asymmetries in the micelle size distribution and identify micelle pore expander concentration and reaction stirring rate as equivalent experimental control parameters. Furthermore, precise control of the silica chemistry enables MSN sizes to be tuned from above 100 nm, where dodecagonal tiling patterns are well developed, to below 30 nm, where particles consisting of only a single triangle or square tiling unit represent the earliest formation stages of the dodecagonal tiling. Experimental results are then compared to growth simulations. Our results suggest that the incorporation of building blocks with asymmetric size distributions at early times in the growth process promotes quasicrystal formation and that simple synthesis parameters like stirring rate can be used for their control.

Experimental

Materials

Hexadecyltrimethylammonium bromide (CTAB, ≥99%), ethyl acetate (EtOAc, ACS grade), ammonium hydroxide (NH_4OH, 29%), 1,3,5-trimethylbenzene (TMB, 99%), *N*-(2-aminoethyl)-3-aminopropyltrimethoxysilane (AEAPTMS, 95%), (3-aminopropyl)trimethoxysilane (APTMS, 95%), tetraethyl orthosilicate (TEOS, ≥99%), tetramethyl orthosilicate (TMOS, ≥99%), hydrochloric acid (HCl, 36.5-38%), acetic acid (glacial), and ethanol (absolute, anhydrous) were used as received without further purification. Deionized water (Milli-Q, 18.2 MΩ·cm) was used throughout.

Synthesis of TEOS/AEAPTMS derived MSNs

TEOS/AEAPTMS derived MSNs with different structures were synthesized in aqueous solution at room temperature through surfactant directed silica condensation. Round bottom flasks and egg-shaped stir bars were used in all TEOS/AEAPTMS syntheses. MSNs were prepared with [TMB] ranging from 12mM to 205mM. EtOAc (0.44mL), NH_4OH (1.35 mL), and then TMB were added to an aqueous solution of CTAB (52.5mL, 2.61 mM) stirred at 650 rpm. After 30 minutes, a mixture of TEOS (0.25mL) and AEAPTMS (0.0375 mL) was added to the reaction under continued stirring and allowed to react for 5 minutes. Then, additional water (18.45 mL) was added and the reaction was left stirring for 24 hours. On completion of the reaction, the particle suspension was neutralized with 2M HCl, before cleaning by repeated centrifugation and redispersion in EtOH. CTAB was removed from the resulting particles by adding 5 vol% of acetic acid to the suspension and stirring for 30 minutes. Following CTAB removal, the particles were again cleaned by repeated centrifugation and redispersion in EtOH.

In order to study the effect of stirring rate on the structure of these particles, MSNs were synthesized using constant [TMB] (29 mM) and four different stirring rates: 500 rpm, 650 rpm, 800 rpm, and 1000 rpm. All other synthesis parameters were unchanged from the above description.

Synthesis of TMOS/APTMS derived MSNs

TMOS/APTMS derived MSNs of different sizes and structures were synthesized by surfactant directed silica condensation in room temperature, aqueous solution. Round bottom flasks and egg-shaped stir bars were used in all TMOS/APTMS syntheses. MSNs were prepared with [TMB] ranging from 4mM to 116mM and [NH_4OH] ranging from 15mM to 150mM. High [TMB] resulted in more quasicrystalline particles and high [NH_4OH] resulted in larger particle sizes. NH_4OH and TMB were added to an aqueous solution of CTAB (10 mL, 22.78 mM) stirred at 600 rpm. After two hours, a mixture of TMOS (34 µL) and APTMS (25 µL) was added to the reaction and allowed to react for 24 hours under continued stirring. Applied synthesis conditions gave access to particle sizes between about 30 and 150 nm. On completion of the reaction, the particle suspension was cleaned by repeated centrifugation and redispersion in EtOH. CTAB was removed from the resulting particles by adding 5 vol% of acetic acid to the suspension and stirring for 30 minutes. Following CTAB removal, the particles were again cleaned by repeated centrifugation and redispersion in EtOH. For the APTMS study (Fig. C.4), the [NH_4OH] was held constant at 120 mM and the APTMS concentration was varied from 0 to 14 mM. All other parameters were kept the same.

Characterization

Transmission electron microscopy (TEM) images were taken using a FEI Tecnai T12 Spirit microscope operated at an acceleration voltage of 120 kV. Fast Fourier transform (FFT) analysis was performed using ImageJ software. Each TEM sample was prepared after CTAB removal by evaporating 10 μL of suspension on TEM grid in dry air. Cryo-TEM images were collected under low-dose conditions using a customized FEI Titan Themis 300 operating at 300 kV equipped with a cryo-box and FEI Ceta 16M camera. More details can be found in the Supplementary Methods.

SAXS patterns were obtained at the G1 station at the Cornell High Energy Synchrotron Source (CHESS) using a 10 keV beam and a sample-to-detector distance of 40 cm. All samples were powders prepared by vacuum drying MSN suspensions after CTAB removal and were imaged soon after drying.

Nitrogen sorption measurements were performed using a Micromeritics ASAP2020 instrument. For each measurement, approximately 10 mg of freshly vacuum-dried powder sample was degassed at room temperature under vacuum overnight prior to the analysis.

Tiling analysis

Tilings were obtained from TEM images using a home-built MATLAB program, where a 10% tolerance of edge orientation and edge length were allowed and underdeveloped pores on MSNs were not counted. MSNs were excluded from analysis only if particle orientation prevented visualization of the pore structure from TEM images. No additional selection criteria were applied. These tilings were further analyzed using home-built programs to calculate radius of gyration in both parallel and perpendicular spaces. Detailed methods are provided in the Supplementary Methods.

Simulations

An irreversible triangle-square tiling model was developed so that particle growth trajectories could be studied. Simulations were performed employing a self-written MATLAB program. See descriptions in the main text as well as more details in the Supplementary Methods.

Results

[TMB] induced transitions between four MSN structures

MSNs were synthesized by co-condensing a mixture of silane precursors, tetraethyl orthosilicate (TEOS) and N-(2-aminoethyl)-3-aminopropyltrimethoxysilane (AEAPTMS), in the presence of hexadecyltrimethylammonium bromide (CTAB) surfactant micelles (see molecular structures in Fig. 4.1a). The aminosilane was added to tailor the packing behavior of the CTAB surfactant molecules[24, 25], enabling access to more complex silica nanostructures[19, 20, 26]. The CTAB micelle size and size distribution was systematically varied by adjusting the concentration of a micelle pore expander, mesitylene (TMB) (*27*, *28*, *29*). Transmission electron microscopy (TEM) images show that as the concentration of TMB, [TMB], was increased, the MSN structure changed from hexagonal (Fig. 4.1b) to multicompartment (Fig. 4.1c and Fig. C.1) to cubic (Fig. 4.1d) and finally to a structure with dodecagonal symmetry (Fig. 4.1e).

Small-angle x-ray scattering (SAXS) measurements, which average over macroscopic volumes, were performed on the TEOS/AEAPTMS particles (Fig. C.2). The results corroborate the structural transitions observed in TEM (Fig. 4.1b-e). At 12 mM [TMB], the SAXS pattern shows reflections consistent with hexagonal symmetry. When [TMB] is increased to 29 mM, a well-resolved set of cubic $Pm\bar{3}n$ reflections from the particle cores is superposed with a prominent set of hexagonal *p*6*mm*

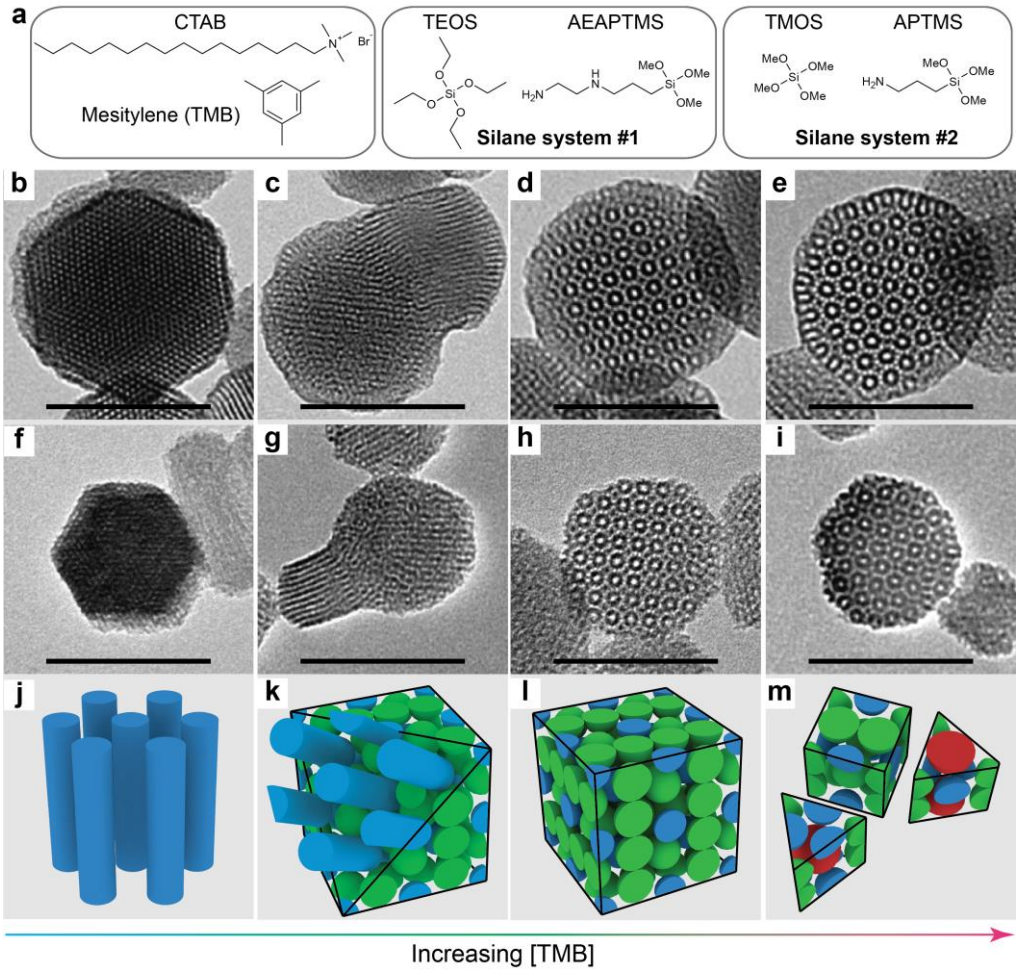

Figure 4.1. Four mesoporous silica nanoparticle structures observed in two silane systems as a function of mesitylene concentration **a,** Chemical structures of key reagents used in tetraethyl orthosilicate/N-(2-aminoethyl)-3-aminopropyltrimethoxysilane (TEOS/AEAPTES) and tetramethyl orthosilicate/(3-aminopropyl)trimethoxysilane (TMOS/APTMS) synthesis systems. **b-e,** Transmission electron microscopy (TEM) images of mesoporous silica nanoparticles prepared from TEOS/AEAPTMS with (**b**) 12 mM, (**c**) 29 mM, (**d**) 47 mM, and (**e**) 116 mM mesitylene (TMB), using constant ammonium hydroxide concentration (13.8 mM) and stirring rate (650 rpm). **f-i,** TEM images of mesoporous silica nanoparticles prepared from TMOS/APTMS with (**f**) 4 mM, (**g**) 10 mM, (**h**) 14 mM, and (**i**) 72mM TMB, using constant ammonium hydroxide concentration (150 mM) and stirring rate (600 rpm). **j-m,** Micelle packing models corresponding to mesoporous silica nanoparticles in (**b**) to (**i**). All images have the same magnification; scale bars are 100 nm.

reflections from the particle arms. This pattern is consistent with previously reported SAXS measurements from multicompartment MSNs[19]. At 47 mM [TMB], the SAXS pattern shows reflections consistent with a cubic particle with $Pm\bar{3}n$ lattice[24]. Expected peak positions for cubic $Pm\bar{3}n$ and hexagonal *p6mm* are indicated in the SAXS patterns using solid and dashed lines, respectively (Fig. C.2). As [TMB] is further increased to 116 mM and beyond, the SAXS patterns lose more and more features and lattices cannot unambiguously be assigned. TEM tilt series (Fig. C.3) as well as TEM tomography failed to establish the three-dimensional particle structure, the latter as a result of severe beam damage of the organic-silica hybrids during data acquisition.

To deconvolute the effects of [TMB] from the specifics of the silica chemistry, we examined a second, independent organosilane system, composed of tetramethyl orthosilicate (TMOS) and (3-aminopropyl)trimethoxysilane (APTMS) (Fig. 4.1a). MSNs synthesized using TMOS and APTMS showed similar transitions as a function of increasing [TMB] (Fig. 4.1f-i). Comparison between the TEOS/AEAPTMS and TMOS/APTMS systems suggests that the observed structural transitions do not depend on the specifics of silane and aminosilane molecules used here. However, it is important to note that the presence of an aminosilane is critical for the formation of quasicrystalline mesoporous silica nanoparticles (Fig. C.4a, b). This observation is consistent with our expectation that the aminosilane mediates changes in the packing behavior of the CTAB surfactant[24, 25], facilitating the formation of more complex nanostructures[19, 20, 26].

Pore patterns of MSNs like the ones in Figure 4.1e were tiled using squares and equilateral triangles (Fig. C.2a, b). These MSNs exhibit two distinctive features of dodecagonal quasicrystals. Fast Fourier transform (FFT) analysis of TEM images reveals 12-fold symmetry and no translational periodicity is observed in the 2-

dimensional tiling patterns extracted from the TEM images (Fig. C.2a, b)[11]. The tile edges correspond to dodecagonal directions and each vertex can be described by $\mathbf{r}^{//} = n_1\mathbf{e}_1^{//} + n_2\mathbf{e}_2^{//} + n_3\mathbf{e}_3^{//} + n_4\mathbf{e}_4^{//}$ (Fig. 2b). Each vertex in parallel (Fig. 4.2c) space corresponds to a unique vertex in perpendicular (Fig. 4.2d) space[30]. Figures 4.2c and d show by color how individual points move during this transformation. A comparison of the radii of gyration in perpendicular and parallel space, $R_g\perp$ vs. $R_g//$, is a measure of the quasicrystallinity of a pattern: the more a pattern shrinks, the more quasicrystalline it is (compare patterns in Fig. 4.2c to d).

Synthesis of MSNs with varying size and quasicrystallinity

We systematically investigated the growth of dodecagonal tilings in mesoporous silica all the way down to a single tiling unit by capitalizing on well-established silica chemistry to control particle size. The comparatively fast hydrolysis of TMOS relative to TEOS facilitated access to smaller MSNs[21]. Precise particle size control in this system was further achieved using variations in reaction pH, where the increasing condensation rate associated with lowered pH resulted in smaller particle sizes[31]. In this way, MSNs could be synthesized with sizes < 30 nm such that associated tilings were composed of a single triangle or square tiling unit. TEM images of quasicrystalline MSNs, synthesized using constant [TMB] and varying ammonium hydroxide concentration, [NH_4OH], are shown in the bottom row of Fig. 4.2e. Interestingly, qualitative assessment of the triangle-square tilings extracted from these images suggests that quasicrystallinity does not vary with changes in reaction pH.

Increasing [TMB] from 14 mM to 72 mM introduces a gradual transition from cubic to quasicrystalline pore structure, where triangle-square tilings extracted from MSNs synthesized using intermediate [TMB] are mixed phase rather than purely cubic

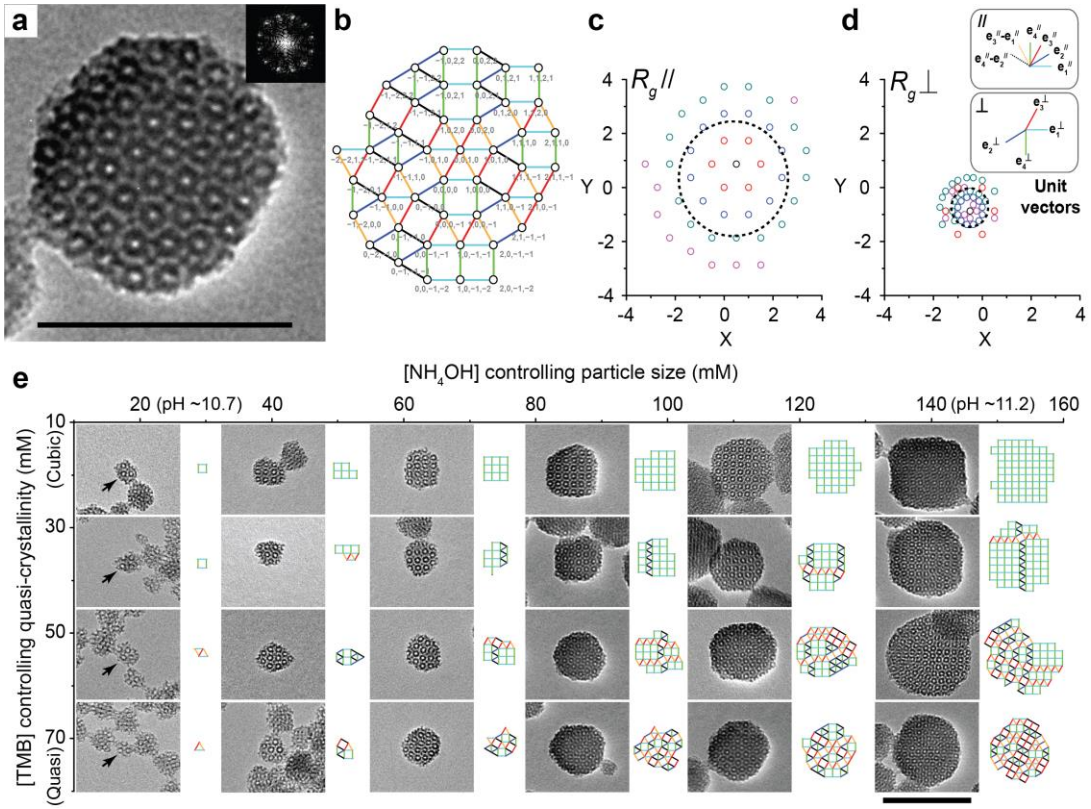

Figure 4.2. Quasicrystallinity of tetramethyl orthosilicate/(3-aminopropyl)trimethoxysilane derived mesoporous silica nanoparticles. **a,** Transmission electron microscopy (TEM) image of a mesoporous silica nanoparticle with dodecagonal symmetry, synthesized using tetramethyl orthosilicate and (3-aminopropyl)trimethoxysilane. The scale bar is 100 nm. The insert in (**a**) shows a Fourier diffractogram of the TEM image exhibiting 12-fold symmetry. **b,** Square-triangle tiling and parallel space coordinates of the nanoparticle shown in (**a**). Edges with different colors correspond to the six dodecagonal directions in parallel space. The corresponding dodecagonal directions in parallel and perpendicular space are shown in (**d**). **c, d,** Parallel and perpendicular space coordinates for the triangle-square tiling shown in (**b**). Dotted circles with radius equal to R_g// and $R_g\perp$ are shown on the parallel and perpendicular space plots, respectively. The colors in (**c**) and (**d**) show how individual points move during the transformation. **e,** TEM images and corresponding square-triangle tilings of representative mesoporous silica nanoparticles (arrows) synthesized from different concentrations of mesitylene (TMB) and ammonium hydroxide (NH_4OH). The stirring rate was 600 rpm for all syntheses. All images have the same magnification; scale bar is 100 nm.

or quasicrystalline. Tuning reaction pH at low and intermediate [TMB] again resulted in particle sizes ranging from > 100 nm down to < 30 nm with no observable pH dependent variations in pore structure. Figure 4.2e illustrates the range of particle structures obtained from over ~50 synthesis batches of particles (see also Fig. C.4).

Quantitative analysis of micelle size distributions

Although the observed MSN structures result from cooperative interactions between the CTAB micelles and the silica species[32], the above observations point to the starting micelle size distribution as a key factor in the formation of quasicrystalline MSNs. Recent reports provide supporting evidence for the role of building block polydispersity in self-assembly, demonstrating that particles with broad monomodal or bimodal size distributions form more complex structures[7, 8, 33]. We have characterized the starting micelle sizes using cryo-TEM (Fig 4.3). Representative micelle size distributions from native CTAB/TMB solutions prepared using increasing [TMB] and constant stirring rate are shown in Figure 4.3a-d. Micelle solutions prepared without TMB or using low [TMB] (4mM) led to formation of hexagonal MSNs (Fig. 4.3k and l) whereas and use of high [TMB] (72 mM and 116mM) resulted in quasicrystalline MSNs (Fig. 4.3m and n). Comparison of the entire series reveals that increasing [TMB] causes a shift to larger average micelle diameter as well as an increase in the positive skewness of the micelle size distribution, e.g. compare numbers of micelles with sizes above 5 nm as [TMB] increases (Fig. 4.3a-d).

Cryo-TEM experiments further demonstrated that mechanical agitation (stirring), in addition to TMB, is a requirement for producing these broadened micelle size distributions (Fig. 4.3e, j, and o), consistent with recent observations of complex polymer micelle size distributions in the presence of a co-solvent and solution agitation[34]. Associated structural transitions are illustrated schematically by the

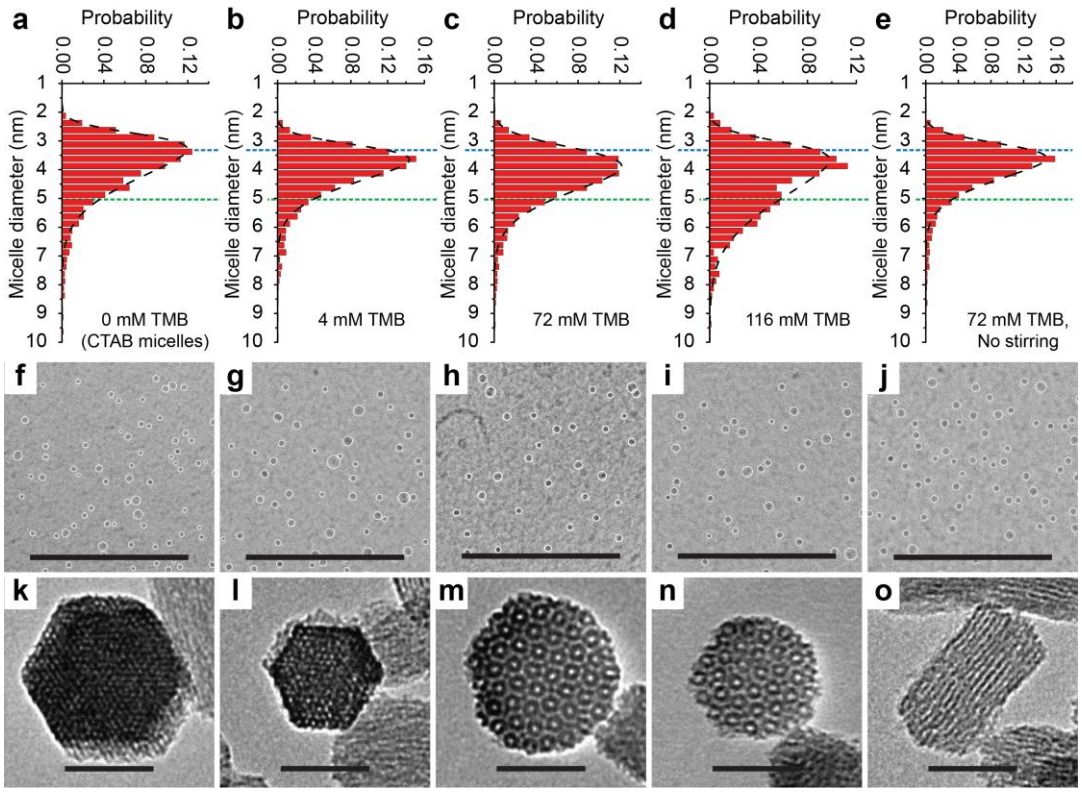

Figure 4.3. Cryo-transmission electron microscopy of native micelle solutions prepared using varying mesitylene concentrations and stirring rates. **a-e,** Micelle size distributions before silane addition, prepared using (**a**) 0 mM, (**b**) 4 mM, (**c**) 72 mM, and (**d**) 116 mM mesitylene (TMB) under constant stirring (600 rpm) and (**e**) 72 mM TMB with no stirring. The ammonium hydroxide concentration was kept constant (150 mM) across all solutions. Distribution fits are shown using black dashed lines. Blue dashed lines indicate the peak position of the micelle size distribution of hexadecyltrimethylammonium bromide (CTAB) micelles without TMB and green dashed lines are shown as an additional reference for comparison across different plots. Comparison between the micelle size distributions demonstrates that although the peak position does not vary substantially, the combination of increased TMB concentration and mechanical agitation, causes a shift to larger average micelle diameters and an increase in the frequency of large micelles with sizes above 5 nm. **f-j,** Cryo-transmission electron microscopy images of the micelle solutions before silane addition corresponding to conditions used in (**a**) to (**e**), respectively. Individual micelles are identified using a self-written python code and are circled in white. **k-o,** Transmission electron microscopy images of mesoporous silica nanoparticles synthesized via adding tetramethyl orthosilicate and (3-aminopropyl)trimethoxysilane into micelle solutions corresponding to conditions used in (**a**) to (**e**), respectively. Scale bars in both sets of images are 50 nm.

micelle packings in Figure 4.1j to m,[6, 35, 36] using a model with three discrete micelle sizes for simplicity. Hexagonal MSNs have channel-like pores templated by elongated CTAB micelles (blue) (Fig. 4.1j). Multicompartment MSNs are composed of a $Pm\bar{3}n$ cubic core connected epitaxially at the (111) face to a hexagonal structure[19]. The $Pm\bar{3}n$ cubic core is composed of two types of spherical micelles, one of which is slightly larger (green) than the other (blue) due to increased TMB loading (Fig. 4.1k). As [TMB] is further increased, subsequently single phase $Pm\bar{3}n$ cubic MSNs (Fig. 4.1l) and MSNs with dodecagonal symmetry are formed, the latter incorporating even larger micelles (red) (Fig. 4.1m).

These observations are supported by pore size analysis of nitrogen sorption measurements on TEOS/AEAPTMS particles after CTAB removal that show marked pore size increase and broadening of the pore size distribution with increasing [TMB] (Fig. C.2). At 12 mM (hexagonal MSNs), the pore size distribution is well fit by a single log-normal distribution (Fig. C.5). However, as [TMB] is increased to 47 and 116 mM (cubic and quasicrystalline MSNs), the increasingly broadened pore size distributions can no longer be described by unimodal log normal fits, suggesting that additional micelle populations may be involved in the formation processes of these more complex structures. As a first approximation, these data are therefore fit using a superposition of two and three log-normal distributions, respectively (Supplementary Fig. 4.5). Average pore sizes extracted from these fits (Table C.1) support the hypothesis that the structural changes observed with increasing [TMB] are due to the presence of additional, larger micelle populations. Additional experiments demonstrated that the same structural transitions and pore size increases were achieved using constant [TMB] (29 mM) but increased stirring rates which also affects micelle size (Fig. C.5 and C.6).

Tiling analysis

The MSNs shown in Figs. 4.1e and i exhibit indicators of quasicrystallinity (i.e. 12-fold symmetric Fourier diffractogram and no translational periodicity). Since there are no local constraint rules that enforce quasicrystallinity in systems of triangles and squares, quasicrystallinity in these finite structures is instead characterized by statistical analysis of the phason coordinates. We analyzed the tilings extracted from the TMOS/APTMS derived MSNs synthesized as a function of increasing [TMB] (Fig. 4.2e and Fig. 4.4). Figure 4.4a shows a plot of $R_g\perp$ versus $R_g//$ calculated from the tilings of individual MSNs synthesized with systematic variations in [TMB] and [NH_4OH]. The slope of the linear fit $R_g\perp = AR_g// + B$ provides the magnitude of the phason strain, a quantitative measure of quasicrystallinity[6, 30]. MSNs synthesized at the highest [TMB] (72 mM) and varying pH lie on the same line, which is well described by the fit with phason strain equal to 0.14 (see TEOS/AEAPTMS data in Fig. C.7) approaching the zero-phason strain of a dodecagonal quasicrystal[6] and consistent with the phason behavior of a random tiling quasicrystal[30]. Additionally, the fit demonstrates that these MSNs have similar quasicrystallinity, which contrary to previous studies[6], is independent of the reaction pH and pH-induced changes in the interaction potentials between micelles.

TEM images of MSNs synthesized using low [TMB] and varying pH (Fig. 4.2e and Fig. C.4) exhibit predominantly cubic structure. Interestingly, a few quasicrystalline MSNs are always found in a batch of cubic MSNs, resulting in a slope that is slightly smaller than 1, i.e., the phason strain of a perfectly cubic crystal. Comparison between MSNs synthesized using low and high [TMB] demonstrates that changes in quasicrystallinity are due to differences in [TMB] rather than pH. Particles synthesized at intermediate [TMB] between 22 mM and 50 mM exhibited substantial fluctuations in the plot of $R_g\perp$ versus $R_g//$ (Fig. 4.4a). More specifically, individual

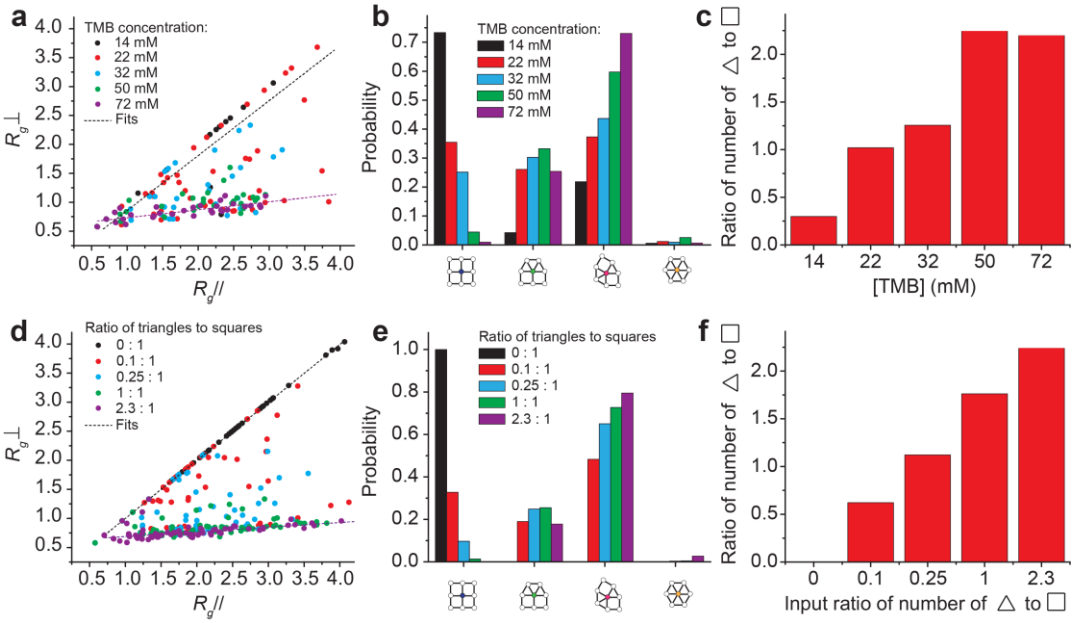

Figure 4.4. Analysis of tetramethyl orthosilicate/(3-aminopropyl)trimethoxysilane derived mesoporous silica nanoparticles and simulated structures. **a,** Plot of R_g in perpendicular vs. parallel space, calculated for mesoporous silica nanoparticles synthesized from five different mesitylene (TMB) concentrations. **b,** Distribution of pore conformers (4^4, 3^34^2, $3^24^13^14^1$ and 3^6) calculated for particles synthesized from five different TMB concentrations. **c,** Ratio of triangle to square tiles calculated for particles in (**a**). **d-f**, Plots corresponding to (**a**) to (**c**) for 500 particles derived from simulations with five different triangle to square ratios.

particles from a single batch of MSNs synthesized in this regime may be cubic, quasicrystalline, or mixed phase, suggesting that not only [TMB] and stirring rate but also other factors are at play.

From the tiling analysis the distribution of four fundamental geometrical conformations was derived for all batches/particles, i.e. 4^4, 3^34^2, $3^24^13^14^1$ and 3^6, where 4 and 3 represent square and triangle base units and the exponent indicates the number of adjacent base units incident on a single vertex (Fig. 4.4b). This analysis shows that with increasing [TMB], cubic 4^4 conformers decrease, 3^34^2 conformers first increase but then roughly stay constant, and $3^24^13^14^1$ conformers increase. All MSN samples analyzed have low abundance of 3^6 conformers. At the same time, the ratio of the overall numbers of triangles to squares increases with [TMB] (Fig. 4.4c). Considering that the triangle tile contains the largest micelles (Fig. 4.1m), these data imply that the presence of large micelles plays a key role in quasicrystal formation. The growth of quasicrystals may also be highly dependent on the dynamic packing process of differently sized micelles forming triangle and cubic tiles, as indicated by the substantial phason strain fluctuations of the MSNs synthesized at intermediate [TMB]. Simulations were carried out in order to elucidate the origin of these fluctuations and reveal dominant factors in this [TMB] regime.

Simulated single particle growth trajectories

Quasicrystal growth has previously been modeled in 2-dimensions using triangle-square tilings[6, 13, 37]. We have developed an irreversible MSN growth model that produces 2D tilings that mimic the observed features of our experimental system (see Supplementary Methods for details). Particle growth in these simulations proceeds via irreversible aggregation of square and equilateral triangle tiles. This accounts for experimental observations wherein packings of small and medium sized

micelles result in square tiles (green and blue in Fig. 4.1l) and the involvement of a third larger micelle gives rise to triangle tiles (red in Fig. 4.1m). Each tile is randomly chosen from a weighted shape distribution given by an input triangle/square number ratio that reflects the increasing number of triangles observed in MSNs synthesized at increasing [TMB] (Fig. 4.4b, c). The probability of tile attachment on the growing cluster is governed by both shape and site specific interaction parameters. We also include an additional threshold parameter that allows the system to choose replacement tiles if attachment probabilities above a minimum value do not exist. For each triangle/square ratio, several batches of particles with size distributions that approximately match those of experimentally observed particles were generated. Simulated particles were analyzed according to the methods outlined for the experimental particles. Although this is a simplified model, comparison of Fig. 4.4d through f with Fig. 4.4a through c shows that it was sufficient to reproduce the experimentally observed features. These results suggest that the structural transition observed is primarily a function of the triangle/square ratio or micelle size distribution in an irreversible, random growth process.

Analysis of simulated single particle growth trajectories (Fig. 4.5a) shows the relationship between quasicrystallinity ($R_g\perp$ vs. $R_g//$) and the size of the particle or the number of square tiles present (plotted along the z-axis) when the first triangle is added. For perfect cubic particles, the total number of squares at the end of the simulation is counted instead. At the highest triangle/square input ratio of 2.3 (*38*), all data points (purple) are highly concentrated in a low z range in Fig. 4.5a, suggesting that in this irreversible tiling process, the early appearance of a first triangle contributes to the growth of highly quasicrystalline particles. By comparison, the appearance of the first triangle in particles with a triangle/square input ratio of 0.1 (red) is widely distributed in the growth process causing the spread in

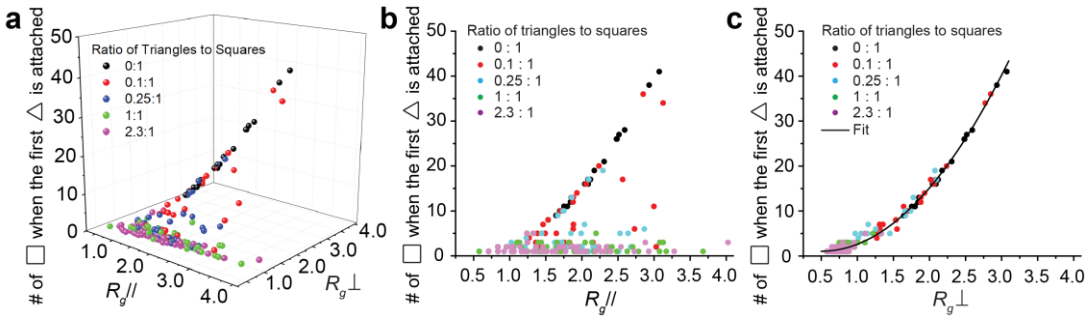

Figure 4.5. Analysis of simulated single particle growth trajectories. **a,** 3D plot showing that phason strain is highly dependent on the time at which the first triangle is added to the growing particle. **b, c,** 2D projections of the 3D plot in (**a**). The data in (**c**) is fitted using equation $Na^2 = AR_g\perp^2 + aBR_g\perp + a^2C$, where $a = 1$ is the edge length of a square tile, N is the number of tiles, and A, B and C are fitting parameters. This is consistent with the theoretical relationship between the area and the radius of gyration, R_g, of a 2D square packing pattern (Supplementary Methods).

quasicrystallinity observed in Fig. 4.4d. 2D projections of Fig. 4.5a, which represent the dependence of R_g// and $R_g\perp$ on the timing (i.e. particle size) of the first triangle addition are shown in Figs. 4.5b and c, respectively. In Fig. 4.5c, all data points fall onto a master curve, $N = N(R_g\perp)$, that relates the area of a 2D square tiling pattern ($\propto N$) to its radius of gyration (see Supplementary Methods).

Side-by-side comparison of Figs. 4.5b and c reveals that the first triangle addition seeds the growth of a quasicrystalline phase. While particle growth in real (parallel) space does not depend on the timing of the triangle addition, particle growth in perpendicular space is mostly terminated as soon as the first triangle is added. Single particle growth trajectories (Fig. 4.6) of two simulated particles with the same triangle/square input ratio (0.1) illustrate this effect. Similarities between tilings from TEM images of particles synthesized at intermediate [TMB] and tilings of simulated particles at various stages of growth support the assumption that the formation of MSNs with dodecagonal tilings can be described using our model (Fig. 4.6).

Discussion

We have discovered a series of four different structures in mesoporous silica nanoparticles, including dodecagonal tiling, as a function of either pore expander concentration or stirring rate. Precise control of highly tunable silica sol-gel chemistry together with growth simulations has enabled identification of the early growth trajectories of quasicrystalline mesoporous silica nanoparticles. Our results suggest that skewed micelle size distributions as mapped by cryo-state TEM frustrate crystal formation and favor the growth of quasicrystalline structures. Our experiments further suggest that this skewness can be induced either by increasing amounts of micelle pore expander, or by simple increase of stirring rate. These results imply that size polydispersity of building blocks, rather than pH dependent changes in interaction

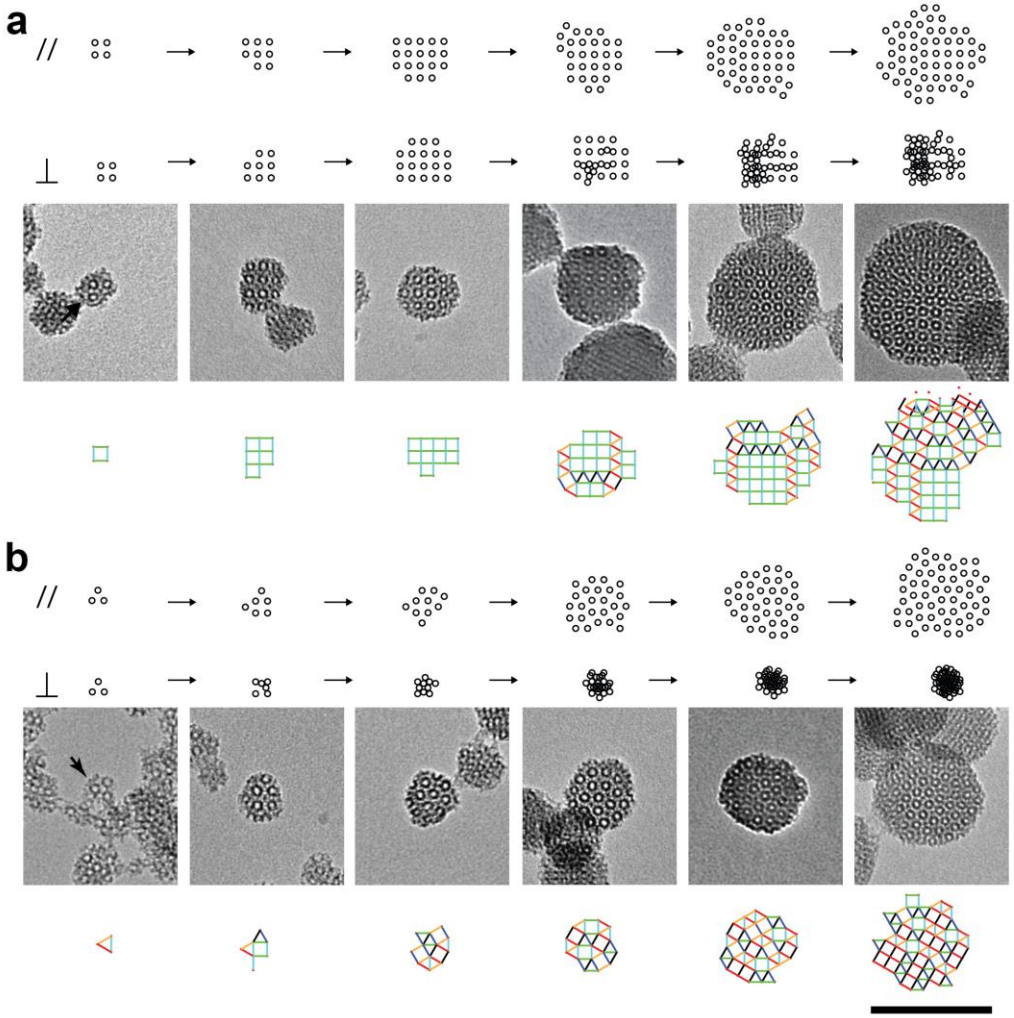

Figure 4.6. Comparison of simulated growth trajectories with tetramethyl orthosilicate/(3-aminopropyl)trimethoxysilane derived mesoporous silica nanoparticles. **a, b,** Single particle growth trajectories of two simulated particles with input triangle/square ratio equal to 0.1 with vertices plotted in both parallel and perpendicular space. Simulated growth stages are compared to experimental TEM images of tetramethyl orthosilicate/(3-aminopropyl)trimethoxysilane derived mesoporous silica nanoparticles and their tilings. Particles were synthesized under varying ammonium hydroxide and mesitylene concentrations as shown in Fig. 2e. The stirring rate was 600 rpm for all syntheses. All images have the same magnification; scale bar is 100 nm.

potentials between building blocks as suggested earlier,[6] is the primary factor in triggering the growth of quasicrystalline mesoporous silica structures.

Our results suggest that due to fast silane condensation, quasicrystalline mesoporous silica nanoparticles are likely formed via an irreversible micelle packing process. Although the micelles studied here are unlikely to undergo the local structural rearrangements that are observed in metal alloys during high temperature processing steps[14], we expect that the simple synthetic control parameters we have identified can be translated to a wide variety of self-assembled systems. The accessibility of the experimental control parameters we introduce in this study may simplify the design of alternative self-assembly chemistries for studying quasicrystal growth, especially in systems of polymer micelles where addition of co-solvents and mechanical agitation have already been shown to affect building block polydispersity[34]. Finally, although we are limited by the silica chemistry to relatively small particle sizes, the experimental observation of quasicrystal formation via an irreversible growth mechanism may provide fundamental insights into the origin of quasicrystallinity in other materials systems.

4.5 Acknowledgements

This work was supported by the U.S. Department of Energy, Office of Science, Basic Energy Sciences, under Award No. DESC0010560. T.K. acknowledges support from the NSF IGERT program (DGE-0966188). K.A.S. and L.F.K. acknowledge support by the Cornell Center for Materials Research (CCMR) with funding from the NSF MRSEC program (DMR-1120296). K.M. and D.Z. thank K. Xie (University of Virginia) for assistance with the development of an automated tiling program. This work made use of the CCMR shared facilities, and the Nanobiotechnology Center shared research facilities at Cornell. The Titan Themis 300 was acquired through NSF-MRI-

1429155, with additional support from Cornell University, the Weill Institute and the Kavli Institute at Cornell. This work is based upon research conducted at the Cornell High Energy Synchrotron Source (CHESS), which is supported by the National Science Foundation and the National Institutes of Health/National Institute of General Medical Sciences under NSF award DMR-1332208.

REFERENCES

1. Shechtman, D., Blech, I., Gratias, D. & Cahn, J. Metallic Phase with Long-Range Orientational Order and No Translational Symmetry. *Phys. Rev. Lett.* **53**, 1951-1953 (1984).

2. Förster, S., Meinel, K., Hammer, R., Trautmann, M. & Widdra, W. Quasicrystalline structure formation in a classical crystalline thin-film system. *Nature* **502**, 215-218 (2013).

3. Zeng, X. *et al*. Supramolecular dendritic liquid quasicrystals. *Nature* **428**, 157-160 (2004).

4. Hayashida, K., Dotera, T., Takano, A. & Matsushita, Y. Polymeric Quasicrystal: Mesoscopic Quasicrystalline Tiling in A B C Star Polymers. *Phys. Rev. Lett.* **98**, 195502 (2007).

5. Talapin, D. *et al*. Quasicrystalline order in self-assembled binary nanoparticle superlattices. *Nature* **461**, 964-967 (2009).

6. Xiao, C., Fujita, N., Miyasaka, K., Sakamoto, Y. & Terasaki, O. Dodecagonal tiling in mesoporous silica. *Nature* **487**, 349-353 (2012).

7. Huang, M., *et al.* Selective assemblies of giant tetrahedra via precisely controlled positional interactions. *Science* **348**, 424 – 428 (2015).

8. Yue, K., *et al.* Geometry induced sequence of nanoscale Frank-Kasper and quasicrystal mesophases in giant surfactants. *PNAS* **113**, 14195 – 14200 (2016).

9. Gillard, T.M., Lee, S., & Bates, F.S. Dodecagonal quasicrystalline order in diblock copolymer melt. *PNAS* **113**, 5167 – 5172 (2016).

10. Lee, S., Leighton C., & Bates, F.S. Sphericity and symmetry breaking in the formation of Frank-Kasper phases from one component materials. *PNAS* **111**, 17723-17731 (2014).

11. Iacovella, C.R., Keys, A.S. & Glotzer, S.C. Self-assembly of soft-matter quasicrystals and their approximants, *PNAS* **108**, 20935 – 20940 (2011).

12. Van der Linden, M. N., Doye, J. P. K. & Louis, A. A. Formation of dodecagonal quasicrystals in two-dimensional systems of patchy particles. **136**, 054904 (2012).

13. Joseph, D. & Elser V. A model of quasicrystal growth, *Phys. Rev. Lett.* **79**, 1066 – 1069 (1997).

14. Nagao, K., Inuzuka, T., Nishimoto, K., Edagawa, K. Experimental observation of quasicrystal growth. *Phys. Rev. Lett.* **115**, 075501 (2015).

15. Yanagisawa, T. Shimizu, K., Kuroda, K., Kato, C. The preparation of alkyltrimethylammonium-kanemite complexes and their conversion to microporous materials. *Bull. Chem. Soc. Jpn.* **63**, 988-992 (1990).

16. Kresge, C., Leonowicz, M., Roth, W., Vartuli, J. & Beck, J. Ordered mesoporous molecular sieves synthesized by a liquid-crystal template mechanism. *Nature* **359**, 710-712 (1992).

17. Hoffman, F., Cornelius, M., Morell, J., & Fröba, M. Silica-Based Mesoporous Organic-Inorganic Hybrid Materials. *Angew. Chem. Int. Ed.* **45**, 3216 – 3251 (2006).

18. Sakamoto, Y. *et al*. Direct imaging of the pores and cages of three-dimensional mesoporous materials. *Nature* **408**, 449-453 (2000).

19. Suteewong, T. *et al*. Multicompartment Mesoporous Silica Nanoparticles with Branched Shapes: An Epitaxial Growth Mechanism. *Science* **340**, 337-341 (2013).

20. Suteewong, T. *et al.* Highly Aminated Mesoporous Silica Nanoparticles with Cubic Pore Structure. *J. Am. Chem. Soc.* **133**, 172-175 (2011).

21. Ma, K., Sai, H. & Wiesner, U. Ultrasmall Sub-10 nm Near-Infrared Fluorescent Mesoporous Silica Nanoparticles. *J. Am. Chem. Soc.* **134**, 13180-13183 (2012).

22. Gao, C., Sakamoto, Y., Terasaki, O. & Che, S. Formation of diverse mesophases templated by a diprotic anionic surfactant. *Chem. Eur. J.* **14**, 11423 – 11428 (2008).

23. Huo, Q. *et al*. Generalized synthesis of periodic surfactant/inorganic composite materials. *Nature* **368**, 317-321 (1994).

24. Suteewong, T. *et al*. Synthesis and Formation Mechanism of Aminated Mesoporous Silica Nanoparticles. *Chem. Mater.* **24**, 3895-3905 (2012).

25. Huh, S., Wiench J.W., Yoo, J., Pruski, M. & Lin, V.S.Y. Organic Functionalization and Morphology Control of Mesoporous Silicas via a Co-Condensation Synthesis Method. *Chem. Mater.* **15**, 4247-4256 (2003).

26. Ziherl, P. & Kamien, R.D. Maximizing Entropy by Minimizing Area: Towards a New Principle of Self-Organization. *J. Phys. Chem. B.* **105**, 10147-10158 (2001).

27. Ottaviani, M. F. *et al.* Synthesis of Micelle-Templated Silicas from Cetyltrimethylammonium Bromide/1,3,5-Trimethylbenzene Micelles. *J. Phys. Chem. B.* **108**, 12123-12129 (2004).

28. Schmidt-Winkel, P. *et al.* Microemulsion Templating of Siliceous Mesostructured Cellular Foams with Well-Defined Ultralarge Mesopores, *Chem. Mater.* **12**, 686 – 696 (2000).

29. Blin, J.L. & Su B.L. Tailoring Pore Size of Ordered Mesoporous Silicas Using One or Two Organic Auxiliaries as Expanders, *Langmuir* **18**, 5303 – 5308 (2002).

30. Oxborrow, M. & Henley, C. Random square-triangle tilings: A model for twelvefold-symmetric quasicrystals. *Physical Review B* **48**, 6966-6998 (1993).

31. Ma, K., Mendoza, C., Werner-Zwanziger, U., & Wiesner, U. Control of Ultrasmall Sub-10 nm Ligand-Functionalized Fluorescent Core-Shell Silica Nanoparticle Growth in Water. *Chem. Mater.* **27**, 4119-4133 (2015).

32. Firouzi, A. *et al.* Cooperative organization of inorganic-surfactant and biomimetic assemblies. *Science* **267**, 1138-1143 (1995).

33. Cabane, B. *et al.* Hiding in Plain View: Colloidal Self-Assembly from Polydisperse Populations. *Phys. Rev. Lett.* **116**, 208001 (2016).

34. Kelley, E.G. *et al.* Size evolution of highly amphiphilic macromolecular solution assemblies via a distinct bimodal pathway. *Nat. Commun.* **5**, 3599 (2014).

35. Frank, F.C. & Kasper, J.S. Complex alloy structures regarded as sphere packings. II. Analysis and classification of representative structures. *Acta Crystallogr.* **12**, 483 – 499 (1959).

36. Ye, X. *et al.* Quasicrystalline nanocrystal superlattice with partial matching rules. *Nat. Mater.* **16**, 214 – 219 (2016).

37. Kuo, K.H., Feng, Y.C. & Chen, H. Growth Model of Dodecagonal Quasicrystal Based on Correlated Tiling of Squares and Equilateral Triangles, *Phys. Rev. Lett.* **61**, 1740 – 1743 (1988).

38. Stampfli, P. A dodecagonal quasiperiodic lattice in two dimensions. *Helv. Phys. Acta* **59**, 1260 – 1263 (1986).

CHAPTER 5

A GROWTH MODEL FOR QUASICRYSTALLINE MESOPOROUS SILICA NANOPARTICLES

Abstract

Quasicrystals have been observed in a variety of soft materials systems, including block copolymers, dendrimers, and micelle templated mesoporous networks. While recent reports of soft quasicrystals have identified micelle polydispersity as a critical control parameter, their underlying assembly mechanisms remain a subject of study. Here, after demonstrating that the formation of quasicrystals in surfactant micelle-templated mesoporous silica nanoparticles is particularly sensitive to higher-order moments of the micelle size distribution, we provide a full account of an early growth model for dodecagonal quasicrystals, which is consistent with experimental observations. We evaluate the effects of a set of physically inspired tiling rules on the irreversible assembly of 2-dimensional, dodecagonal quasicrystals from equilateral triangle and square tiles. By making an analogy between size distribution in surfactant micelles and the relative availability of triangles and squares in our simulations, we elucidate an experimentally observed structural transition from crystal to quasicrystal. Finally, we extend our model to the continued growth of quasicrystalline seeds, arguing that similar structures may be observed in bulk, mesoporous silica quasicrystals.

---

[*] Prepared for Submission as: Teresa Kao, Kai Ma, Ulrich Wiesner. *A Growth Model for Quasicrystalline Mesoporous Silica Nanoparticles.*

Introduction

Since the discovery of quasicrystals in rapidly cooled metal alloys[1], similar structures have been observed in an expanding library of soft materials, including block copolymers[2, 3] and dendrimers[4, 5], as well as surfactant-templated mesoporous silica networks[6, 7] and nanoparticles[8, 9]. These advances have attracted widespread attention to the mechanisms that govern quasicrystal formation in soft-matter systems[3, 9, 10, 11]. Although direct experimental inquiries into quasicrystal growth remain challenging[12], recent reports have identified model quasicrystal-forming materials, including block copolymers[3], giant surfactants[11], and mesoporous silica[6, 9], that provide a platform for fundamental studies of quasicrystal formation mechanisms.

Mesoporous silica is a uniquely tunable self-assembly system, in which cooperative assembly of inorganic silica species and organic molecular templates produces a diverse range of structures, including dodecagonal quasicrystals[6, 8, 13, 14, 15]. As observed in other soft-matter systems[2, 4, 11], quasicrystals in mesoporous silica[6, 8, 9] are often found in close connection with periodic approximant structures, such as the A15- or σ-phases. The macroscopic form of these materials (e.g. particle size) can be precisely controlled by choice of silica precursor, solvent, and reaction pH[8, 15, 16]. Because the synthesis of mesoporous silica provides easily accessible control parameters that dictate both particle size and mesostructure, it represents an ideal model system for fundamental investigations of early quasicrystal growth mechanisms.

Computer simulation studies have predicted that quasicrystals can be assembled from a variety of two- and three-dimensional building blocks[10, 17, 18]. For example, in systems of approximately spherical building blocks, modeled after block copolymer and surfactant micelles, dodecagonal quasicrystals have been reported to form as a consequence of increased micelle size or shape polydispersity[10, 11]. These

assembly strategies are particularly attractive because they rely on readily accessible, experimental parameters for tuning micelle polydispersity[11, 19]. In this context, simulation studies of mesoporous silica provide a unique perspective on quasicrystal growth, in which micelle assembly is effectively irreversible, due to the fast formation of the matrix material[9].

Recently, to the best of our knowledge for the first time, we reported on nanoparticles with quasicrystalline structure[8, 9]. Our studies revealed surfactant-directed synthesis of quasicrystalline mesoporous silica nanoparticles (MSNs) exhibiting dodecagonal tiling, with dimensions less than 100 nm. In this system, the addition of a micelle-swelling agent or, equivalently, an increase in solution stirring rate, induced a gradual transition between four distinct nanoparticle mesostructures, ranging from crystalline to quasicrystalline[8, 9]. Additionally, precise control of particle size facilitated direct comparison with a simple theoretical growth model that reproduced experimentally observed, structural trends[9]. Here, after examining the role of higher-order moments of experimentally determined micelle size distributions in quasicrystal formation, we provide a full account of this quasicrystal growth model. We introduce the set of tiling rules used in the assembly of equilateral triangle and square building blocks and evaluate their effects on the quasicrystallinity of the resulting particles. We reproduce the experimentally observed structural transition from crystal to quasicrystal and by investigating the growth pathways of these simulated particles, we elucidate the mechanism that governs quasicrystal formation in mesoporous silica. Finally, we extend our model to quasicrystal growth beyond the nanoparticle sizes observed in our experiments and compare the resulting structures to examples of micron-sized quasicrystalline mesoporous silica materials[6]. We expect that our findings, supported by a simple model, may have implications beyond

quasicrystal formation in mesoporous silica, potentially providing mechanistic insights into other quasicrystal-forming materials systems.

Methods

Experimental System and Size Distribution of Building Blocks.

The work in this article is based on a surfactant micelle-templated MSN system, where a crystal to quasicrystal transition has previously been observed as a function of micelle size distribution (Figure 5.1). Details of the synthesis and characterization of these MSNs have been described elsewhere[9]. Briefly, MSNs were synthesized by co-condensing a mixture of silane precursors, tetramethyl orthosilicate (TMOS) and (3-aminopropyl)trimethoxysilane (APTMS), in the presence of hexadecyltrimethylammonium bromide (CTAB) surfactant micelles. The micelle size/size distribution was tailored either by varying the concentration of a micelle swelling agent (trimethylbenzene, TMB), [TMB], added to the MSN synthesis or by varying the rate of solution stirring.

Micelle size distributions were quantitatively characterized using cryo-transmission electron microscopy (cryo-EM)[9] of the native micelle solutions, prior to silane addition (Figure 5.1a). Distributions were well-described using a log-normal function:

$$y = \frac{1}{\sqrt{2\pi}\sigma x} e^{-\frac{(\ln x - \mu)^2}{2\sigma^2}},$$

where μ and σ are location and scale parameters, respectively[20]. Such log-normal distribution functions are typically used in cases where the underlying physics is described by multiplicative effects[21], which is also the case here of surfactant micelle self-assembly as described, e.g. by Israelachvili[22]. Figure 5.1a shows that micelle size distributions shifted to larger average micelle diameters, e.g. as a function of increasing [TMB], but at the same time became increasingly asymmetric. As a

reference for comparison of micelle size distributions obtained using different [TMB], we have also indicated the positions of mean (green) and mode (blue) calculated from each of the log-normal fits superimposed on the experimental cryo-EM data in Figure 5.1a. These parameters were calculated using the equations:

$$Mean = e^{\mu + \sigma^2/2}$$

and

$$Mode = e^{\mu - \sigma^2},$$

where σ and μ values were obtained from the log-normal fits shown in Figure 5.1a[20]. As expected for increasingly asymmetric distributions, we observe an increase in the separation between the positions of mean (green) and mode (blue) as a function of increasing [TMB].

TMB-induced changes in the micelle size distribution can also be quantified by calculating moments of the size distribution function. Earlier studies have demonstrated that higher order moments can provide particular insights into specific physical phenomena[24, 25, 26] and are therefore also of interest in the context of quasicrystal formation. Indeed, as a function of [TMB] we observed more dramatic relative changes in the higher-order size distribution moments, e.g. the fourth size distribution moment, kurtosis, as compared to the lower moments (Figure 5.1b). Kurtosis describes the tails of a distribution relative to a normal distribution, with positive values corresponding to wider tails. Here, kurtosis was calculated as follows:

$$kurtosis = e^{4\sigma^2} + 2e^{3\sigma^2} + 3e^{2\sigma^2} - 6,$$

where σ values were again obtained from the log-normal fits[23]. Results reveal that the formation of quasicrystalline structures is particularly sensitive to the higher order moments of the micelle size distribution, *i.e.* to the presence of more and more pronounced micelle size distribution tails with larger sizes than the mean. The same tails could also be observed with increasing stirring rate, independent from [TMB][9].

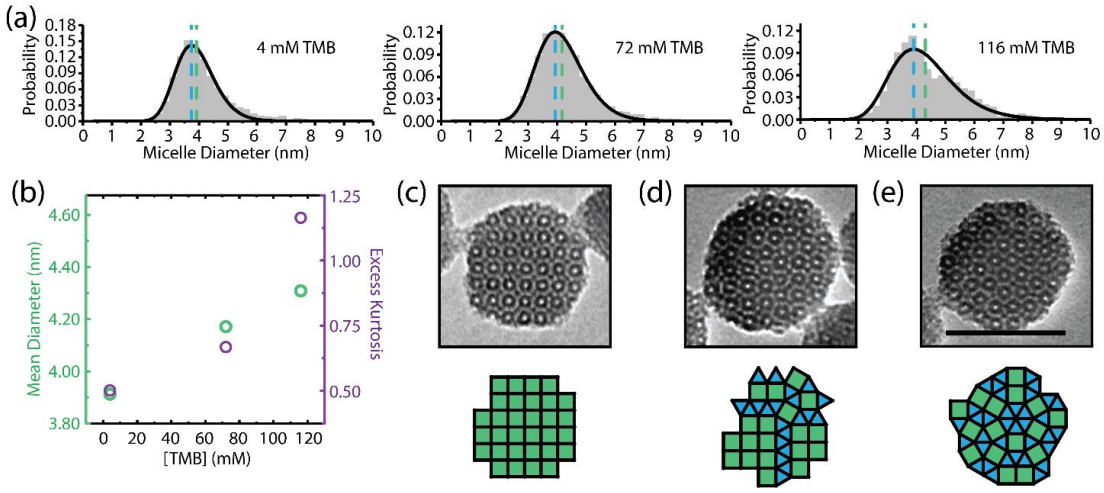

Figure 5.1. (a) Micelle size distributions from cryo-TEM images of native micelle solutions prior to silane addition, prepared using 4 mM, 72 mM, or 116 mM TMB. Solid black lines denote log-normal distribution fits. Green and blue dashed lines indicate positions of the calculated mean and mode, respectively. (b) Mean micelle diameter and excess kurtosis calculated from log-normal fits of micelle size distributions in (a). TEM images of MSNs and associated triangle-square tilings obtained from syntheses using (c) 4 mM, (d) 50 mM, and (e) 72 mM TMB. Scale bar for all images is 100 nm.

Since increasing stirring rate also leads to a crystal to quasicrystal transition (*vide supra*), our findings point to a more general significance of higher order moments of the size distribution of the specific building blocks in quasicrystal formation.

Computational Model and Approach and Relation to Building Block Size.

Statistical analysis of 2-dimensional (2D) MSN "tiling" patterns, constructed from TEM images by connecting the centers of neighboring mesopores to form equilateral triangle or square tiles, showed that increasing [TMB], translated to an increasing number of triangles relative to squares in the ensemble of MSNs[9]. TEM images of representative cubic crystalline (Figure 5.1c), mixed phase (Figure 5.1d), and quasicrystalline (Figure 5.1e) MSNs are shown in Figure 5.1, alongside the corresponding triangle-square tiling patterns. In this system, MSNs with dodecagonal quasicrystalline mesopore patterns were observed at high [TMB], or high stirring rates, thereby correlating the triangular tiles/building blocks with the presence of the asymmetric tails of the micelle size distributions templating silica growth, i.e. with micellar building blocks of sizes substantially larger than their mean size.

Quasicrystals have previously been modeled as 2D tilings of equilateral triangle and square tiles[17, 27, 28]. In this study, quasicrystalline MSNs are constructed using the same basic tiling units. Due to the fast kinetics of the silica matrix formation[16], particle growth is modeled as an irreversible aggregation of tiles[6]. Growth is seeded by an individual triangle or square tile and proceeds by sequential edge-to-edge attachment of additional tiles, which represent clusters of surfactant micelles[3, 6, 27]. To model fluctuations in the local micelle size distribution, incoming tiles are chosen randomly from a weighted probability distribution defined by an input number ratio of triangles to squares (S). Candidate growth sites on the boundary of the growing cluster are assigned interaction

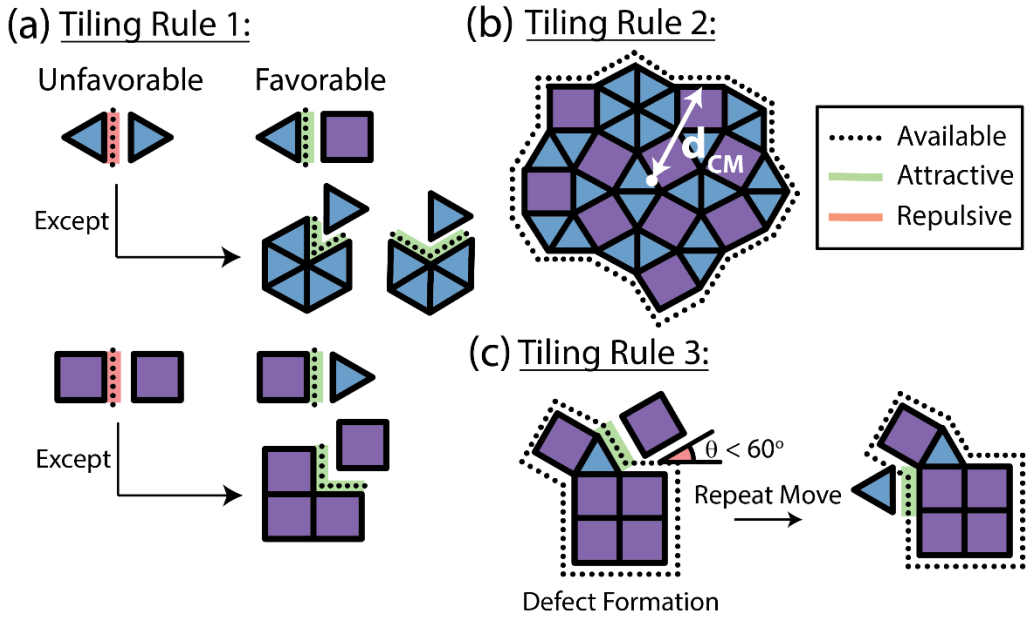

Figure 5.2. Schematic illustration of the proposed assembly model. (a) Tiling Rule 1 uses shape-specific interactions to promote formation of dodecagonal tilings. The shape of an available site (square or triangle) determines if interaction with an incoming tile is attractive (green) or repulsive (red). (b) Tiling Rule 2 favors tile attachment at sites near the mass center (CM) of the existing tiling. (c) Using Tiling Rule 3, the interaction parameter (P) is modified to avoid defect formation, based on the geometry of the tiles surrounding an available site. Tile attachment does not occur if newly generated sites cannot accommodate a triangle tile without overlapping the existing structure (i.e. if $\theta < 60°$). Instead, the choice of tile and site are repeated. Dotted lines represent available growth sites.

parameters (P) that govern the probability of tile attachment[6, 28]. In this model, final cluster size is determined at the start of each simulation by random choice from a weighted normal distribution of particle radii. In the following, we introduce the set of Tiling Rules needed to assemble quasicrystals using this basic framework (see Figure 5.2 for illustrations).

Tiling Rule 1. As previously suggested, a shape-specific component (P_s) is introduced in P that penalizes attachment of similar tiles (e.g. triangle-triangle), minimizing the formation of large cubic or hexagonal domains[6, 30]. Based on the associated energetics, Tiling Rule 1 does not apply in cases where attachment of similar tiles prevents defect formation (e.g. a square tile and a 90° concave corner). Figure 5.2a illustrates shape-specific interactions, where red and green halos imply repulsive and attractive interactions, respectively.

Tiling Rule 2. A surface (energy) minimizing component is introduced in P using an additional parameter, m. Although not explicitly formulated as a surface energy term, it reproduces the roughly spherical boundaries of the MSNs observed in TEM (Figure 5.1). Here, the distance (d_{CM}) of a candidate site from the mass center (CM) of the existing tiling is compared to the shortest radial distance (d_0) between an available growth site and the CM, such that candidate sites near the CM are preferred (Figure 5.2b).

Tiling Rule 3. When the selected growth site has P below a minimum threshold value (T), the system will repeat its choices of tile and site. The new tile and site are again chosen randomly from weighted probability distributions defined by S and P, respectively. To prevent defect formation, we set P equal to $P_0 < T$ if tile attachment would generate a concave corner that cannot accommodate a triangle tile without overlapping the existing structure (Figure 5.2c)[30]. In this irreversible tiling model, repeated tile and site selections are used as a short-cut to introduce local micelle

rearrangements during assembly. Although P_0 and T cannot be directly correlated to defect formation energy, they are used as fitting parameters to effectively adjust the degree of micelle rearrangement allowed before the assembly is arrested by silica matrix formation[33].

Our model was optimized by conducting a survey of the above parameters using a fixed triangle to square ratio (S = 2.3), chosen to match that observed in ideal quasicrystals[6, 31]. Roughly spherical tilings with quasicrystalline features were obtained using

$$P = P_s \times \left({}^{d_{CM}}/_{d_0} \right)^{-m},$$

where m = 10 and edge-to-edge contact between similar and dissimilar shapes were assigned $P_S = 0.001$ and $P_S = 0.75$, respectively. P_s was further modified to reflect the geometry of the tiles surrounding the candidate site, suppressing defect formation by favoring attachment of square tiles at concave 90º corners ($P_S = 0.75$) and triangle tiles at concave 60º and 120º corners ($P_S = 0.75$). The attachment threshold (T) was defined as T = 0.00075 x *d*. and $P_0 = 0.0000075$. For each set of conditions, we performed four sets of simulations containing 100 particles each, with size distributions defined using normal distributions with mean (μ) and variance (σ) defined as (μ, σ) = (1.5, 0.5), (3.5, 1.5), (6.0, 2.0), and (7.5, 2.5). These distributions were chosen to reflect the particle sizes observed in experiments as a function of pH[9].

We simulated the micelle size-dependent, structural trends observed in experiments[9] by varying the availability of triangles relative to squares (S)[30]. Our results demonstrate that this model reliably reproduces structural features observed in experiment over a range of S values (S = 0 to S = 2.3). We therefore employ this simple model to investigate the formation pathways of quasicrystalline mesoporous silica nanoparticles.

Tiling Analysis.

We evaluated the quasicrystallinity of the simulated structures using a previously described method[9], in which a triangle-square tiling may be viewed as a physical projection of a four-dimensional hyperlattice[27]. Every edge in the square-triangle tiling can be described by one of six dodecagonal directions in physical (parallel) space. If tile edges are assigned length a = 1 and a single vertex is designated as the origin of the tiling, all vertices can be described by the parallel space position vector

$$r^{\parallel} = n_1 e_1^{\parallel} + n_2 e_2^{\parallel} + n_3 e_3^{\parallel} + n_4 e_4^{\parallel},$$

where n_i is a unique set of integer coordinates and the dodecagonal directions are $e_i^{\parallel} = \{\cos(\alpha(i - 1)), \sin(\alpha(i - 1))\}$ with $\alpha = \pi/6$ and i = 1-4. The vertices of the triangle-square tiling in parallel space can be mapped onto a conjugate image in an orthogonal subspace (perpendicular space)[6, 27]. In perpendicular space, all vertices can be described by the position vector

$$r^{\perp} = n_1 e_1^{\perp} + n_2 e_2^{\perp} + n_3 e_3^{\perp} + n_4 e_4^{\perp},$$

where n_i is again a unique set of integer coordinates and $e_i^{\perp} = \{\cos(7\alpha(i - 1)), \sin(7\alpha(i - 1))\}$ with $\alpha = \pi/6$ and i = 1-4 (27).

The relative degree of scatter in the vertex arrangements in parallel and perpendicular space is a measure of the disorder in the tiling[27]. Therefore, quasicrystallinity can be assessed by comparing the radius of gyration of the pattern in parallel space ($R_g^{\parallel}$) to the radius of gyration of the conjugate image in perpendicular space ($R_g^{\perp}$)[9]. For a dodecagonal quasicrystal, where the tile arrangement has no translational order, vertices are concentrated to a small window in perpendicular space ($R_g^{\perp} << R_g^{\parallel}$). Conversely, the radius of gyration of a crystalline arrangement of triangles or squares remains unchanged upon transformation from parallel to perpendicular space ($R_g^{\parallel} = R_g^{\perp}$). Since the tilings described in this study are relatively

small, we rely on statistical analysis of an ensemble of structures to assess quasicrystallinity. The slope, A, of a linear fit to a plot of $R_g^{\perp}$ against $R_g^{\parallel}$ ($R_g^{\perp} = AR_g^{\parallel} + B$) is equal to the magnitude of the phason strain, a quantitative measure of the quasicrystallinity[9]. An ideal quasicrystal and crystal have phason strains equal to 0 and 1, respectively[29, 31].

Modeling Results and Discussion

We model the growth of quasicrystalline mesoporous silica nanoparticles as an irreversible aggregation of triangles and squares to reflect the relatively fast kinetics of the silica matrix formation[9]. As discussed, triangles are the result of surfactant micelle template sizes substantially larger than the mean of their size distribution. A survey of the parameters described above (see Computational Methods) yielded optimized conditions for assembly of quasicrystalline particles. Optimized simulations using an input triangle to square ratio of 2.3 to 1 ($S = 2.3$) consistently produced particles with dodecagonal quasicrystalline features (*i.e.* 12-fold symmetry and no translational periodicity), similar to quasicrystalline MSNs observed in experiments (Figure 5.1e). We characterized the quasicrystallinity of these particles by statistical analysis of an ensemble, because we are limited by our experimental model system to relatively small particle sizes[9]. Figure 5.3a shows the results of analyzing the phason coordinates of 400 simulated particles (see Tiling Analysis for details). Comparison of $R_g^{\perp}$ against $R_g^{\parallel}$ shows that structures collapse upon transformation and that the phason strain, calculated as the slope ($A = 0.09$) of the linear fit in Figure 5.3a, approaches that of an ideal quasicrystal ($A = 0$)[6, 30]. The inset in Figure 5.3a shows a typical tiling, where a 50 nm scale bar is defined using the average tile edge length measured from TEM images of MSNs.

To complete our description of this MSN growth model, we evaluated the effects of the imposed set of tiling rules on the quasicrystallinity of the assembled structures. As illustrated in Figure 5.2a, our model includes a shape specific interaction parameter (Tiling Rule 1) that penalizes edge-to-edge attachment of similar tiles (i.e. triangle to triangle attachment), except in cases where such attachments prevent defect formation. Similar interaction parameters have been widely utilized in 2-dimensional models of quasicrystal growth to prevent the formation of large cubic or hexagonal, crystalline domains[6, 17, 30]. The justification of such a parameter in the assembly of quasicrystalline mesoporous silica is the presence of repulsive interfacial interactions between the highest coordinated surfactant micelles in the triangle tiles[6, 32]. We analyzed the phason coordinates of an additional 400 simulations, performed without suppressing direct contact between similar shapes (i.e. without Tiling Rule 1) and using S = 2.3. Figure 5.3b shows a plot of $R_g^{\perp}$ against $R_g^{\parallel}$, demonstrating that these particles exhibit significantly increased phason strain (A = 0.28) as compared to those obtained using optimized simulation conditions (A = 0.09). Representative tilings, shown in the insets of Figures 5.3a and b, illustrate that the observed increase in quasicrystallinity arises from segregation of square and triangle tiles into crystalline domains.

We also included a growth rule that favors tile attachment at sites near the mass center of the existing tiling (Tiling Rule 2). The use of this surface minimizing condition is motivated by surface energy considerations that promote spherical rather than elongated MSN morphologies (Figure 5.1). As illustrated by representative tilings shown in the insets of Figures 5.3a and 3c, Tiling Rule 2 minimizes the formation of elongated structures, allowing us to reproduce the roughly spherical morphology of the quasicrystalline MSNs observed in experiment (Figure 5.1). Plots of $R_g^{\perp}$ against

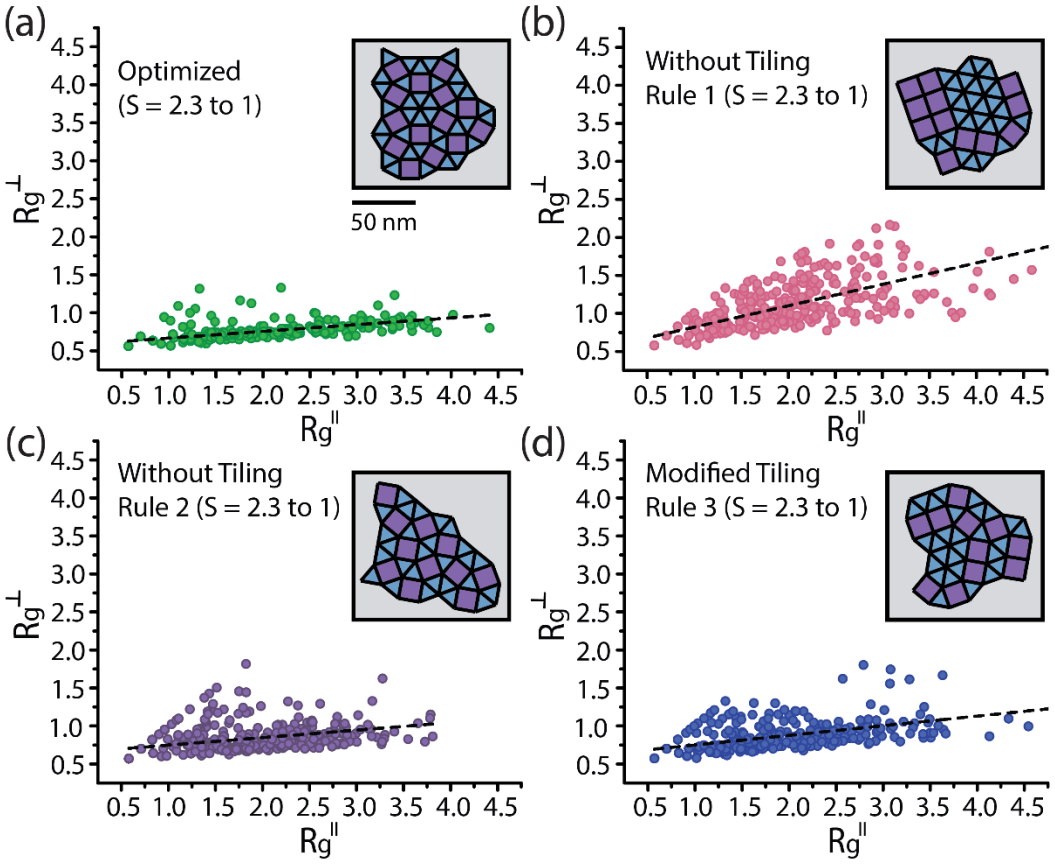

Figure 5.3. Plots of $R_g^{\perp}$ against $R_g^{\parallel}$ calculated for tilings produced using S = 2.3 and varying simulation conditions. Simulations were performed using (a) optimized conditions, (b, c) after removing Tiling Rules 1 and 2, and (d) using a modified version of Tiling Rule 3 that allows replacement site selection only. Dashed black lines in all plots denote linear fits. The insets in (a-d) show representative tilings, where the scale bar is defined using the tile edge length measured from TEM images of MSNs.

$R_g^{\parallel}$ in Figure 5.3 confirm that simulations performed with (Figure 5.3a) and without (Figure 5.3c) this growth rule yielded similarly low phason strains (A = 0.09 and 0.10, respectively).

In the absence of additional tiling rules, we observe the formation of packing defects, where growth sites remain unoccupied because attachment of either a triangle or a square would cause overlap with an already existing tile[28]. Since such defects are energetically unfavorable and only rarely observed in our experimental MSN system, we impose a mechanism that allows the system to avoid such defects by repeating its choices of both tile and attachment site (Tiling Rule 3). We also evaluated an alternate approach that allows replacement site selection only. Figure 5.3d shows a plot of $R_g^{\perp}$ against $R_g^{\parallel}$ calculated for structures using S = 2.3 and a modified threshold mechanism that allows repeated site selection only. Comparison to optimized simulations at S = 2.3 shows an increase in the calculated phason strain (A = 0.13) due to high frequency of packing defects (Figure D.1) and slightly increased sizes of triangle-only domains (inset in Figure 5.3d).

By changing the relative availability of triangles and squares in our simulations, we mimic the effects of increasing TMB concentration on MSN mesopore structure[9]. The wide range of structures observed in a single batch of MSNs synthesized at intermediate [TMB], including cubic (Figure 5.1c), mixed phase (Figure 5.1d), and quasicrystalline (Figure 5.1e) particles, could be reproduced by our model using S = 0.1 (Figure 5.4a)[9]. Figure 5.4a shows that the variety of structures observed in these simulations is reflected in a correspondingly wide distribution in $R_g^{\perp}$, where the crystalline and quasicrystalline extremes are illustrated using fits from optimized simulations using S = 0 and 2.3. The insets in Figure 5.4a show typical tilings obtained from this set of simulations. Additional simulations performed at S = 0.01 confirmed our expectation that primarily cubic particles are assembled under

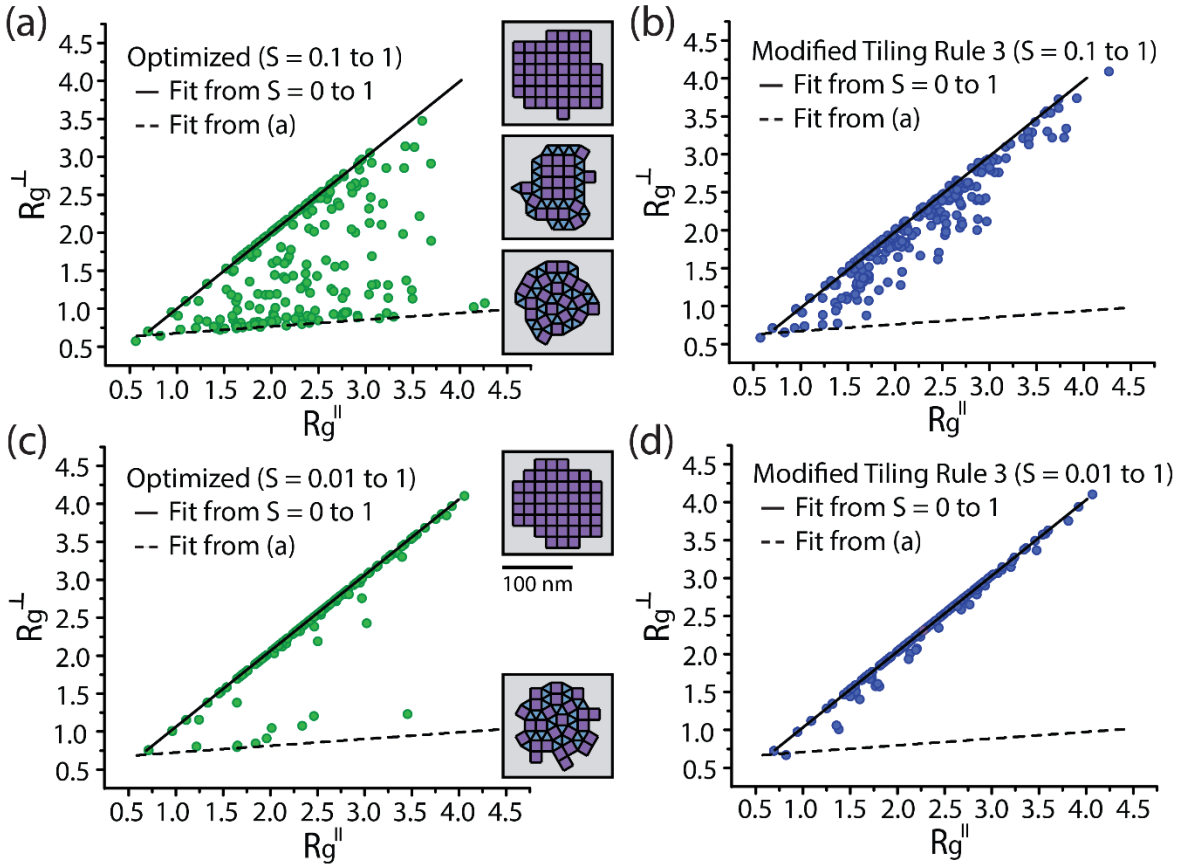

Figure 5.4. Plots of $R_g^{\perp}$ against $R_g^{\parallel}$ calculated for tilings produced using S = 0.1 (a, b) and 0.01 (c, d) and varying simulation conditions. Simulations were performed using (a, c) optimized conditions and (b, d) using a modified version of Tiling Rule 3 that allows replacement site selection only. Insets in (a) and (c) show representative tilings, where a scale bar is defined using the tile edge length measured from TEM images of MSNs. Solid and dashed lines denote fits obtained from optimized simulations using S = 0 and S = 2.3, respectively.

triangle-scarce growth conditions. Notably, as in MSN syntheses using low [TMB] (Figure 1c), we also observed a few quasicrystalline particles aside from the expected crystalline structures (Figure 5.4c)[9].

The growth rule (Tiling Rule 3) we introduced to prevent defect formation and reduce phason strain in simulations using S = 2.3 (Figure 5.3d) is also important for reproducing the variety of structures observed in experiments at intermediate and low [TMB] (S = 0.1 and 0.01). We again performed simulations in which we did not allow repeated tile selection to prevent defect formation. Figure 5.4b and d show plots of $R_g^{\perp}$ against $R_g^{\parallel}$ calculated for simulations that allowed repeated site selection only, using S = 0.1 and 0.01, respectively. While optimized simulations using S = 0.1 fluctuate widely in $R_g^{\perp}$, simulations performed using identical input parameters and this modified version of Tiling Rule 3 exhibit only a narrow range of structures. Similarly, no quasicrystalline particles are observed in simulations using S = 0.01 if repeated tile selection is excluded.

We begin to explain this difference by comparing the growth pathways of crystalline, mixed phase, and quasicrystalline particles, starting with a single square or triangle tile and using S = 0.1 (Figure 5.5). As illustrated in Figure 5.5, we observe that mixed phase structures form when the first triangle is late entering the growth pathway, attaching to an existing cubic, crystalline domain. In contrast, a first triangle appears early in the growth pathways of quasicrystalline particles. Comparison of representative particle growth pathways (Figure 5.5) suggests that even under triangle-scarce conditions (e.g. S = 0.1), the attachment of a first triangle seeds the growth of a quasicrystalline domain. Thus, in our optimized model system, the quasicrystallinity of an individual particle is largely determined by the time at which a first triangle is attached to the growing structure.

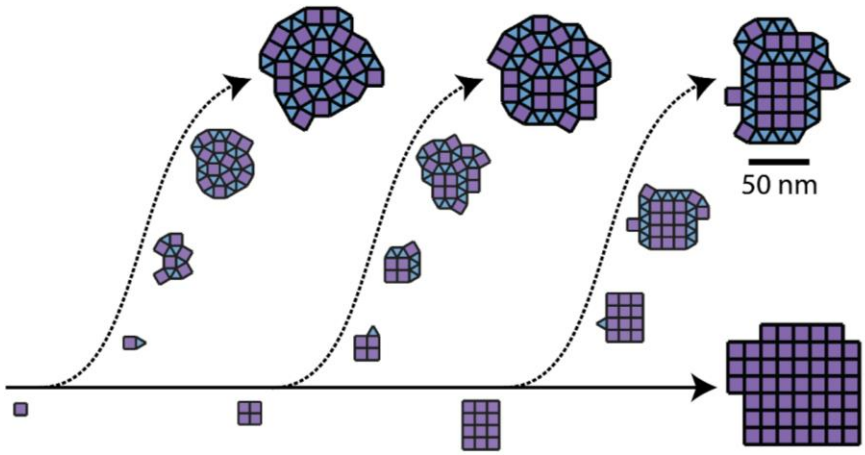

Figure 5.5. Representative particle growth trajectories from simulations using S = 0.1. A scale bar is defined using the tile edge length measured from TEM images of MSNs.

This behavior can be understood by considering the geometric constraints imposed by attaching a triangle to an otherwise cubic structure. As an example, we consider the attachment of a single triangle tile to a cubic structure with N = 4 (Figure 2c). As described in Figure 2, the triangle tile provides two attachment sites with high affinity for incoming square tiles, at least one of which belongs to a concave corner that may be completed only by triangles (*e.g.* 120º concave corner). If growth occurs under triangle-scarce conditions, one probable scenario is that the system will attempt to attach a square at this site. Since this move will generate a defect that cannot be filled by either a triangle or square (*i.e.* 30º concave corner), tile attachment will not occur. Instead the system will repeat its choice of tile and attachment site until a favorable move can be made, effectively increasing the probability of choosing a second triangle tile. We find that as a result of this defect suppression mechanism, the frequency of triangle attachment in simulations using $S = 0.1$ is substantially increased after a first triangle enters the assembly.

In real MSNs, triangle and square tiles are assembled from differently-sized micelles[9]. Thus, we approached our investigation of quasicrystal formation mechanisms by making an analogy between micelle polydispersity in the self-assembly of mesoporous silica and the availability of triangles relative to squares in an irreversible tiling model. In this experimental system, micelle rearrangements involving the entire assembly were ruled out due to the relatively fast kinetics of silica condensation[9, 28]. However, to assemble the variety of structures observed in experiment, we needed to allow geometric constraints imposed by the local environment to influence tile selection (Tiling Rule 3). This result implies that in the synthesis of quasicrystalline MSNs, local micelle rearrangements can occur before the structure is arrested by silica matrix formation. Our proposed mechanism is consistent with studies of micelle ordering in CTAB-directed MSN syntheses, where oriented

ellipsoidal micelles have been shown to undergo local alignment to form hexagonally-packed rods[33]. Although this relatively simple model does not address details of the micelle packing process, it reveals a general mechanism by which the involvement of polydisperse micelles may alter the growth pathway of a mesoporous silica nanoparticle.

Since our experimental study is limited to relatively small MSN sizes (N < 50), we performed additional simulations to investigate the continued growth of quasicrystalline seed structures (S = 2.3). Figure 6a shows a representative tiling with R = 25. To assess the quasicrystallinity of larger diameter tilings, we used a modified version of the analysis described above (see Methods), where phason strain is obtained from a single tiling rather than an ensemble. For a tiling with radius R, we define an origin r_0. $R_g^{\perp}$ and $R_g^{\parallel}$ were calculated for a series of concentric, circular areas with centers given by r_0 and radii (r) ranging from r_0 to R. As previously observed for smaller structures (Figure 3a), comparison of $R_g^{\perp}$ against $R_g^{\parallel}$ for simulations using S = 2.3 shows that patterns collapse upon transformation (Figure 6c). In this case, a phason strain value of 0.06 was obtained from the linear fit of a plot comparing $R_g^{\perp}$ against $R_g^{\parallel}$ (Figure 6c) for five, large diameter structures (R = 25).

Experimental studies of the continued growth of CTAB micelle-templated, quasicrystalline MSNs have not been reported, and thus our findings are presented here as a prediction. As observed in micron-sized mesoporous silica materials synthesized using an oppositely charged surfactant micelle[6], our simulated quasicrystals show a random mixture of triangle and square tiles in the particle core (white, dashed box in Figure 6a) with more periodic fans (alternating rows of triangles and squares) found in the periphery. Typical tilings from simulations *S* = 0.1 and 0.01 are shown in Figure D.2a and b, respectively. In all cases, irreversible tiling errors lead to the formation of large radial tears, in which tile edges remain

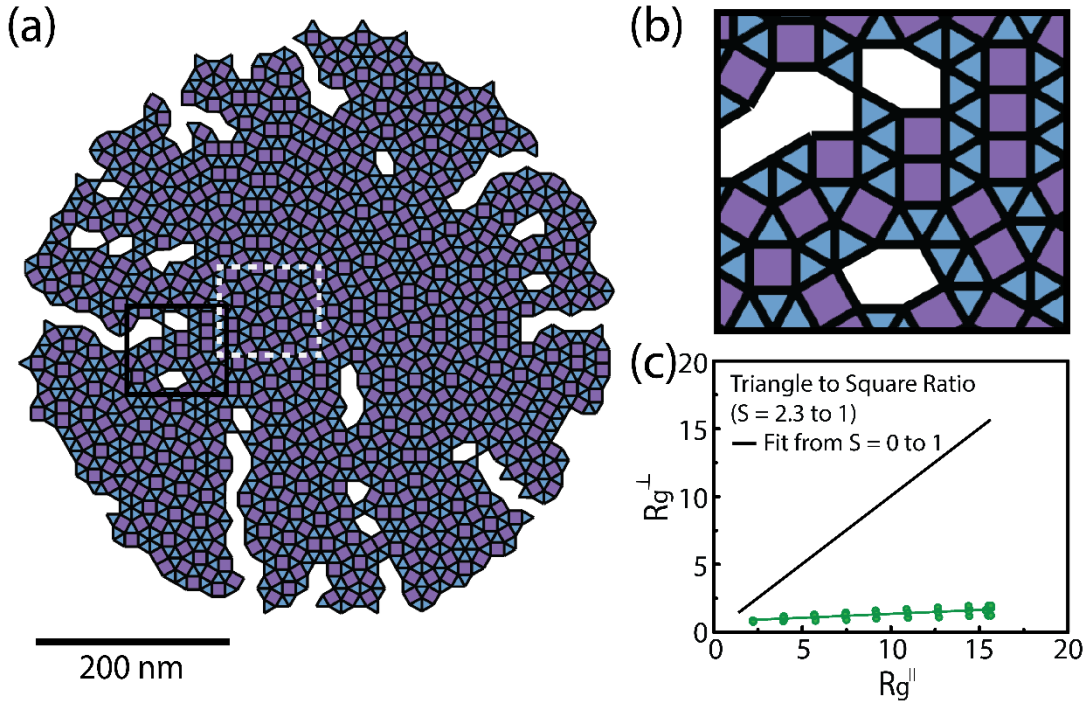

Figure 5.6. (a) Representative tiling with S = 2.3 and radius = 25 *d*. The particle core is marked in (a) using a white, dashed box. A scale bar is defined using the tile edge length measured from TEM images of MSNs. Examples of commonly observed defects are marked using a black box in (a) and shown magnified in (b). (c) Plot of $R_g^{\perp}$ against $R_g^{||}$ at various points during the growth of 5 tilings using S = 2.3.

unoccupied even as growth proceeds, because any new tile placed in the gap would overlap with an already existing tile[28]. These tears limit the long-range order in quasicrystals assembled using our growth model (Figure 6a), but we note that the most commonly observed defects (*i.e.* unoccupied, 6-sided polygons in Figure 6b) are also frequently observed by C. Xiao *et al.* in quasicrystalline mesoporous silica[6].

Conclusions

In this article, we have given a full account of recent experimental and theoretical investigations of the growth of surfactant micelle-directed quasicrystalline mesoporous silica in the form of nanoparticles. Comparing different moments of the experimentally determined asymmetric micelle size distributions we first revealed sensitivity of the quasicrystal formation particularly to the higher order moments of these distributions. Then, using an irreversible, square-triangle tiling model, we showed that increasing the availability of triangles relative to squares in our simulations mimicked the effects of these increasingly asymmetric micelle size distributions on MSN structures[9]. Our study describes a set of simple, geometric tiling rules that can be used to reproduce the experimentally observed crystal to quasicrystal transition.

We have shown that the quasicrystallinity of our simulated particles is improved by a shape-specific parameter that penalizes edge-to-edge attachment of similar tiles. We have also demonstrated that the roughly spherical morphology of experimentally observed MSNs is successfully reproduced in our model by a surface minimizing parameter. Our results demonstrate that the variety of structures observed experimentally is accessible using our growth model, only if geometric constraints imposed by the local environment are allowed to influence the availability of triangles relative to squares. By analyzing the growth pathways of individual particles, we have

also shown that quasicrystallinity is dictated by the time at which a triangle joins the assembly. Our results imply that although micelle mobility is limited by the relatively fast kinetics of silica formation in our MSN system, local micelle rearrangements play a critical role in quasicrystal formation.

Finally, we have shown that the continued growth of our simulated particles yields quasicrystals similar to those observed experimentally in micron-sized mesoporous silica materials. Although the mechanism described here is complicated by cooperative interactions between micelles and silica species[13], parallels may exist in other quasicrystal-forming soft materials, where rapid cooling steps produce kinetically trapped micelle clusters[3]. Additionally, our results may be extended to the self-assembly of 2-dimensional, patchy nanoplates, which have already been shown to form a variety of Archimedian tilings[34]. In the future, our simple model may be expanded to include molecular details that facilitate more direct comparison to quasicrystal-forming materials systems.

REFERENCES

1. Shechtman, D.; Blech, I.; Gratias, D.; Cahn, J. Metallic Phase with Long-Range Orientational Order and No Translational Symmetry. *Phys. Rev. Lett.* **1984**, *53*, 1951-1953.

2. Zhang, J.; Bates F. S. Dodecagonal quasicrystalline morphology in a poly(styrene-b-isoprene-b-styrene-b-ethylene oxide) tetrablock terpolymer. *J. Am. Chem. Soc.* **2012,** *134*, 7636-7639.

3. Gillard, T.M.; Lee, S.; Bates, F.S. Dodecagonal quasicrystalline order in diblock copolymer melt. *PNAS* **2016**, *113,* 5167 – 5172.

4. Zeng, X.; Ungar, G.; Lui, Y.; Percec, V.; Dulcey, A. E.; Hobbs, J. K. Supramolecular dendritic liquid quasicrystals. *Nature* **2004**, *428,* 157-160.

5. Hayashida, K.; Dotera, T.; Takano, A.; Matsushita, Y. Polymeric Quasicrystal: Mesoscopic Quasicrystalline Tiling in A B C Star Polymers. *Phys. Rev. Lett.* **2007,** *98,* 195502.

6. Xiao, C.; Fujita, N.; Miyasaka, K.; Sakamoto, Y.; Terasaki, O. Dodecagonal tiling in mesoporous silica. *Nature* **2012,** *487,* 349-353.

7. Gao, C.; Sakamoto, Y.; Terasaki, O.; Che, S. Formation of diverse mesophases templated by a diprotic anionic surfactant. *Chem. Eur. J.* **2008,** *14,* 11423 – 11428.

8. Suteewong, T.; Sai, H.; Cohen, R.; Wang, S.; Bradbury, M., Baird, B.; Gruner, S. M.; Wiesner, U. Highly Aminated Mesoporous Silica Nanoparticles with Cubic Pore Structure. *J. Am. Chem. Soc.* **2011,** *133,* 172-175.

9. Sun, Y.; Ma, Kai.; Kao, T.; Spoth, K.A.; Sai, H.; Zhang, D.; Kourtoutis, L.F.; Elser, V.; Wiesner, U. Formation pathways of mesoporous silica nanoparticles with dodecagonal tiling. *Nat. Commun.* **2017**, *8*, 252.

10. Iacovella, C.R.; Keys, A.S.; Glotzer, S.C.; Self-assembly of soft-matter quasicrystals and their approximants, *PNAS* **2011,** *108,* 20935 – 20940.

11. Yue, K.; Huang, M.; Marson R.L.; He, J.; Huang, J.; Zhou Z.; Wang, J.; Liu C.; Yan, X.; Wu, Kan.; *et al.* Geometry induced sequence of nanoscale Frank-Kasper and quasicrystal mesophases in giant surfactants. *PNAS* **2016,** *113,* 14195 – 14200.

12. Nagao, K; Inuzuka, T.; Nishimoto, K.; Edagawa, K. Experimental Observation of Quasicrystal Growth. *Phys. Rev. Lett.* **2015,** *115,* 075501.

13. Firouzi, A.; Kumar, D.; Bull, L. M.; Besier, T.; Sieger, P.; Huo, Q.; Walker, S.A.; Zasadzinski, J. A.; Glinka, C.; Nicol, J.; *et al.* Cooperative organization of inorganic-surfactant and biomimetic assemblies. *Science* **1995,** *267,* 1138-1143.

14. Yanagisawa, T.; Shimizu, K.; Kuroda, K.; Kato, C. The preparation of alkyltrimethylammonium-kanemite complexes and their conversion to microporous materials. *Bull. Chem. Soc. Jpn.* **1990,** *63,* 988-992.

15. Kresge, C.; Leonowicz, M.; Roth, W.; Vartuli, J.; Beck, J. Ordered mesoporous molecular sieves synthesized by a liquid-crystal template mechanism. *Nature* **1992,** *359,* 710-712.

16. Ma, K.; Sai, H.; Wiesner, U. Ultrasmall Sub-10 nm Near-Infrared Fluorescent Mesoporous Silica Nanoparticles. *J. Am. Chem. Soc.* **2012,** *134,* 13180-13183.

17. Kuo, K. H.; Feng, Y. C.; Chen, H. Growth Model of Dodecagonal Quasicrystal Based on Correlated Tiling of Squares and Equilateral Triangles. *Phys. Rev. Lett.* **1975,** *34,* 1740 – 1743.

18. van der Linden, M. N.; Doye, J. P. K.; Louis, A. A. Formation of dodecagonal quasicrystals in two-dimensional systems of patchy particles. *J. Chem. Phys.* **2012**, *136*, 054904.

19. Kelley, E.G.; Murphy R. P.; Seppala, J. E.; Smart, T. P.; Hann, S. D.; Sullivan, M. O.; Epps, T. H. Size evolution of highly amphiphilic macromolecular solution assemblies via a distinct bimodal pathway. *Nat. Commun.* **2014,** *5,* 3599.

20. Espenscheid, W. F.; Kerker, M.; Matijevic E.; Logarithmic Distribution Functions for Colloidal Particles. *J. Phys. Chem.* **1964**, *68*, 3093 – 3097.

21. Limpert, E.; Stahel, W. A.; Abbt, M.; Log-normal Distributions across the Sciences: Keys and Clues. *BioScience.* **2001**, *51*, 341 – 352.

22. Israelachvilli, J. *Intermolecular and Surface Forces;* Academic Press: New York, **1991**.

23. DeCarlo, L. T. On the meaning and use of kurtosis. *Psychol. Meth.* **1997**, *2*, 292 – 307.

24. Ogarko, V.; Luding, S. Prediction of polydisperse hard-sphere mixture behavior using tridisperse systems. *Soft Matter* **2013,** *9*, 9530-9534.

25. Wiesner, U.; Schmidt-Rohr, K.; Boeffel, C.; Pawelzik, U.; Spiess, H. W. Solid-State ^{13}C-NMR on Oriented Films of Liquid-Crystalline Polymers. *Adv. Mat.* **1990,** *2*, 484-487.

26. Patel, A. J.; Garde, S.; Efficient Method to Characterize the Context-Dependent Hydrophobicity of Proteins. *J. Phys. Chem. B* **2014,** *118*, 1564-1573.

27. Oxborrow, M.; Henley, C. Random square-triangle tilings: A model for twelvefold-symmetric quasicrystals. *Phys Rev B* **1993**, *48*, 6966-6998.

28. Joseph, D.; Elser, V. A Model of Quasicrystal Growth. *Phys. Rev. Lett.* **1997,** *79*, 1066 – 1069.

29. Frank, F. C.; Kasper, J. S. Complex alloy structures regarded as sphere packings. II. Analysis and classification of representative structures. *Acta Crystallogr.* **1959,** *12*, 483 – 499.

30. Rubinstein, B.; Ben-Abraham, S. I. The 'random' square-triangle tiling: simulation of growth. *Mater. Sci. Eng. A* **2000,** *296*, 418 – 420.

31. Stampfli, P. A dodecagonal quasiperiodic lattice in two dimensions. *Helv. Phys. Acta* **1986**, *59*, 1260-1263.

32. Ziherl, P.; Kamien, R. D. Maximizing Entropy by Minimizing Area: Towards a New Principle of Self-Organization. *J. Phys. Chem. B* **2001,** *105*, 10147 – 10158.

33. Sadasivan, S.; Fowler, C. E.; Khushalani, D.; Mann, S. Nucleation of MCM-41 Nanoparticles by Internal Reorganization of Disordered and Nematic-Like Silica-Surfactant Clusters. *Angew. Chem. Int. Ed.* **2002,** *41*, 2151-2153.

34. Millan, J. A.; Ortiz, D.; van Anders, G.; Glotzer, S. C. Self-Assembly of Archimedian Tilings with Enthalpically and Entropically Patchy Polygons. *ACS Nano*, **2014**, *8*, 2918 – 2928.

CHAPTER 6

CONCLUSIONS

In this dissertation, I have explored the design, synthesis, and characterization of two silica nanoparticle systems: an intensity-based fluorescent silica nanoparticle barcode (Chapters 2 and 3) and a quasicrystal-forming mesoporous silica nanoparticle system (Chapters 4 and 5).

In Chapters 2 and 3, a batch synthesis platform for fluorescent silica nanoparticles with controlled intensity levels was developed. Optimized intensity distributions as mapped by single-particle fluorescence microscopy were achieved using a seeded growth approach to minimize the formation of low dye-loaded secondary particles. Variations of the organosilane linker were also introduced to maximize the dye incorporation efficiency. As a first example, fluorescent Cy3 dye was employed to generate a single-color fluorescent intensity barcode. High and low dye-loaded fluorescent silica nanoparticles were unambiguously distinguishable in single-particle fluorescence images.

These results may be generalized to a range of spectrally distinct dyes. Combinatorial labeling using spectrally distinct dyes at different intensity levels could be used to extend this platform and generate large numbers of distinguishable probes. For example, a series of 27 optical codes could be generated by using 3 different colors and 3 different intensity levels (e.g. zero, low, and high). Due to the tunability of the silica chemistry, this system is ideal for developing multi-color fluorescent probes. The controlled silica shell growth introduced here could be used to separate spectrally distinct fluorescent dyes, preventing energy transfer between dyes, while further surface functionalization of the particles could be used to target probes e.g. to specific desired locations within a cell.

In Chapters 4 and 5, a model system for investigation of quasicrystal formation mechanisms was developed. An irreversible micelle packing mechanism was proposed to account for the fast condensation of silica in this system. Control of the silica chemistry enabled direct comparison of experimental and simulated quasicrystal growth pathways down to a single tiling unit. Continued growth of simulated quasicrystalline MSNs yields quasicrystals similar to those observed experimentally in micron-sized mesoporous silica materials[1]. The results demonstrated in Chapters 4 and 5 indicate that size dispersity of the surfactant micelle building blocks triggers the growth of quasicrystalline mesoporous silica.

The quasicrystal growth mechanism described in Chapters 4 and 5 is facilitated by electrostatic interactions between positively charged surfactant micelles and negatively charged silica precursors. Moreover, the fast formation of silica in this system may find parallels in the rapid cooling steps commonly used during fabrication of quasicrystals in other soft materials systems[2]. Finally, the easily accessible experimental control parameters identified in this work, i.e. micelle size heterogeneity as induced by increasing amounts of pore expander or increasing stirring rates, may be translated to the design of alternate quasicrystal-forming materials systems. In the future, the specific growth model used to describe the experimental findings may also be expanded beyond simple phenomenological approaches and include approaches directly mapped on physical laws associated with molecular parameters, thereby providing further insight into quasicrystal-forming materials systems.

REFERENCES

1. Xiao, C.; Fujita, N.; Miyasaka, K.; Sakamoto, Y.; Terasaki, O. Dodecagonal tiling in mesoporous silica. *Nature* **2012,** *487,* 349-353.

2. Gillard, T.M.; Lee, S.; Bates, F.S. Dodecagonal quasicrystalline order in diblock copolymer melt. *PNAS* **2016**, *113,* 5167 – 5172.

APPENDIX A

SUPPORTING INFORMATION FOR CHAPTER 2

Materials

Tetraethyl orthosilicate (TEOS, ≥99%), l-arginine (≥99%), ammonium hydroxide (NH4OH, 29%), isopropanol (anhydrous, 99.5%), ethanol (absolute, anhydrous), and dimethyl sulfoxide (DMSO) were purchased from Sigma Aldrich. N-(2-aminoethyl)-3-aminopropyltrimethoxysilane (AEAPTMS, 95%), 3-aminopropyltrimethoxysilane (APTES, ≥97%), 3-mercaptopropyltrimethoxysilane (MPTMS, ≥96%), and methoxy-terminated poly(ethylene glycol) chains (PEG-silane, molar mass of ~500 g/mol) were purchased from Gelest Inc. Phosphate buffered saline (PBS, sterile) was purchased from Amresco Inc. Cy3 NHS ester was purchased from GE Healthcare. α,ω-Heterobifunctional PEGs with maleimide and biotin groups (mal-PEG-biotin, molar mass of ~922 g/mol) were purchased from Quanta BioDesign Inc. Streptavidin and N-γ-maleimidobutyryl-oxysuccinimide ester (GMBS) were purchased from Life Technologies. All chemicals were used as received without further purification. Deionized water (Milli-Q, 18.2 MΩ·cm) was used throughout. 20 mL borosilicate scintillation vials, purchased from DWK Life Sciences, and 4 mm x 12.7 mm PTFE coated stir bars, purchased from Fisher Scientific, were used for all particle syntheses. 35 mm glass bottom dishes purchased from Mattek Corporation (No. 1.5 coverslip, 20 mm glass diameter) were used in all imaging experiments.

Synthesis of Fluorescent SNPs by Homogenous Growth

Cy3/APTES conjugate was prepared by reacting Cy3 NHS ester with a 10-fold excess of APTES in DMSO overnight under an inert nitrogen environment. In a typical synthesis, l-arginine (0.012 g) was dissolved in deionized water (9.32 mL), stirring slowly (150 rpm) in a 20 mL scintillation vial at 60°C. Use of l-arginine

resulted in an initial pH of 9.2. The Cy3/APTES conjugate was added dropwise into the stirring solution at varying concentrations (1.3 μM or 24.0 μM). Then, TEOS (135 μL) was added slowly in a thin layer to the top surface of the aqueous reaction medium. The resulting mixture was stirred for 8 hrs. An additional 3 TEOS (135 μL) additions to the top surface were made in 8 hr increments. The reaction was left stirring (150 rpm) for 24 hrs after the final TEOS addition.

Synthesis of Fluorescent SNPs by Seeded Growth

To synthesize seed particles, l-arginine (0.012 g) was dissolved in deionized water (9.32 mL), stirring slowly (150 rpm) in a 20 mL scintillation vial at 60°C. Use of l-arginine resulted in an initial pH of 9.2. TEOS (135 μL) was added slowly in a thin layer to the top surface of the aqueous reaction medium. The resulting mixture was stirred for 8 hrs. An additional 4 TEOS (3x135 μL and 1x143.5 μL) additions were made to the top surface in 8 hr increments. The reaction was left stirring (150 rpm) for 24 hrs after the final TEOS addition.

In a typical seeded growth, Cy3/AEAPTMS conjugate was prepared by reacting Cy3 NHS ester with a 10-fold excess of AEAPTMS in DMSO overnight under an inert nitrogen environment. Then, 2 mL of seed particles was added to 8 mL of deionized water stirring slowly (150 rpm) in a 20 mL scintillation vial at 60°C. Cy3/AEAPTMS conjugate was added dropwise into the stirring solution. The concentration of Cy3 was varied from 6.0 μM to 30.0 μM. TEOS (143.5 μL) was added slowly in a thin layer to the top surface of the reaction. The resulting mixture was stirred (150 rpm) for 24 hrs. One additional TEOS (143.5 μL) addition to the top surface was made after 24 hrs.

PEGylation of Fluorescent SNPs

Biotin-PEG-silane was prepared by reacting mal-PEG-biotin (100 mg/mL in DMSO) with 1.1 equivalents of MPTMS in DMSO overnight under an inert nitrogen environment. Native solutions of SNPs were diluted 5 times in deionized water. The pH of the solution was increased to 10 using NH_4OH. A mixture of PEG-silane (100 μL) and silane-PEG-biotin (12.5 μL) was added dropwise to the stirring solution (600 rpm), which was left stirring overnight. In the next step, the temperature was increased to 80°C and the stirring was stopped. PEGylation was completed after 12 hrs at 80°C.

TIRF Substrate Preparation

Glass bottom dishes were functionalized using a previously established protocol with slight modifications[1]. Glass dishes were rinsed successively with isopropanol and deionized water. Substrates were then dried using nitrogen and plasma cleaned for 10 minutes using a Harrick Plasma Generator (PDC32G) operated at high power. As illustrated in Figure 2b, each dish was covered and incubated with 500 μL of a 0.2M solution of MPTMS in ethanol for 30 minutes, before rinsing several times with ethanol. The silanized slide was activated for streptavidin attachment by incubation with 250 μL of 4 mM GMBS in ethanol for 30 minutes (Figure 2.2b). The GMBS had been dissolved in DMSO at 1M before dilution in ethanol. The substrate was rinsed several times with ethanol and then rinsed again using PBS buffer. 100 μL of streptavidin (50 μg/mL) was immobilized on the surface of the GMBS-activated glass by incubation for 2 hours. Finally, the substrate was rinsed several times using PBS. Substrates were used immediately or stored in PBS at 4°C.

Characterization

Gel permeation chromatography (GPC) purification was performed using a BioLogic LP system equipped with a 275 nm UV detector and using Sephacryl 400 resin from GE Healthcare, as previously described for PEGylated SNPs[2]. As expected, 3 peaks were observed in GPC elugrams of SNPs and were attributed to aggregated SNPs, individual SNPs, and free reactants (black arrows in Figures A.1 and A.4e), as described in reference (2). Narrowed size distributions were achieved by collecting a fraction of the SNP peak (blue in Figures A.1 and A.4e).

Transmission electron microscopy (TEM) images were taken using a FEI Tecnai T12 Spirit microscope operated at an acceleration voltage of 120 kV. TEM grids were prepared by drop casting from native synthesis solution prior to PEGylation. Particle diameters (Figures A.1 and A.4d) were obtained from TEM images using the automated particle detection feature of the ImageJ image analysis software (version 1.50i).

Absorption and emission spectra were measured using a Varian Cary Model 5000 spectrophotometer and Photon Technologies International Quantamaster spectrofluorometer, respectively. Intrinsic scattering from SNPs was estimated by fitting the absorbance from 350 – 450 nm, a region of the spectra which is not affected by Cy3 absorbance, and subtracted from the excitation spectra of fluorescent SNPs (*3*).

Fluorescence correlation spectroscopy (FCS) measurements were conducted using a home-built FCS setup. A 543 nm HeNe laser was used as a laser source for the Cy3 fluorophore. The hydrodynamic size, brightness per particle, and particle concentration were obtained from fits of the FCS autocorrelation curves for single component diffusion as described elsewhere[4, 5, 6].

Fluorescence imaging was performed using an inverted Zeiss Elyra microscope operated in total internal reflection fluorescence (TIRF) geometry. A 1.46 NA 100X

objective was used for illumination and light collection. Fluorescent signal was filtered using a 570 - 620 nm band pass filter. A 543 nm laser (4.2 mW laser power, measured at the objective) was used as an excitation source for the Cy3 fluorophore. Imaging conditions were optimized to minimize deviations in excitation power, image focus, and photobleaching, resulting in reproducible single particle intensity distributions[7]. For each imaging experiment, a series of 50 images (100 ms/frame) was acquired, beginning just before the excitation laser was turned on. Images acquired before the laser power stabilized (~700 ms) were discarded and intensity analysis was performed on the first image of the remaining stack. "Definite focus" focal-drift compensation was used during image acquisition. Biotinylated SNPs were attached to streptavidin coated slides by incubation for several minutes before rinsing with PBS to remove free SNPs. All imaging experiments were performed in PBS.

Intensity Analysis

Spot detection and subsequent spot intensity analyses were performed using a home-built MATLAB program[8]. Spot detection was performed inside a 256 x 256 pixel^2 area to minimize deviations in excitation power and image focus (green dashed box line in Figure A.2a). For individual SNPs, we expect that peak pixel intensity (I_{Peak} in Figure A.2b) and spot area increase with particle brightness[8]. However, we observed widely varying spot areas for low intensity substrate contaminants, which were occasionally found on streptavidin-coated substrates (Figure A.3). We have therefore used I_{Peak} as an area-independent metric for spot identification. Specifically, spots with I_{Peak} above a threshold value ($I_{Threshold}$) were centered in a 17 x 17 pixel^2 region of interest (ROI). As illustrated in Figures A.3c and d, $I_{Threshold}$ was increased to reduce false positive identification of low intensity contaminants. However, at high $I_{Threshold}$ values, increasing numbers of low intensity SNPs were also excluded from

analysis. For this reason, $I_{Threshold}$ was kept between 0 and 7500. $I_{Threshold}$ was optimized and held constant for all experiments performed using a particular batch of substrates. For this reason, only imaging experiments performed using the same batch of substrates were compared directly. As an example, a discarded spot with I_{Peak} below $I_{Threshold}$, is highlighted in red in Figure S2a and shown magnified in the inset on the right side for clarity. Spots identified for intensity analysis ($I_{Peak} > I_{Threshold}$) are bounded in white (Figure A.2a). Figure A.2b shows the intensity profiles of a representative spot in the x- and y- directions. The background level and full width at half maximum (FWHM) were determined from Gaussian fits centered on I_{Peak} in the x- and y- directions (Figure A.2b). Spot intensity was calculated as the background-corrected sum over all pixels inside an approximately circular area, defined using $FWHM_x$ and $FWHM_y$ as the x- and y-axis lengths of an ellipse[8]. A single background value was calculated by averaging background signals determined from the x- and y-spot intensity profiles (Figure A.2b). To avoid errors in defining background signal, the ROI size was optimized to accommodate the entire spot intensity profile. Since the background level was determined from the tails of Gaussian fits to the spot intensity profile, small ROIs resulted in artificially inflated background signals and correspondingly low apparent intensities for large spots.

We applied additional selection rules to exclude ROIs containing multiple SNPs from analysis. Assuming that the point spread function (PSF) of a single SNP is approximately symmetric[9], we attributed large deviations to overlap of multiple nanoparticle PSFs (Figure A.2a). Spots were therefore rejected if the FWHMs of Gaussian fits in the x- and y-direction were unequal beyond a 5% tolerance (orange). Spots were also rejected if ROIs overlapped with the boundary of the area of analysis (green) or with another ROI (blue) to minimize associated errors. Examples are again

highlighted in the image in Figure A.2a and magnified in the insets on the right side of the figure.

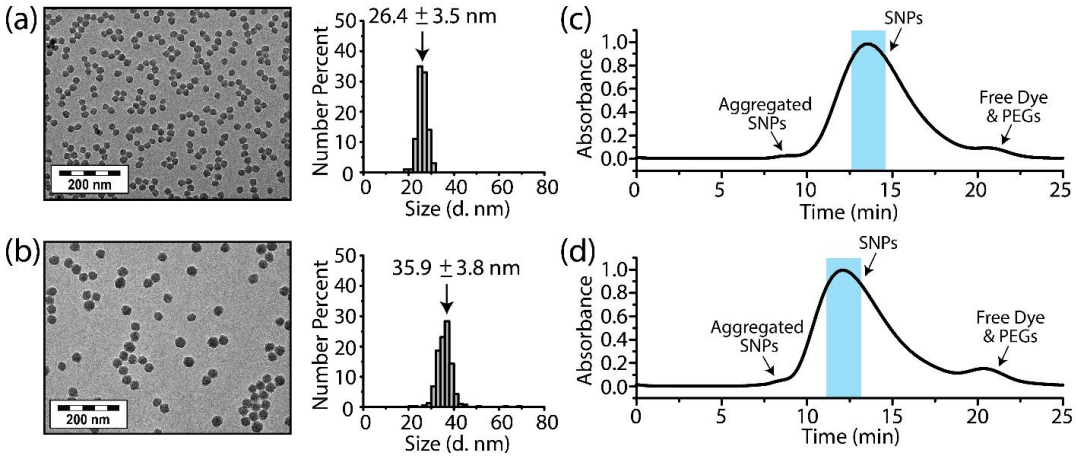

Figure A.1. Characterization of SNPs synthesized by homogenous growth. (a, b) TEM images of SNPs prepared using (a) 1.3 μM Cy3/APTES or (b) 24.0 μM Cy3/APTES prior to PEGylation and corresponding image based size analysis. (c, d) GPC elugram of PEGylated SNPs prepared using (c) 1.3 μM Cy3/APTES or (d) 24.0 μM Cy3/APTES. Native solutions contained aggregated SNPs, SNPs, and free reactants (black arrows). Narrowed size distributions were achieved by collecting only a fraction of the SNP peak (blue).

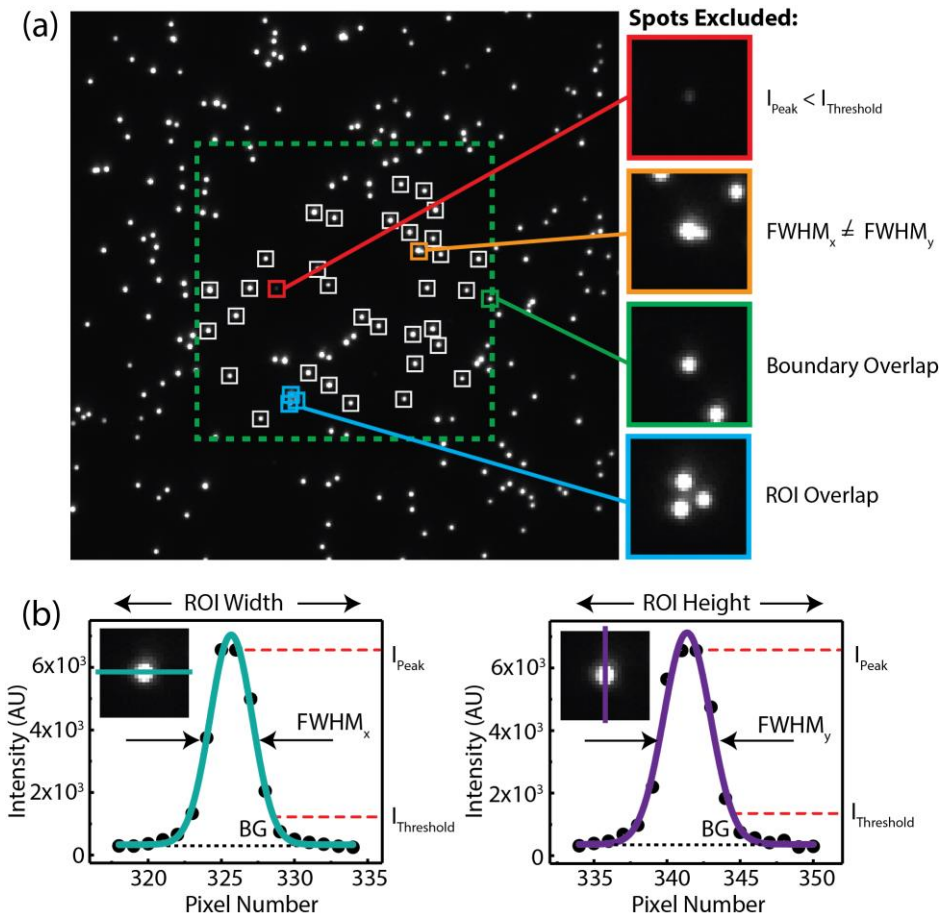

Figure A.2. Spot detection and intensity analysis. (a) A typical fluorescence image of Cy3-loaded SNPs acquired using TIRF microscopy. Spot detection was performed inside a 256 x 256 pixel^2 area (green dashed box). Spots with peak intensity (I_{Peak}) above a threshold value ($I_{Threshold}$) were centered in a 17 x 17 pixel^2 region of interest (ROI). As an example, a discarded spot, with I_{Peak} below $I_{Threshold}$, is highlighted in red and shown magnified in the inset for clarity. Spots arising from overlap of multiple nanoparticles were rejected if the FWHMs of Gaussian fits in the x- and y-direction deviated by more than 5% (orange box). Spots were also rejected if ROIs overlapped with the boundary of the area of analysis (green box) or with another ROI (blue box). Examples are highlighted in the image and magnified in the inset. Spots identified for intensity analysis are bounded in white. (b) Intensity profiles of a representative spot in the x- and y- directions. Gaussian fits are shown in teal and purple, respectively. The positions of the profiles are marked in the inset images. I_{Peak} and $I_{Threshold}$ are marked using red dashed lines. Background signal is determined from the Gaussian fit and marked in the plots using black dotted lines. Spot intensity is calculated as the background-corrected sum over all pixels inside the FWHM.

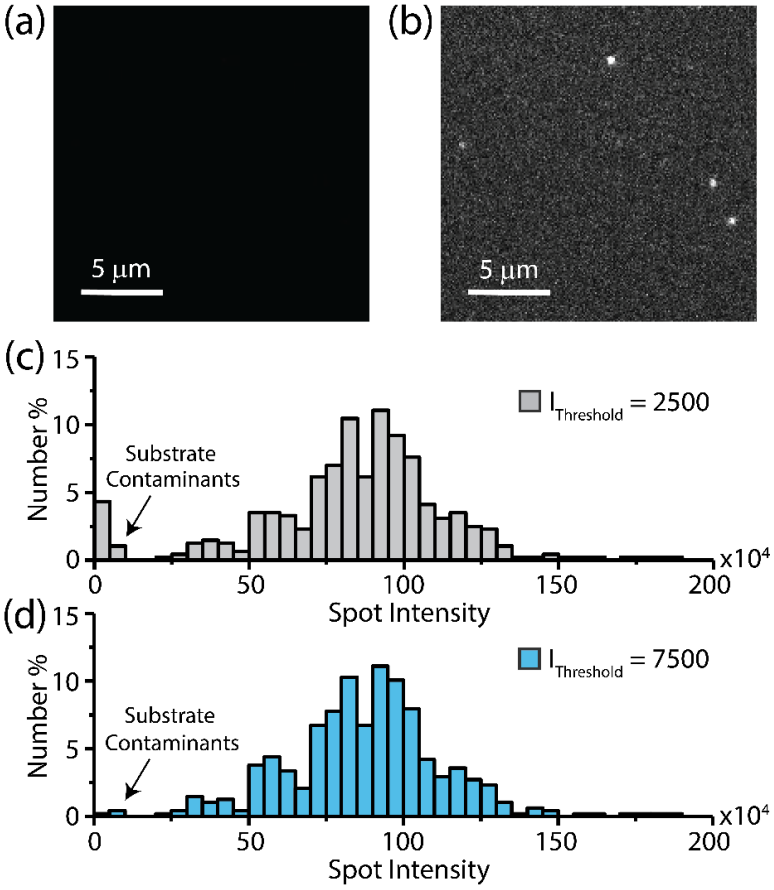

Figure A.3. Substrate background and intensity threshold. (a) A fluorescence image of a streptavidin-coated glass substrate, taken before biotinylated SNPs were added. (b) A contrast-enhanced version of the image shown in (a), highlighting low intensity spots that result from substrate contamination. (c, d) Spot intensity distributions resulting from images of Cy3-loaded SNPs using (c) low and (d) high values for $I_{Threshold}$. Spot intensity was calculated as the background-corrected sum over all pixels within the FWHM. However, we have used the peak pixel intensity (I_{Peak}) as a spot area-independent metric for spot identification. Spots are selected for analysis if $I_{Peak} > I_{Threshold}$. In experiments performed using this set of substrates, $I_{Threshold} = 7500$ was chosen to reduce false positive identification of fluorescent substrate contaminants (black arrows). $I_{Threshold}$ was not increased beyond this value, because increasing numbers of low intensity SNPs would also be excluded from analysis. SNPs used for this analysis were synthesized by seeded growth, using 24.0 μM Cy3/AEAPTMS.

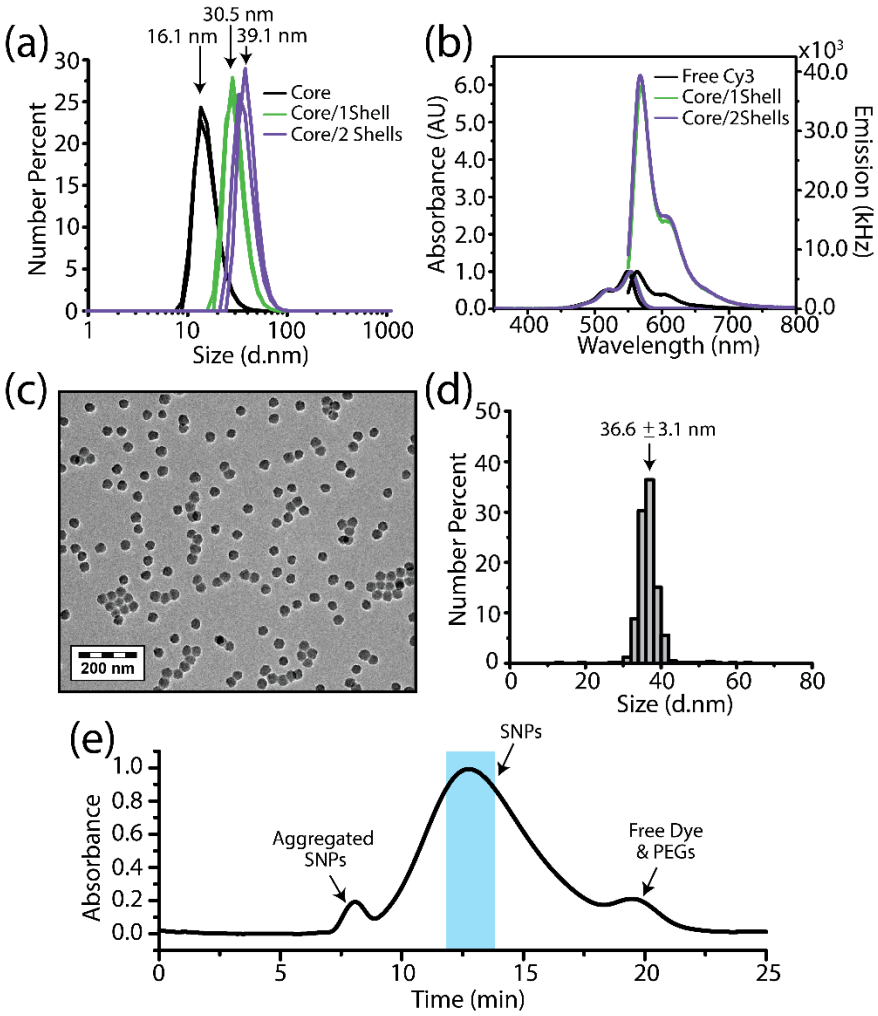

Figure A.4. Characterization of nanoparticle intermediates during seeded growth, using 24.0 μM Cy3/AEAPTMS. (a) DLS derived size distributions of blank SNP cores and Cy3-labeled SNPs with one or two shells added. DLS measurements were taken prior to PEGylation. (b) Normalized absorption and emission spectra for free Cy3 dye and Cy3-labeled SNPs with one or two shells added, following PEGylation and subsequent GPC purification. (c, d) TEM image of final two-shell Cy3-labeled SNPs, prior to PEGylation, and corresponding image based size analysis. (e) GPC elugram of PEGylated, two-shell Cy3-labeled SNPs. Native solutions contain aggregated SNPs, SNPs, and free reactants (black arrows). Narrowed size distributions were achieved by collecting only a fraction of the SNP peak (blue).

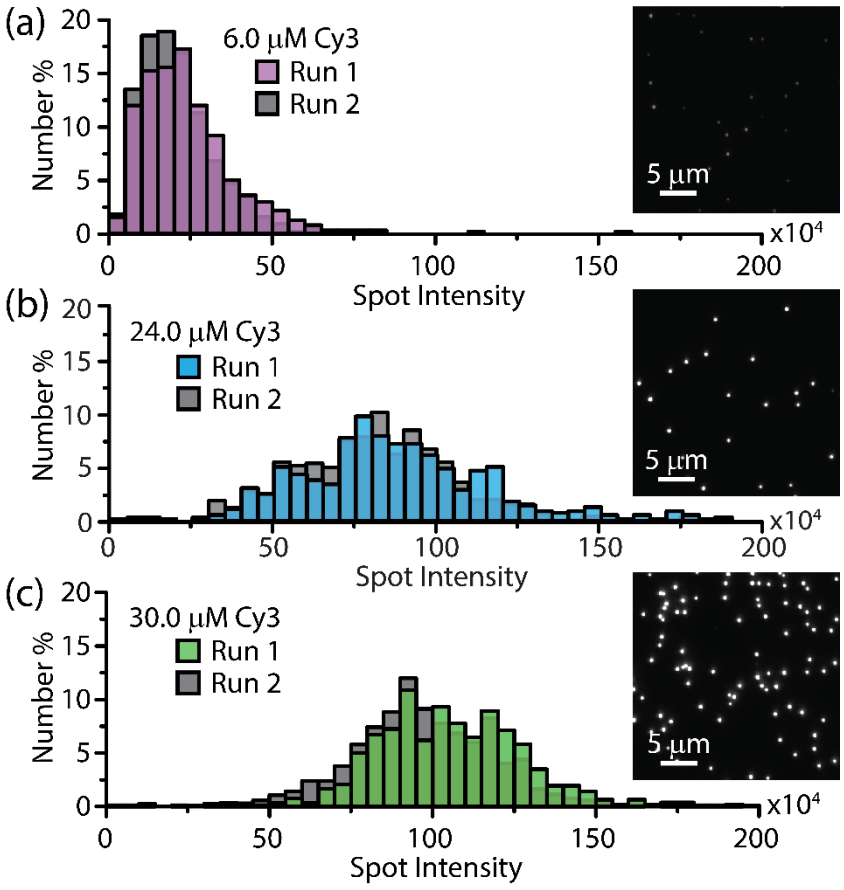

Figure A.5. Intensity distributions for SNPs synthesized using seeded growth and (a) 6.0 μM, (b) 24.0 μM, or (c) 30.0 μM Cy3/AEAPTMS. Distributions for SNPs obtained from two independent syntheses under the same conditions are superimposed (gray) to demonstrate reproducibility of the approach. Insets show the corresponding TIRF images.

REFERENCES

1. Ngundi, M. M.; Shriver-Lake, L. C.; Moore, M. H.; Lassman, M. E.; Ligler, F. S.; Taitt, C. R. *Anal. Chem.* **2005**, *77*, 148 – 154.
2. Ma, K.; Mendoza, C.; Werner-Zwanziger, U.; Zwanziger, J.; Wiesner, U. *Chem. Mater.* **2015**, *27*, 4119 – 4133.
3. Ruiz, A. E.; Caregnato, P.; Arce, V. B.; Schiavoni, M. M.; Mora, V. C.; Gonzalez, M. C.; Allegretti, P. E.; Martire, D. O. *J. Phys. Chem. C.* **2007**, *111*, 7623 – 7628.
4. Ow, H.; Larson, D.; Srivastava, M.; Baird, B., Webb, W.; Wiesner U. *Nano Lett.* **2005**, *5*, 113 - 117.
5. Larson, D. R.; Ow, H.; Vishwasrao, H. D.; Heikal, A. A.; Wiesner, U.; Webb, W. W. *Chem. Mater.* **2008**, *20*, 2677 – 2684.
6. Yin, Y.; Yuan, R.; Zhao, X. S. *J. Phys. Chem. Lett.* **2013**, *4*, 304 – 309.
7. Woehrstein, J. B.; Strauss, M. T.; Ong, L. L.; Wei, B.; Zhang, D. Y.; Jungmann R.; Yin P. *Sci. Adv.* **2017**, *3*, 1602128.
8. Willing, K. I.; Rizzoli, S. O.; Westphal, V.; Jahn, R.; Hell, S.W. *Nature*. **2006**, *440*, 935 – 939.
9. Small, A.; Stahlheber, S. *Nat. Methods*. **2014**, *11*, 267 – 279.

APPENDIX B

SUPPORTING INFORMATION FOR CHAPTER 3

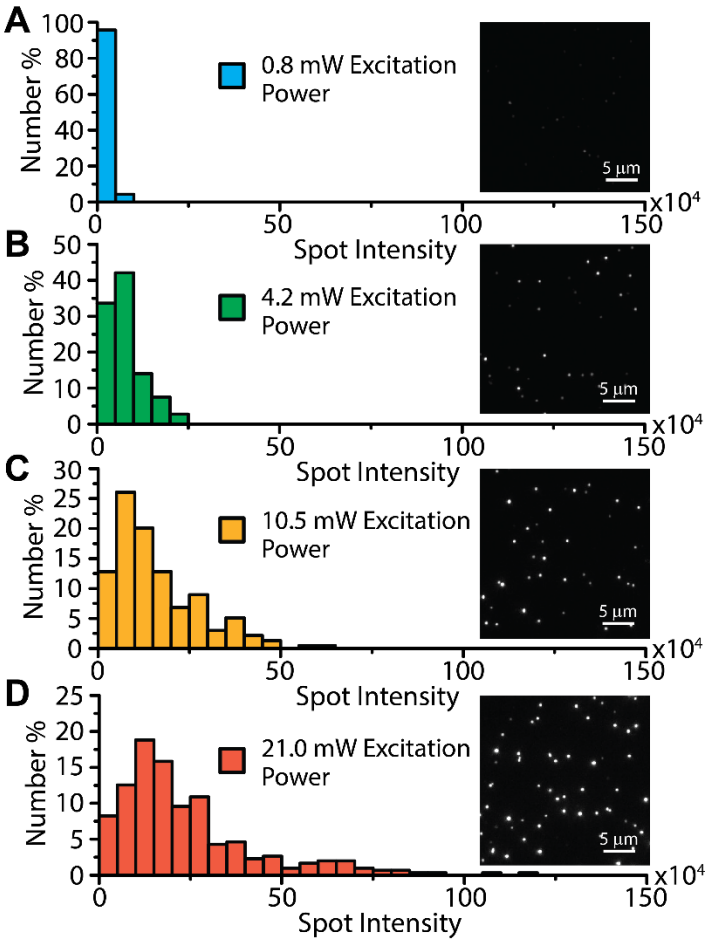

Figure B.1. Optimization of laser power in TIRF microscopy. (A) to (D) Single particle intensity distributions for SNPs prepared by homogenous growth using 1.3 µM Cy3/APTES. Images were acquired using (A) 0.8 mW, (B) 4.2 mW, (C) 10.5 mW, and (D) 21.0 mW laser power, measured at the objective. Representative fluorescence images are shown in the insets.

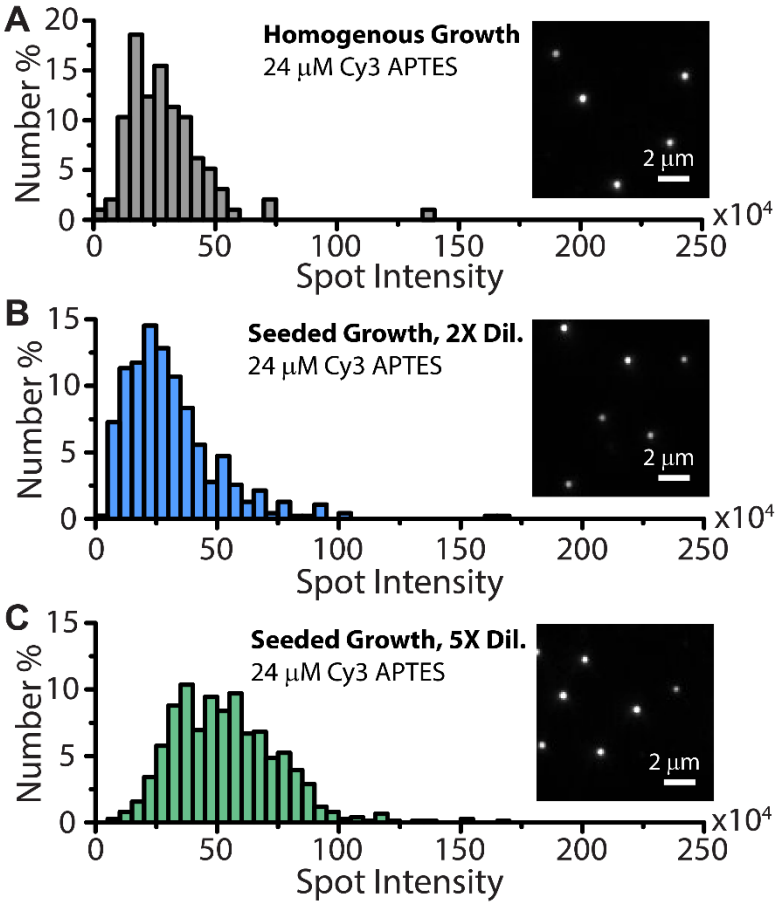

Figure B.2. Comparison of homogenous and seeded growth conditions in TIRF microscopy. (A) to (C) Single particle intensity distributions for SNPs prepared by (A) homogenous growth, (B) seeded growth of 2-fold diluted cores, and (C) seeded growth of 5-fold diluted cores. 24 μM Cy3/APTES was used in all syntheses. Representative fluorescence images are shown in the insets.

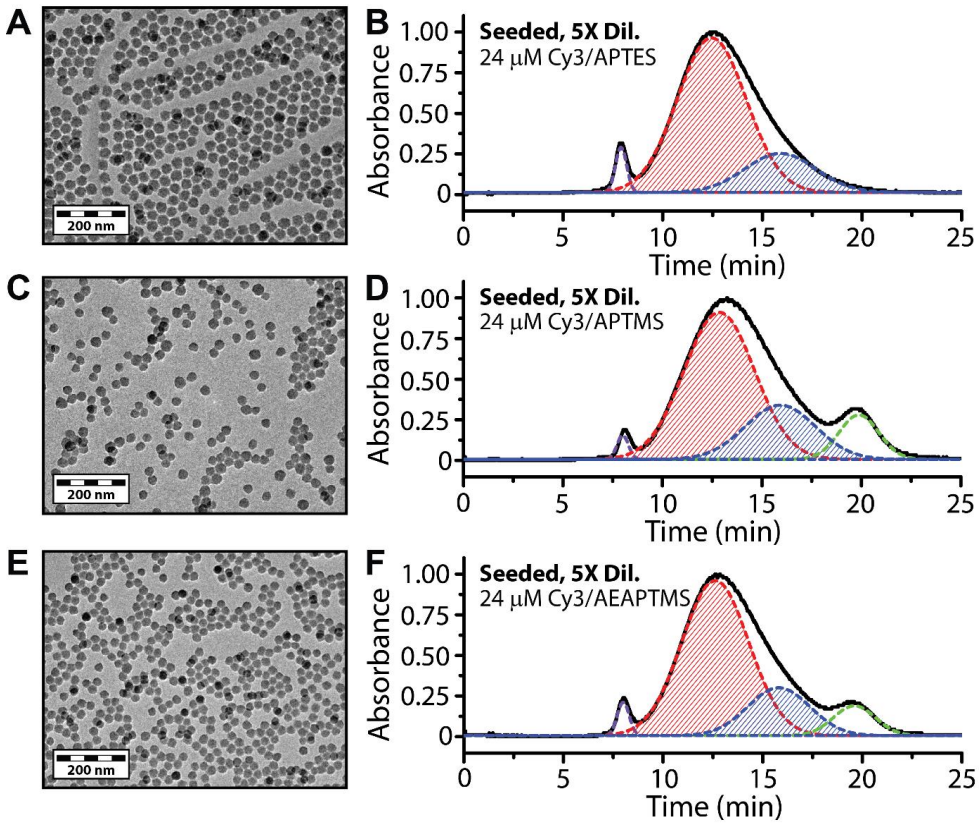

Figure B.3. Characterization of size dispersity in SNPs prepared using different dye conjugates. TEM images and GPC elugrams corresponding to SNPs prepared by seeded growth using (A, B) 24.0 μM Cy3/APTES, (C, D) 24.0 μM Cy3/APTMS, and (E, F) 24.0 μM Cy3/AEAPTMS. All dye conjugates in this series were prepared using a 10-fold excess of aminosilane. TEM images were taken prior to PEGylation and GPC purification. The dominant peak in each GPC elugram corresponds to the PEGylated SNP product. The asymmetric peak shape is attributed to the presence of smaller, secondary particles. This peak is therefore approximated as a superposition of two Gaussian distributions, corresponding to main (red) and secondary (blue) particle populations. The amount of secondary nucleation is estimated by comparing the peak areas calculated from the Gaussian fits. Calculated ratios of the secondary particle peak area (blue) to the main particle peak area (red) are (A) 0.26, (B) 0.37, and (D) 0.29. Gaussian fits of the aggregate (purple) and remaining free reactants (green) peaks complete the analysis.

APPENDIX C

SUPPORTING INFORMATION FOR CHAPTER 4

Cryo-TEM and micelle size measurements

For direct observation of micelle size and size distribution, five samples of native micelle solution (before silane addition) with varying [TMB] and stirring conditions were subjected to cryo-TEM characterization. The first four samples, containing 0mM, 4mM, 72mM and 116mM TMB, were prepared by adding TMB into CTAB/NH_4OH (22.78mM/150mM) aqueous solution under stirring at 600 rpm. The stirring was maintained at 600 rpm for two hours before an aliquot of the micelle solution was removed for cryo-TEM sample preparation. Immediately afterward, TMOS and APTMS were added to the native micelle solutions to make the corresponding MSNs shown in the bottom row of Fig.3a through d. The fifth sample, containing 72mM TMB, was prepared by adding TMB into CTAB/NH_4OH (22.78mM/150mM) aqueous solution under stirring at 600 rpm. The stirring was maintained at 600 rpm for about 30 seconds to ensure homogeneous dispersion of TMB into the solution. The stirring was then stopped and the solution was left static for two hours before cryo-TEM sample preparation. Then, the stirring was started again and maintained at 100 rpm during TMOS and APTMS addition. One minute after silane addition, the stirring was stopped and the reaction solution was kept static through the remainder of the synthesis. TEM results of this synthesis procedure are shown in Fig. 4.3e.

Samples for cryo-TEM analysis were prepared by plunge freezing. 4 μL of solution were pipetted onto a plasma-etched Quantifoil holey carbon TEM grid that was plasma cleaned for 10s with a mixture of argon and oxygen gases. The specimen was manually blotted for 6-8 seconds and plunged into a liquefied mixture of ethane

and propane[1]. Grids were transferred to the TEM and imaged below the recrystallization temperature of the specimen using a Gatan cryo-transfer holder. Cryo-TEM images were collected under low-dose conditions using a customized FEI Titan Themis 300 operating at 300 kV equipped with a cryo-box and FEI Ceta 16M camera. All images were collected at -2 μm defocus at a dose between 80-120 electrons/Å^2.

Micelle size distributions were determined from cryo-TEM images. Images were cropped to regions of micelles suspended in vitreous ice in a TEM grid hole. Using in-house python code, micelles were located via a Laplacian of Gaussian blob-detecting algorithm and their sizes measured by fitting the local image intensity at the location determined by the blob-finder to a two-dimensional Gaussian function. Reported diameters are $2\sqrt{2}\sqrt{\sigma_x^2 + \sigma_y^2}$, where σ_x and σ_y are the standard deviation of the 2D Gaussian in x and y directions determined by the longest and shortest axes of the micelle. For each image, the intensity threshold of the blob-detecting algorithm was set by hand to ensure correct identification of micelles without inclusion of noise. Size distributions for each condition were calculated from 5-7 images collected at different locations across the TEM grid.

To describe the shape of the micelle size distributions, the histograms were fit to a skew-normal distribution using nonlinear least squares fitting in python:

$$A\left(1 + \mathrm{erf}\left(\frac{\alpha(x-\mu)}{\sigma\sqrt{2}}\right)\exp\left(-\frac{(x-\mu)^2}{2\sigma^2}\right)\right), \quad (1)$$

where erf is the error function, A, μ and σ are amplitude, average size and scale parameter, respectively. The parameter α describes the departure from the normal distribution and improves fitting for distributions with a longer tail. The skew-normal distribution was chosen because it describes well the tail of the size distribution contributed by larger micelles[2].

Tiling Analysis

The edges of the square-triangle tiling correspond to the six dodecagonal directions in physical (or parallel) space. Each vertex in parallel space can be expressed as

$$\mathbf{r}^{\parallel} = n_1\mathbf{e}_1^{\parallel} + n_2\mathbf{e}_2^{\parallel} + n_3\mathbf{e}_3^{\parallel} + n_4\mathbf{e}_4^{\parallel}, \quad (2)$$

where n_i is a unique set of integer coordinates and $\mathbf{e}_i^{\parallel} = \{\cos(\alpha(i - 1)), \sin(\alpha(i - 1))\}$ with $\alpha = \pi/6$ and i = 1-4. The corresponding vector $\mathbf{r}^{\perp}$ in perpendicular space is

$$\mathbf{r}^{\perp} = n_1\mathbf{e}_1^{\perp} + n_2\mathbf{e}_2^{\perp} + n_3\mathbf{e}_3^{\perp} + n_4\mathbf{e}_4^{\perp}, \quad (3)$$

where n_i is again a unique set of integer coordinates and the dodecagonal directions in perpendicular space are $\mathbf{e}_i^{\perp} = \{\cos(7\alpha(i - 1)), \sin(7\alpha(i - 1))\}$ with $\alpha = \pi/6$ and i = 1-4. As shown in Figure 2d, the 2D parallel and perpendicular spaces are identified by means of consistency of $\mathbf{e}_1^{||,\perp}$ and $\mathbf{e}_3^{||,\perp}$.

Following transformation from parallel to perpendicular space, a crystalline pattern, e.g. with pure square or triangle packing, remains unchanged. In contrast, a quasicrystalline pattern shrinks upon translation to perpendicular space. The degree of shrinkage reflects the disorder in the triangle-square packing and can be used as a measure of quasicrystallinity. For this reason, the quasicrystallinity of a pattern can be obtained by comparing the radii of gyration of the patterns in parallel and perpendicular spaces. The relationship between the radii of gyration in the two spaces can be described by the linear equation $R_g\perp = AR_g// + B$, where the slope provides the magnitude of the phason strain, a quantitative measure of quasicrystallinity. The phason strains of an ideal quasicrystal and crystal are 0 and 1, respectively.

Tilings of the synthesized MSNs were obtained from TEM images using a self-written MATLAB program, where 10% tolerance of edge orientation and edge length are allowed and undeveloped pores were not counted. These tilings were further analyzed by using a second self-written program to calculate $R_g//$ and $R_g\perp$ and to

quantify the presence of the four fundamental geometrical conformers present in the structure, i.e. 4^4, 3^34^2, 3^2434 and 3^6 (see details in main text). Considering that differently sized MSNs synthesized at the same [TMB] but at varying pH are expected to have similar micelle size and size distribution, a linear fit ($R_g\perp = AR_g// + B$) was applied to MSNs synthesized at the same [TMB]. For MSNs synthesized at the highest [TMB] with the highest quasicrystallinity, the plot of $R_g\perp$ vs. $R_g//$ was described well by this linear relationship. This suggests that individual MSNs have the same type of crystalline pattern, and thus the fitted slope represents the phason strain of the structure obtained from this [TMB]. In contrast, as [TMB] decreased, large particles synthesized at intermediate [TMB] exhibited substantial fluctuations in the plot of $R_g\perp$ vs. $R_g//$, suggesting that the MSN structure obtained from those synthesis conditions was heterogeneous. Therefore, in this case the slope of the linear fit does not reflect the phason strain of these individual particles. However, the fact that the slope of these fits increased with increasing [TMB] (or decreased with decreasing [TMB]) suggests that the average quasicrystallinity of all the MSNs from a single synthesis is highly dependent on [TMB].

Growth Simulations

Growth of quasicrystalline mesoporous silica materials has previously been modeled as a random aggregation of triangle and square tiles[3]. The relationship between these fundamental triangle/square units and CTAB micelle packings is illustrated schematically in Figure 1m. While these simulations do not directly address the details of the micelle packing process, they can play an important role in developing an understanding of the structural arrangement of triangle/square tiles observed experimentally in quasicrystalline mesoporous silica. We have therefore modeled our experimental system using a similar tiling process[3].

We employed a random square-triangle tiling process wherein cluster growth, seeded by an individual equilateral triangle or square tile, proceeds by sequential and irreversible edge-to-edge addition of triangle and square tiles with edge length *a*. The seed tile and all subsequent tiles were randomly chosen from a weighted distribution defined by an input triangle/square ratio that reflects the micelle size distribution at varying [TMB]. New tiles were placed at random, according to a probability-weighted list of candidate growth sites defined as edges that lie on the boundary of the growing cluster. Candidate sites were assigned probabilities according to physically inspired interaction potential energies. The tiling process proceeded until the final particle size, determined at the start of each simulation from a weighted normal distribution about an average particle size, was reached. Importantly, we did not make any effort to suppress the stochastic noise that accompanies this process. Comparison with experimental data showed that these results may reflect local fluctuations of the micelle sizes in solution.

In defining interaction potentials for candidate growth sites, we included two separate contributions, one that reflects the incoming shape and the geometry of the site and one that is directly related to the distance, *d*, of the site from the center of mass of the growing cluster. Interaction potentials were optimized so that an input triangle/square ratio of 2.3 (chosen to reflect the triangle/square ratio in an ideal dodecagonal quasicrystal) produced clusters with quasicrystalline features and were then held constant for the remainder of these simulations. The form of the attachment probability, *P*, associated with each candidate site was also considered a fitting parameter and was ultimately determined to be:

$$P = P_s \times (d/d_0)^{-10}, \quad (4)$$

where P_S is the attachment probability associated with the surface site geometry, and *d*, the distance from center parameter is normalized by d_0, the shortest radial distance

from the particle edge to its center of mass. This surface minimizing condition produced tilings that mirror the spherical morphology of particles observed in experiments. Contributions to P_S are specified as follows:

(1) The edge-edge contact between a square and a triangle P_{ST}, two triangles P_{TT}, two squares P_{SS}.

(2) The interaction between an incoming square tile and an incomplete 90º corner, P_R.

(3) The interaction between an incoming triangle tile and incomplete 60º or 120º corners, P_T .

Using a triangle/square ratio of 2.3, parameter values were P_{ST} = 0.75, P_{TT} = 0.001, P_{SS} = 0.001, P_R = 0.75, and P_T = 0.75. We found that it was necessary to include P_{TT} and P_{SS} as constant repulsive parameters to prevent the formation of large hexagonal or cubic domains, which were not observed in our experimental particles. These repulsive parameters may reflect interfacial interactions between micelles[3]. Additionally, P_R and P_T were included as attractive parameters to discourage defect formation. For sites that could be assigned to multiple categories, the highest P_S was used. However, if tile attachment generates a defect that cannot accommodate either shape, P_S = 0.0000075. Thus each growth site was given a single interaction potential, specifically defined as the probability that particular site will be filled. For each tile addition, a revised list of interaction potentials was generated to reflect changes to the list of candidate growth sites and a specific growth site was randomly chosen from this probability-weighted list. Optimized values of P_S were kept constant for the remainder of the simulations where the triangle/square number ratio was varied to reflect the range of [TMB] used in experiments.

In order to address the possibility that only growth sites with very low attachment probabilities exist, an additional threshold parameter was included. This attachment threshold, T, is given by

$$T = 0.000075 \times r, \quad (5)$$

where r is the maximum radial distance from the particle edge to its center of mass. If the growth site chosen from the distribution of attachment probabilities is below T, then the tile is not placed. Instead, a new tile is chosen from the shape distribution and the choice is repeated. If after 100 attempts, no site with $P > T$ is chosen, then the growth site is temporarily removed from the list of candidate sites and a new tile is again chosen. This process is repeated until a tile can be placed and growth can proceed. Since the attachment probability is shape specific, the threshold mechanism may act as a barrier to attachment of either type of tile, allowing mismatches between the input triangle to square ratio and resulting particle composition.

For each triangle/square ratio, four batches of particles with varying average diameter were generated and combined for analysis. Final particle size was determined at the start of each simulation by random choice from a probability weighted distribution about an average size. The simulation was terminated when the particle reached the predetermined size. In defining the distribution of particle sizes, we utilized a set of four normal distributions with mean (μ) and variance (σ) parameters as follows.

Set A: (μ, σ) = (1.5, 0.5)

Set B: (μ, σ) = (3.5, 1.5)

Set C: (μ, σ) = (6.0, 2.0)

Set D: (μ, σ) = (7.5, 2.5)

These distributions were chosen to reflect the sizes of the particles observed in experiments.

Fitting of the relationship between $R_g\perp$ and the total number of squares before the first triangle is attached.

The black dots in Figure 5b and c, for which no triangle ever entered the simulations, represent the relationship between the total area and the radius of gyration of a 2D square packing. However, it is interesting to note that all the other data points in Figure 5c, which came from the simulations whose final structure does contain triangles, lie on the same curve. This indicates that the growth of particles in perpendicular space follows the same trend whether or not a triangle is involved in the particle growth; and this is independent of the particle's final quasicrystallinity. In order to quantitatively resolve this general relationship, all the data in Figure 5c were fitted using the equation $N = N(R_g\perp)$ of 2D tiling of squares. To derive the fitting equation, an approximation was first made that the shape of the overall tiling is a perfect square. This is consistent with experiments in which cubic MSNs always have square facets (Fig. 4.1d).

According to the definition of the radius of gyration, R_g, the radius of gyration of a 2D square packing follows the equation:

$$R_g{}^2 = \frac{1}{(\sqrt{N}+1)^2}\sum_{n=0}^{(\sqrt{N}+1)^2} r_n{}^2, \quad (6)$$

where N is the total number of squares and r_n is the distance of point n to the center of mass of the packing:

$$r_n = a \cdot \sqrt{(x_n{}^2 + y_n{}^2)}, \quad (7)$$

where x_n and y_n are the normalized coordinates of point n in the coordinate system whose origin is the center of mass of the overall square tiling. $a = 1$ is the edge length of a single square tile.

R_g can then be expressed as:

$$\left(\frac{R_g}{a}\right)^2 = \frac{1}{6}\left(\left(\sqrt{N}+1\right)^2 - 1\right), \quad (8)$$

Solving for N yields the relationship between R_g and N:

$$N = 6\left(\frac{R_g}{a}\right)^2 - 2\sqrt{6\left(\frac{R_g}{a}\right)^2 + 1} + 2, \quad (9)$$

N for large packings, where $6\left(\frac{R_g}{a}\right)^2 \gg 1$, can be approximated by:

$$N \approx 6\left(\frac{R_g}{a}\right)^2 - 2\sqrt{6}\left(\frac{R_g}{a}\right) + 2 \approx 6\left(\frac{R_g}{a}\right)^2 - 4.9\left(\frac{R_g}{a}\right) + 2, \quad (10)$$

Since $a = 1$,

$$N \approx 6{R_g}^2 - 4.9R_g + 2, \quad (11)$$

We therefore fitted the data in Figure 5c using the equation:

$$N = A{R_g}\perp^2 + BR_g\perp + C, \quad (12)$$

where the fitted values A, B and C were equal to 6.3, -6.3 and 2.6, respectively. These values agree well with the theoretical expectations as described above.

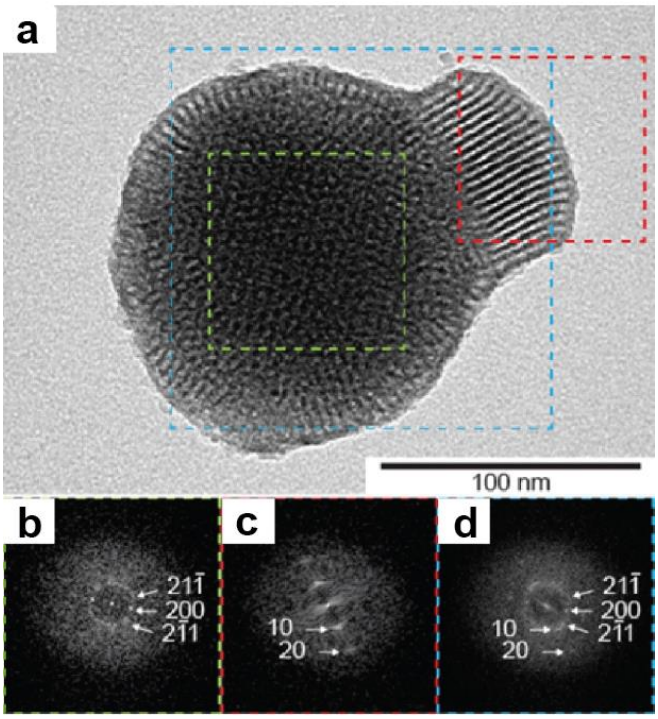

Figure C.1. Fast Fourier transform analysis of a tetraethyl orthosilicate/N-(2-aminoethyl)-3-aminopropyltrimethoxysilane derived multicompartment particle. **a,** Transmission electron microscopy image of a multicompartment mesoporous silica nanoparticle with one branch, synthesized using 29 mM mesitylene and 13.8 mM ammonium hydroxide. The reaction stirring rate was 650 rpm. The scale bar is 100 nm. **b,** Fourier diffractogram (FD) of the cubic core region in (**a)** (green box), showing spots from the cubic *Pm*$\bar{3}$*n* lattice along the [110] zone axis. **c**, FD of the hexagonal branch region in (**a**) (red box), showing spots from the hexagonal *p*6*mm* lattice. **d,** FD of the region containing both compartments in (**a**) (blue box), showing that the cubic 211 and hexagonal 10 spots reside closely with a lattice mismatch of 8.5% (larger for cubic lattice). This lattice mismatch is compensated by low-angle defects at the (111) plane.

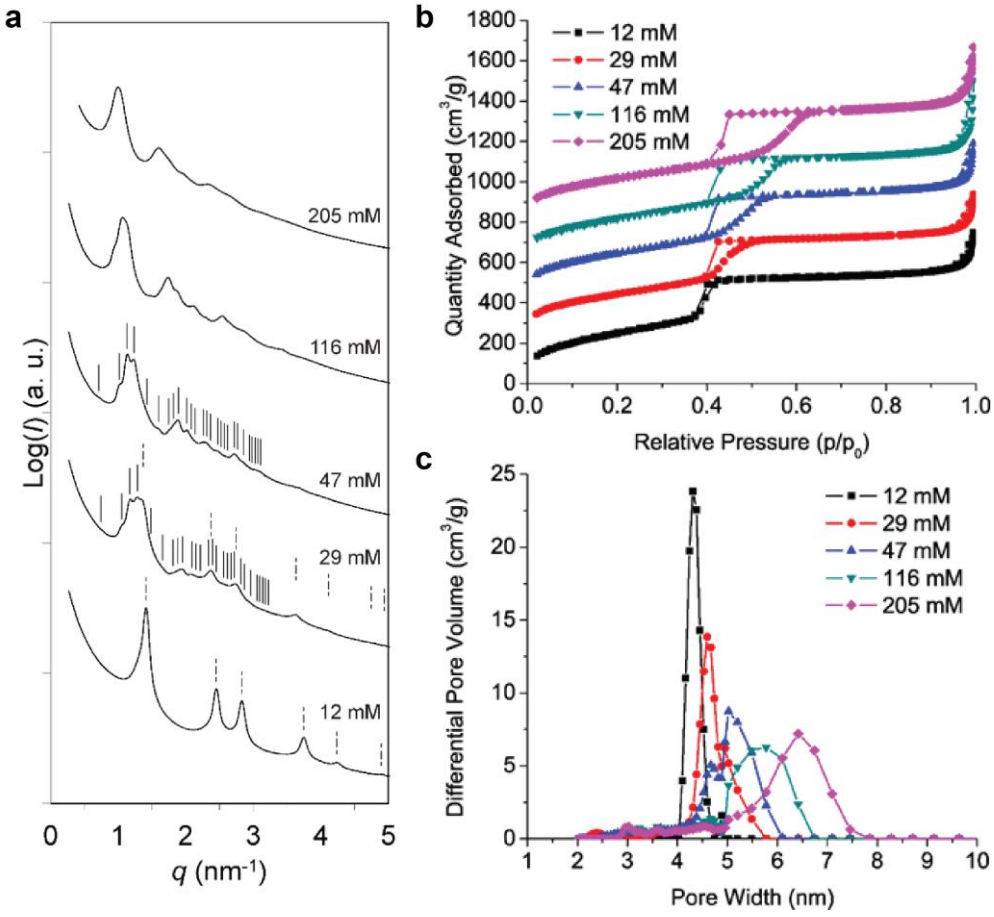

Figure C.2. Structure evolution of tetraethyl orthosilicate/N-(2-aminoethyl)-3-aminopropyltrimethoxysilane derived mesoporous silica nanoparticles as a function of mesitylene concentration as revealed by small angle x-ray scattering and nitrogen sorption. **a**, Small angle x-ray scattering patterns of mesoporous silica nanoparticles prepared at 12 mM, 29 mM, 47 mM, 116 mM, and 205 mM mesitylene (TMB). Particles were synthesized using constant ammonium hydroxide (13.8 mM) and stirring rate (650 rpm). Expected peak positions from cubic $Pm\bar{3}n$ and hexagonal *p*6*mm* lattices are marked using solid and dashed lines, respectively. **b**, **c**, Nitrogen sorption isotherms (**b**) and corresponding density functional theory (DFT) derived pore size distributions (**c**) of mesoporous silica nanoparticles prepared at varying TMB concentrations. In (**b**), starting from the second curve, each isotherm is offset along the *y*-axis by 200 cm^3/g compared to the previous one. All samples exhibited type IV isotherms with increasing size of hysteresis loops, attributed to the expansion of mesopores, which was further elucidated by the pore size distributions calculated using a DFT model.

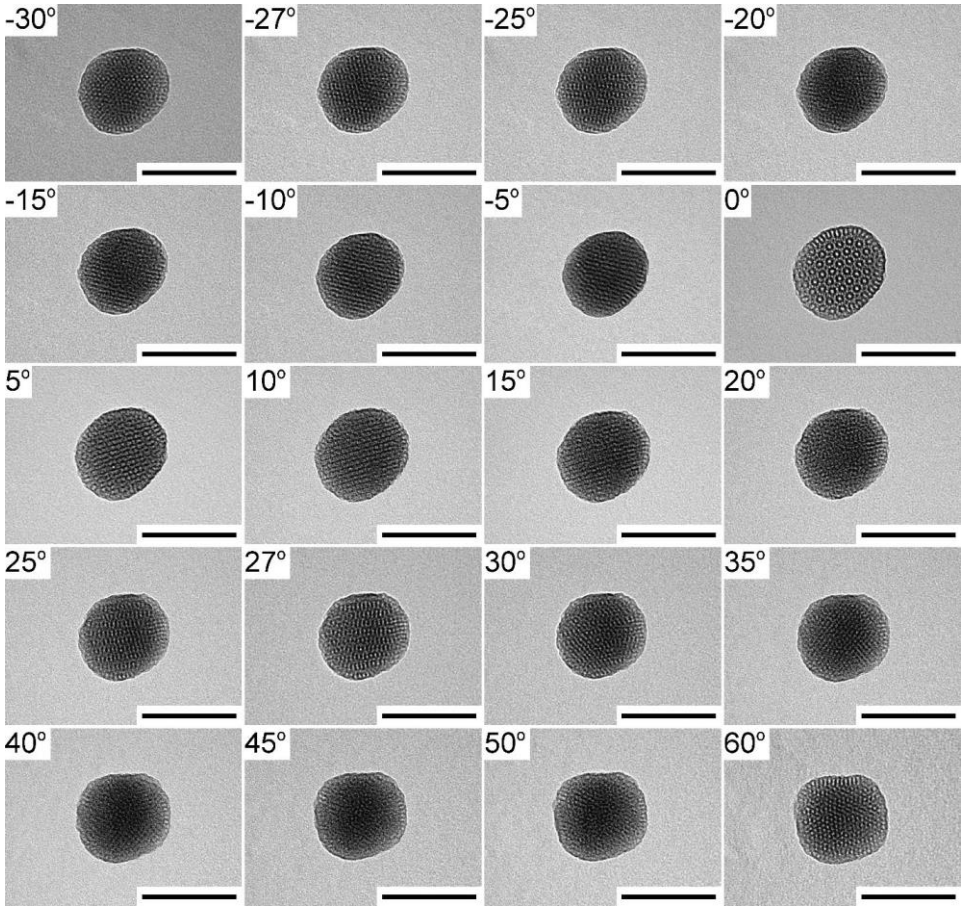

Figure C.3. Single-tilt transmission electron microscopy study of a tetraethyl orthosilicate/N-(2-aminoethyl)-3-aminopropyltrimethoxysilane derived mesoporous silica nanoparticle with dodecagonal tiling. Quasicrystalline tetraethyl orthosilicate/N-(2-aminoethyl)-3-aminopropyltrimethoxysilane particles were synthesized using 116 mM mesitylene and 13.8 mM ammonium hydroxide. The reaction stirring rate was 650 rpm. From these images it is difficult to extract the three-dimensional particle structure. All scale bars are 100 nm.

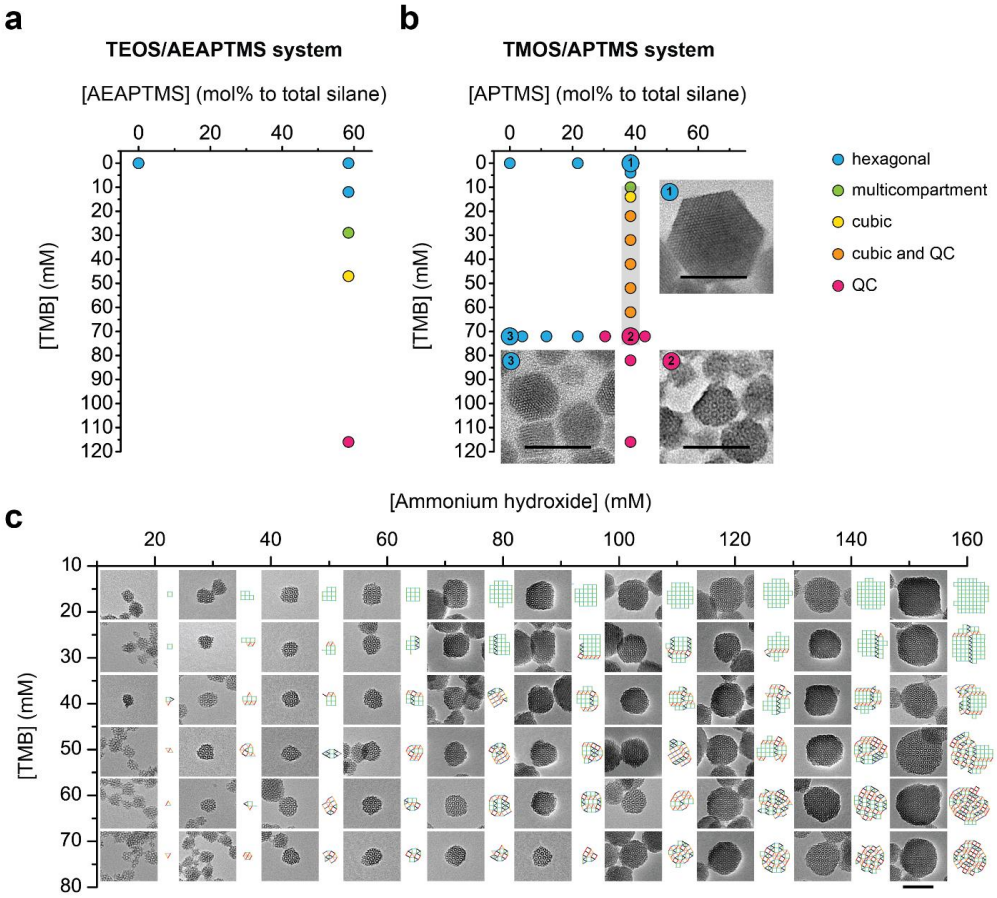

Figure C.4. Synthesis maps of mesoporous silica nanoparticles synthesized using two different silane systems. **a**, **b,** Structures of tetraethyl orthosilicate/N-(2-aminoethyl)-3-aminopropyltrimethoxysilane (TEOS/AEAPTMS) (**a**) and tetramethyl orthosilicate/(3-aminopropyl)trimethoxysilane **(**TMOS/APTMS) (**b**) derived mesoporous silica nanoparticles synthesized under varying mesitylene (TMB) and aminosilane concentrations. TEOS/AEAPTMS and TMOS/APTMS derived MSNs were synthesized using 13.8 mM and 120 mM ammonium hydroxide, respectively. The insets in (**b**) are transmission electron microscopy (TEM) images of representative TMOS/APTMS derived particles. The numbered markers in the top left corner of each TEM image can be correlated to specific positions on the synthesis map. **c**, Extended data set relative to what is shown in Fig. 2e of the main text, including TEM images and square-triangle tilings of mesoporous silica nanoparticles synthesized using the TMOS/APTMS system. The concentration of APTMS used in synthesizing this series of particles was 14 mM. Scale bars in all images are 100 nm.

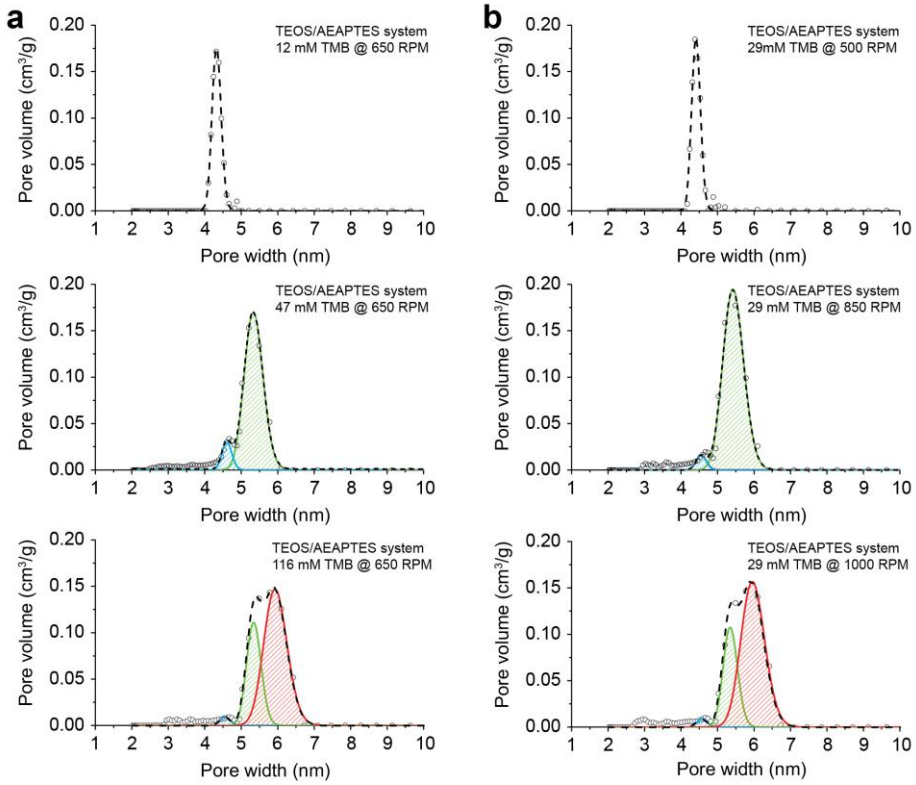

Figure C.5. Pore size analysis of tetraethyl orthosilicate/N-(2-aminoethyl)-3-aminopropyltrimethoxysilane derived mesoporous silica nanoparticles synthesized under varying conditions. **a,** Pore size distributions of mesoporous silica nanoparticles synthesized using the tetraethyl orthosilicate/N-(2-aminoethyl)-3-aminopropyltrimethoxysilane (TEOS/AEAPTES) system and varying mesitylene (TMB) concentrations. **b,** Pore size distributions of mesoporous silica nanoparticles synthesized using TEOS/AEAPTES system and varying stirring rates. The ammonium hydroxide concentration in all syntheses was 13.8 mM. The pore size distributions obtained from fits of the corresponding nitrogen adsorption/desorption experiments shown in Supplementary Figures 2 and 6 were fit with linear combinations of one, two, or three lognormal functions. In bimodal and trimodal fits small, medium, and large micelle distributions are colored blue, green, and red, respectively.

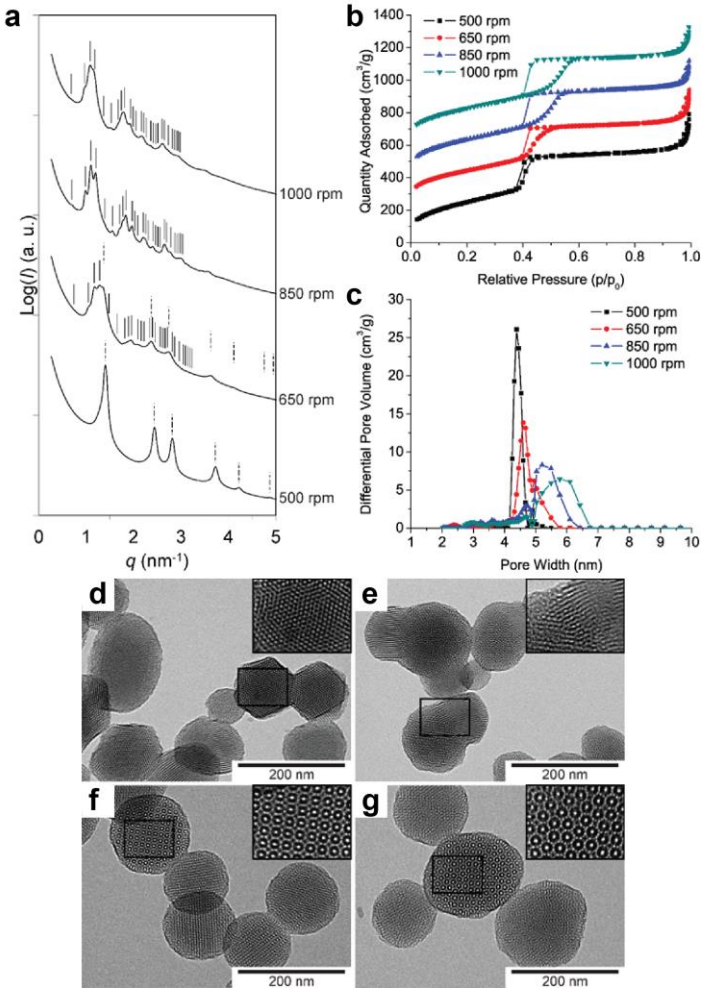

Figure C.6. Structure evolution of tetraethyl orthosilicate/N-(2-aminoethyl)-3-aminopropyltrimethoxysilane derived mesoporous silica nanoparticles as a function of stirring rate. (**a**) Small angle x-ray scattering (SAXS) patterns, (**b**) nitrogen sorption isotherms, and (**c**) corresponding density functional theory derived (DFT) derived pore size distributions of mesoporous silica nanoparticles prepared from tetraethyl orthosilicate (TEOS), N-(2-aminoethyl)-3-aminopropyltrimethoxysilane (AEAPTES), and 29 mM mesitylene (TMB) at varying stirring rates. The ammonium hydroxide concentration in all syntheses was 13.8 mM. In the SAXS patterns, expected peak positions for cubic $Pm\bar{3}n$ and hexagonal $p6mm$ lattices are indexed using solid and dashed lines, respectively. In (**b**), starting from the second curve, each isotherm is offset along the y-axis by 200 cm^3/g compared to the previous one. **d-g,** Transmission electron microscopy images of TEOS/AEAPTMS derived mesoporous silica nanoparticles prepared from 29 mM TMB at stirring rates of (**d**) 500 rpm, (**e**) 650 rpm, (**f**) 850 rpm, and (**g**) 1000 rpm. Scale bars are 200 nm. Insets are magnified images on selected areas (rectangles).

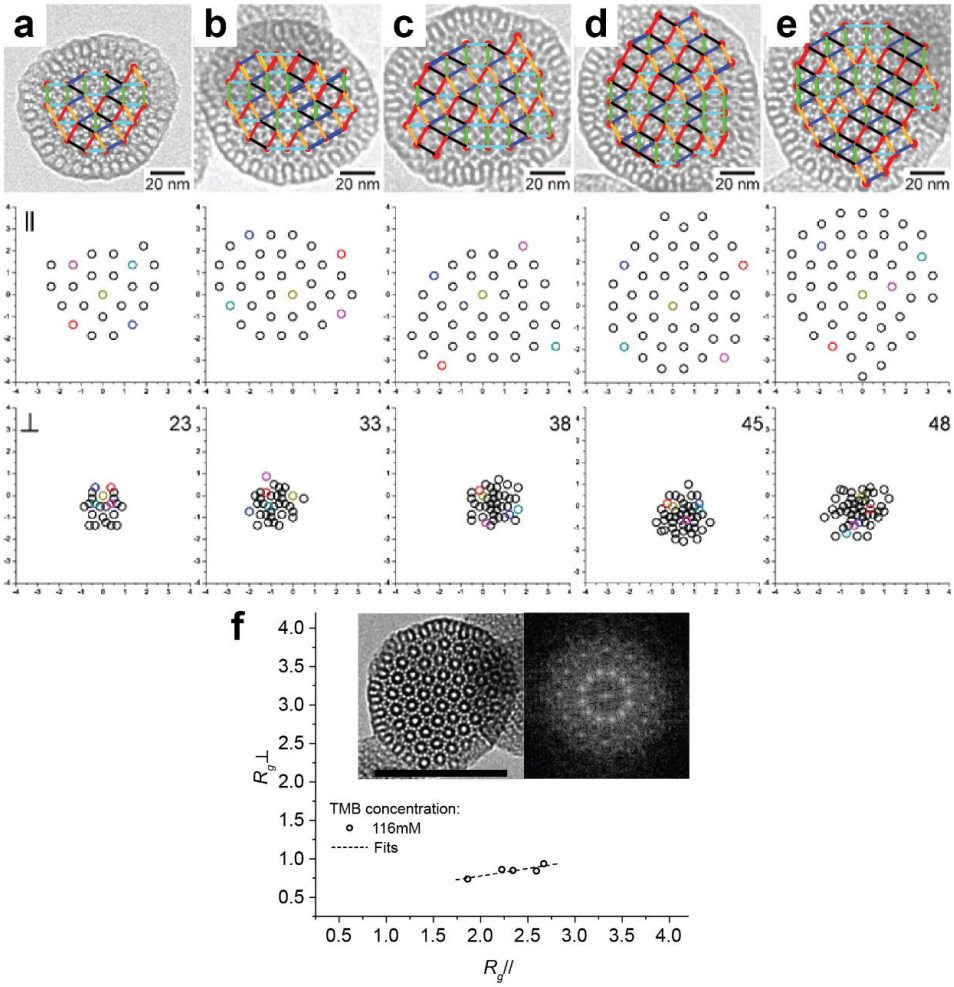

Figure C.7. Tiling analysis for mesoporous silica nanoparticles synthesized using the tetraethyl orthosilicate/N-(2-aminoethyl)-3-aminopropyltrimethoxysilane silane system at 116mM mesitylene. **a-e,** Square-triangle tilings superposed on high-magnification transmission electron microscopy (TEM) images of five dodecagonal mesoporous silica nanoparticles with (**a**) 23, (**b**) 33, (**c**) 38, (**d**) 45, and (**e**) 48 vertices. The randomly colored points in the associated parallel and perpendicular space plots show how individual points move during the transformation from parallel to perpendicular space. **f,** Corresponding phason strain analysis of mesoporous silica nanoparticles. Plot of R_g in perpendicular vs. parallel space, calculated for tetraethyl orthosilicate/N-(2-aminoethyl)-3-aminopropyltrimethoxysilane derived mesoporous silica nanoparticles synthesized at 116 mM mesitylene (TMB) and 13.8 mM ammonium hydroxide. The reaction stirring rate was 650 rpm. The phason strain determined from this analysis is 0.19. The insets show a TEM image of a quasicrystalline MSN (left) and the corresponding Fourier diffractogram (right), scale bar 100nm.

Varying [TMB] @ Constant Stirring Rate					
	[TMB]		**Small Pores**	**Medium**	**Large Pores**
650 RPM	**12 mM**	Total Vol. (cm^3/g)	0.055		
		Avg. Pore Width (nm)	4.3		
		FWHM (nm)	0.3		
	47 mM	Total Vol. (cm^3/g)	0.010	0.109	
		Avg. Pore Width (nm)	4.6	5.3	
		FWHM (nm)	0.3	0.6	
	116 mM	Total Vol. (cm^3/g)	0.003	0.055	0.117
		Avg. Pore Width (nm)	4.6	5.3	5.9
		FWHM (nm)	0.3	0.4	0.5
	205 mM	Total Vol. (cm^3/g)	0.002	0.028	0.186
		Avg. Pore Width (nm)	4.4	5.5	6.5
		FWHM (nm)	0.3	0.7	1.1
Constant [TMB] @ Varying Stirring Rates					
	Stirring		**Small Pores**	**Medium**	**Large Pores**
29 mM TMB	**500 rpm**	Total Vol. (cm^3/g)	0.056		
		Avg. Pore Width (nm)	4.4		
		FWHM (nm)	0.3		
	850 rpm	Total Vol. (cm^3/g)	0.005	0.139	
		Avg. Pore Width (nm)	4.6	5.4	
		FWHM (nm)	0.3	0.7	
	1000 rpm	Total Vol. (cm^3/g)	0.003	0.053	0.127
		Avg. Pore Width (nm)	4.6	5.4	6.0
		FWHM (nm)	0.3	0.5	0.8

Table C.1. Pore size analysis derived from nitrogen sorption measurements on mesoporous silica nanoparticles synthesized using tetraethyl orthosilicate and N-(2-aminoethyl)-3-aminopropyltrimethoxysilane. Total pore volumes, average pore diameters, and full width at half maximum (FWHM) values are determined from log-normal fits of plots of incremental volume vs. pore diameter (fits shown in Fig. C.5).

REFERENCES

1. Tivol, W. F., Briegel, A. & Jensen, G.J. An Improved Cryogen for Plunge Freezing. *Microsc. Microanal.* **14,** 375-379 (2008).
2. Azzalini, A. A class of distributions which includes the normal ones. *Scand. J. Stat.* **12**, 171-178 (1985).
3. Xiao, C., Fujita, N., Miyasaki, K., Sakamoto, Y. & Terasaki, O. Dodecagonal tiling in mesoporous silica. *Nature* **487**, 349-353 (2012).

APPENDIX D

SUPPORTING INFORMATION FOR CHAPTER 5

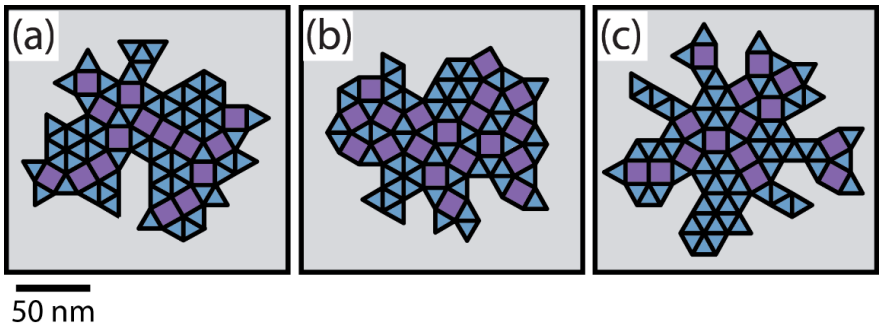

Figure D.1. (a-c) Tilings from simulations performed using a modified version of Tiling Rule 3 that allows replacement site selection only. A scale bar is defined using the tile edge length measured from TEM images of MSNs.

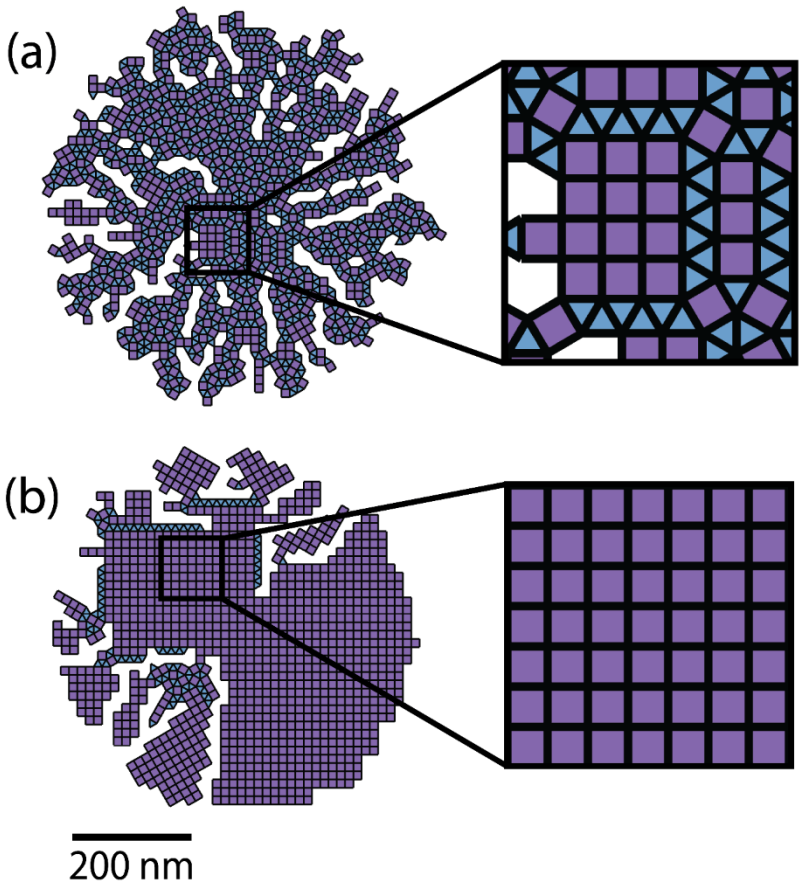

Figure D.2. Representative tilings using S = 0.1 (a) and 0.01 (b) and radius = 25 *d*. A scale bar is defined using the tile edge length measured from TEM images of MSNs. Particle cores are marked using black boxes and are shown magnified in the insets.